Wall Shear Stress in coronary arteries

J.T.C. Schrauwen

Wandschuifspanning in kransslagaders

Wall Shear Stress in Coronary Arteries

Proefschrift

ter verkrijging van de graad van doctor aan de
Erasmus Universiteit Rotterdam
op gezag van de
rector magnificus

prof.dr. H.A.P. Pols

en volgens besluit van het College voor Promoties.

De openbare verdediging zal plaatsvinden op
vrijdag 19 februari 2016 om 13.30 uur door

Jelle Tymen Christiaan Schrauwen
geboren te Roosendaal

Erasmus University Rotterdam

PROMOTIECOMMISSIE

Promotor	Prof.dr.ir A.F.W. van der Steen
Co-promotor	Dr.ir. F.J.H. Gijsen
Overige leden	Prof.dr. W.J. Niessen
	Prof.dr.ir. F.N. van de Vosse
	Dr. E.S. Regar

Voor mijn ouders

TABLE OF CONTENTS

Chapter 1

Introduction

Coronary Artery Disease

Coronary arteries supply the heart with blood. Coronary artery disease can cause narrowing of the coronary arteries and inhibit blood flow. A narrowed part of a coronary artery is called a stenosis. Coronary artery disease can lead to various symptoms. A partial but stable stenosis that limits the blood flow can cause a patient to have predominantly chest pains, which is especially provoked during physical activity or emotional stress. This condition is called stable angina. In more severe cases coronary artery disease leads to an acute coronary syndrome, more commonly known as a heart attack. In this case blood cloths fully block the coronary artery preventing blood to perfuse the heart muscle. If the blockage is not resolved this will result in an infarction of the myocardial area that is being deprived of blood. Well known systemic risk factors leading to coronary artery disease include high cholesterol, high blood pressure, diabetes and smoking.

Cardiovascular disease in general is the leading cause of death in Europe. Coronary artery disease alone is responsible for as much as 1.8 million deaths in Europe annually, or in other words 20% of all deaths[1]. In the Netherlands ischemic heart disease takes about 10.000 lives yearly[2]. It is therefore of the utmost importance for society to improve current treatment strategy and develop more effective pre-emptive screening methods.

Atherosclerosis in coronary arteries

The underlying cause of coronary artery disease is atherosclerosis. Atherosclerosis is a chronic inflammatory disease of the arterial wall with various manifestations[3,4]. The first stage of atherosclerosis is characterized by the build-up of low-density lipoproteins, which is accompanied by inflammatory cell infiltration, smooth muscle cell proliferation and extracellular matrix accumulation[5]. The resulting material build-up in the wall is called a plaque. Within these plaques calcified regions can form or areas with cholesterol crystals[6]. With regards to acute coronary syndrome there is special interest in the plaque type where lipid pools or necrotic cores are formed close to the surface of the wall. Virmani et al. defined this by incorporating one specific morphological characteristic, namely the fibrous cap that separates the necrotic core from the lumen[7]. This type was dubbed a thin cap fibroatheroma (TCFA)[8]. The reason to emphasize the cap is that the rupture of this cap initiates thrombotic events potentially followed by sudden death[9–11].

Over the years different treatment strategies evolved for diagnosing coronary stenoses. The first approach is identifying flow limiting stenoses based on imaging data. To do so, the ratio between the diameter of the stenosis and the diameter of the healthy wall is calculated. This ratio is known as the stenosis degree. Plaques that have a stenosis degree of 50% or more can, in general, become flow limiting and patients can start presenting symptoms of angina. Although more advance strategies evolved over the years, it is still the predominant approach during routine procedures[12]. The choice for

this strategy is driven by the relative ease of obtaining and interpreting imaging data of the coronary lumen, but also by its considerable success rate. The diagnosis relies entirely on the assessment of the geometry with angiography and cannot differentiate between stable fibrotic plaques or unstable high-risk TCFA.

A second approach followed from the ideas presented in two landmarks studies by Gould et al.. In these studies the physiological reaction of the myocardium and the resulting coronary flow were investigate in the presence of a stenosis[13,14]. Resting flow conditions appeared to be unaffected by stenosis degree up to 85% of the arterial diameter. At hyperemic conditions -when maximal flow is achieved- stenosis degrees markedly reduced the observed flows that were not affected at resting conditions. Plaques having a diameter stenosis as small as 30% can become flow limiting. Lesion severity
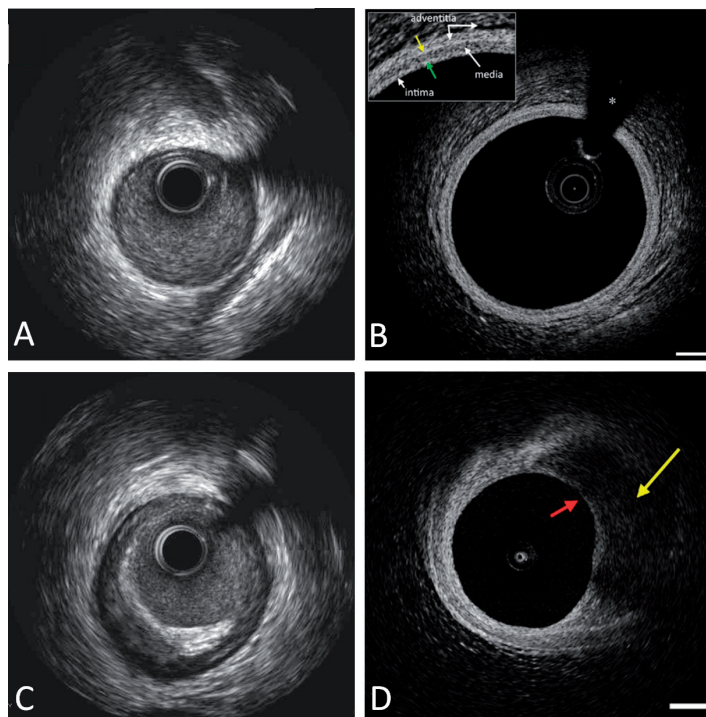
Fig 1: Overview of intravascular imaging techniques used to detect atherosclerosis in coronary arteries. **A:** Cross section of a healthy coronary wall imaged with IVUS. The lumen can clearly be delineated and the wall shows no signs of atherosclerosis. **B:** Cross section of healthy coronary wall imaged with OCT. The lumen can again nicely be delineated and no signs of atherosclerosis are distinguishable. The three layers from the wall can nicely be delineated. **C:** Cross section of diseased human coronary wall imaged with IVUS. The bottom left section of the wall shows characteristics of an advanced atherosclerotic lesion. **D:** Cross section of diseased human coronary wall imaged with OCT showing the characteristics of a TCFA: the fibrous cap (left red arrow) with a signal-poor region behind it indicative for a necrotic core (right yellow arrow). (A. and C. Courtesy of J.C.H. Schuurbiers; B. and D. Adjusted from Tearney et al.[21])

therefore provides limited information to assess the hemodynamic consequences a stenosis has. Coronary flow reserve relates to the capacity of the myocardium to increase flow in the presence of a stenosis in order to meet oxygen demand. Taking the concept of coronary flow reserve, Pijls et al. adjusted it in such a way that pressure measurements could be used to assess the hemodynamic effect of coronary stenosis[15,16]. This resulted in the fractional flow reserve (FFR) that is defined as the ratio of the pressure distal and the pressure proximal of a stenosis under hyperemic conditions. This catapulted the use of inspecting hemodynamic influence of stenoses in a clinical setting, since methods to measure pressure were widely available. In large scale trails FFR proved to be a better marker to guide intervention than visual inspection of lesion severity[17,18]. It was eventually establish that an FFR value of 0.80 or lower was indicative for ischemia due to the stenosis. The strength of this diagnosis is that it uses functional data of the coronary system.

A third approach to diagnose atherosclerosis is to incorporate intravascular imaging that visualizes the plaque within a vessel wall. The two most frequently used catheter-based techniques are intra-vascular ultrasound (IVUS) and optical coherence tomography (OCT). With both modalities the lumen can accurately be delineated. IVUS has a higher penetration depth than OCT, but cannot see past calcified spots and has a relative low resolution (approximately 200 um)[19]. Studies showed that IVUS can give information about wall constituent of plaques, but lipid-rich cores remain difficult to accurately identify[20,21]. OCT has a higher resolution -typically 10 um- and can image beyond calcified spots. Although great leaps are being made regarding to pull back speed of OCT, it remains necessary to flush the arteries before imaging[22]. Although the addition of intravascular imaging could potentially improve the success of screening strategies, it is currently not part of routine clinical care.

The diagnostic strategies described above focus on lumen intruding plaques. During the progression of coronary artery disease, atherosclerotic lesions grow outward rather than inward [4]. This means that a considerable amount of the atherosclerotic burden is present without intruding the lumen, and hence evades detection during routine screening. These lesions will not produce symptoms until a plaque ruptures and initiates a possible fatal thrombolytic event. This explains why the majority of the ruptures are not caused by highly stenotic lesions, but rather by the mildly diseased cases[23–25]. In this thesis, a mildly diseased coronary segment is defined as a segment containing plaques with a stenosis degree less than 50%, i.e. the typical cut-off value used in the first treatment strategy. Since the majority of the ruptures are caused by mildly diseased cases, screening methods should not just aim for finding the heavily stenosed cases, but also focus on identifying the plaques with a high rupture risk.

Rupture-risk

Two parameters can be associated with the rupture risk of plaques. Wall shear stress (WSS) is the frictional force exerted on the vessel wall by the flowing of blood. WSS is one of the key determinants in the onset and progression of atherosclerosis[26,27]. Sites exposed to low and/or oscillatory WSS have a high predilection to develop atherosclerosis[28,29] (Fig. 2a). Due to this propensity, atherogenesis often occurs in coronary bifurcations[30–33].

Plaques that subsequently progress into the lumen are exposed to changes in WSS distribution (Fig. 2b). Depending on the shape of a plaque, a lumen narrowing will result in relatively high WSS at the proximal shoulder and neck of the stenosis and low at the distal shoulder regions (Fig. 2c). Evidence suggests that in the low WSS zones at the downstream shoulder region plaques will continue to grow (Fig. 3c)[34]. At the proximal shoulder and the neck of the stenosis the high WSS initiates pathobiological degradation processes within the fibrous cap and thereby promoting plaque rupture[35,36]. This is in line with the observations that plaques predominately rupture just upstream of the neck of the stenosis[37–39]. So when searching for rupture-prone plaques, elevated WSS over a TCFA could be a potential prognostic marker for rupture-risk.

The second parameter that determines the rupture risk of a TCFA is cap thickness. From a mechanical perspective a cap ruptures if the stresses in the cap exceed a certain threshold value, i.e. the cap strength. Increased stress is therefore a mechanical characteristic for the rupture-risk of a plaque. Many studies focused on computing the wall stress within a cap in order to stratify risk[40–45]. The results of these studies show that
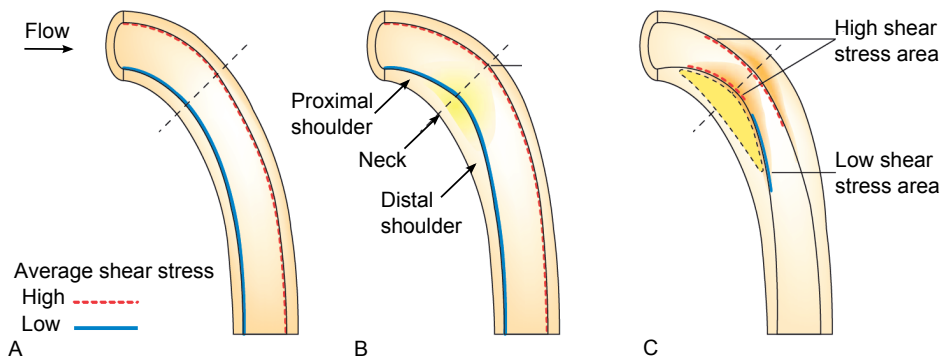
Fig. 2: Overview of atherosclerotic progression on coronary arteries and the subsequent changing WSS patterns. **A:** Curved healthy coronary artery with global WSS distribution, i.e. low WSS at the inner curve and high WSS at the outer curve. **B:** Development of atherosclerotic lesions at the inner curve. The growing lesion results in both outward and inward growth at the inner curve, but the luminal area is still largely preserved. **C**: In the more advanced state of atherosclerosis a lumen intruding plaque develops. This changes the WSS patterns over the plaque. The proximal shoulder and neck become exposed to high WSS, while the distal shoulder subject to low WSS. (Adjusted from Slager et al.[34])

there is a strong correlation between peak-cap stress and cap thickness. The thickness of a cap can thus serve as a marker for the rupture-risk of a plaque.

The combination of WSS and cap-thickness measurements could be valuable in assessing and managing coronary artery disease. To aid the identification of at-risk areas the two complementary risk factors can be merged into a single rupture-risk map.

How to determine the rupture-risk map

WSS is defined as the derivative of the velocity field near the vessel wall multiplied by the viscosity of the blood. WSS cannot be measured in coronary arteries: the resolution of velocity measurements is insufficient to accurately determine the velocity near the wall. The geometry of coronary arteries makes it very challenging to judge in vivo WSS patterns on geometry alone, even in the healthy state. To determine WSS patterns the curvature, bifurcations and the presence of stenoses have to be taken into account[46]. The only reliable technique to quantify WSS in coronary arteries is therefore computational fluid dynamics (CFD).

The second parameter that was introduced to evaluate rupture-risk was cap-thickness. In order to properly assess cap-thickness intravascular imaging methods are needed. To detect thin caps with IVUS remains challenging since the contrast between the wall constituents is low and the resolution not always suffices. OCT on the other hand has an excellent resolution to inspect cap-thickness[47]. The limited penetration depth is no issue for this particular goal since TCFAs are superficial by definition. Furthermore, recent studies introduced automated techniques to detect thin caps[48], which makes an introduction into the clinical setting in the near future conceivable.

This thesis focuses on evaluating WSS in mildly diseased segments since they contain plaques that can rupture but are typically not treated during routine percutaneous coronary intervention. Secondly, these regions are known sites for the onset of atherosclerosis. From a computational perspective coronary bifurcations are interesting as well. Many concepts needed to properly model WSS computations in one coronary bifurcation can be translated to model multiple subsequent bifurcations, i.e. (part of) the coronary tree.

In summary,
- Both cap-thickness and elevated WSS over a plaque are potential markers for rupture-risk.
- This is particularly interesting in mildly diseased coronary bifurcations.
- The combination of the two parameters in one rupture-risk map could proof valuable in detecting and managing mildly diseased segments coronary bifurcations

COMPUTED WALL SHEAR STRESS

With CFD the flow within a 3D domain is computed by solving the Navier-Stokes equations. Besides the material properties of blood two other requirements have to be met in order to perform CFD in coronary arteries: the 3D geometry and boundary conditions for the inlet and outlet(s) of the coronary segment. The 3D geometry of the coronary lumen has to be reconstructed based on imaging data. At the inlet and outlets, a hemodynamic parameter has to be prescribed (Fig. 3).

Geometry

The 3D geometry of coronary arteries can be acquired with different imaging modalities. Most commonly used in clinical practice are computed tomography angiography (CTA) and x-ray angiography. CTA is an emerging minimal invasive screening technology that generates 3D image data. X-ray angiography, or simply angiography, is the principle imaging technique for interventional cardiology. Data from CTA and angiography can be fused with intravascular techniques to get a more detailed reconstruction of the 3D geometry.

Fig. 3: Model of the coronary bifurcation. In order to compute the flow with CFD, the 3D geometry has to be reconstructed based on imaging data. For the inlet and the outlets boundary conditions need to be prescribed.

Computed tomography coronary angiography

CTA is the least invasive imaging technique that allows coronary artery reconstruction. It is based on the attenuation of x-rays, where the level of attenuation is used to differentiate between tissue types. Injection of a contrast agent is required to be able to differentiate between the lumen and the surrounding tissue. With multi-slice spiral CT scanning a patient is continuously advanced through a gantry with a rotating x-ray beam allowing for continuous data acquisition[49]. From the acquired 3D data an image is reconstructed. More recently 320-detector row scanners were introduced that bring a scan within a single heart beat within reach[50]. Although CTA depends on intravenous contrast injection and exposes a patient to radiation, it causes minimal discomfort. The resolution is good enough to visualize the lumen and determine the presence of critical stenoses[51]. It directly provides the 3D geometry including the side branches. For CFD application the typical resolution suffices but is not superb and also the blooming effects in the presence of calcium spots can interfere with a proper delineation of the
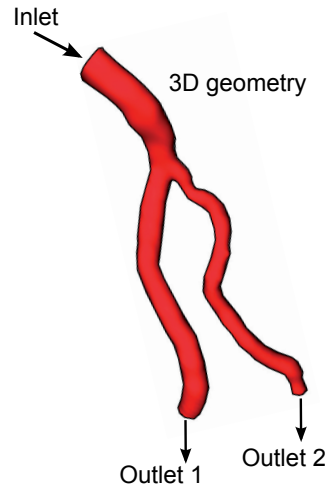
lumen[52]. Previous studies have applied CTA-based geometry reconstructions to perform WSS computations in human coronary arteries[53–57].

Coronary x-ray angiography

X-ray angiography is the imaging modality most commonly used during percutenous coronary intervention. It visualizes the anatomy of the coronary tree with x-rays and by injecting a contrast agent directly into the coronary artery via a catheter. The first coronary angiography was performed unintentionally by Sones in 1958. During routine angiography of an ascending aorta the catheter tip accidentally slipped into ostium of the RCA, where the released contrast agent directly provided a clear image of the lumen[58,59]. Sones and his coworkers realized the potential of this fortunate mistake and soon after they developed protocols for optimal viewing angles and percutaneous access. Since its introduction angiography rapidly became the standard for diagnosing coronary artery disease. To this day a diagnosis of coronary artery disease needs the confirmation of angiographic images[60]. The advancements in x-ray systems improved temporal and spatial resolution. Still, coronary angiography requires the insertion of catheters and contrast agents. It only permits a 2D inspection of the lumen and cannot provide information of the vessel wall. 3D reconstructions of coronary arteries are usually based on two or more projections from different angles[61–65]. These 3D reconstruction were proven suitable to compute WSS[66–73].

Fusion of imaging techniques

The most elaborate procedure to reconstruct the geometry fuses a 3D imaging technique with an intravascular one. IVUS and OCT give highly detailed information of the lumen, but the 3D anatomy of the vessel is not obtained. To get the best of both worlds, techniques were developed that fuse the imaging data from either angiography or CTA with the intravascular recorded data from IVUS or OCT (Fig. 4).

The first study that fused IVUS and angiography to create a 3D volume as a comprehensive visualization tool was done by Laban et al.[74]. By combining these 3D reconstructions with CFD the relationship between local hemodynamics and the evolution of atherosclerosis was studied[75–81]. WSS was also studied by combing OCT with angiography[82,83]. Toutouzas et al. and Papaflakis et al. compared WSS computed in reconstructions based on combing either OCT or IVUS with angiography and concluded that similar WSS results were computed[84,85]. Others derived the 3D backbone from CTA and combined it with luminal information obtained with IVUS[77,86]. One report has combined CTA data with OCT[87]. Two reviews by Bourantas et al. give an overview of all studies on the fusion of imaging techniques[88,89].

Although fusion techniques can lead to lumen reconstructions with higher accuracy, several drawbacks are present as well, especially for clinical applications. First, the re-
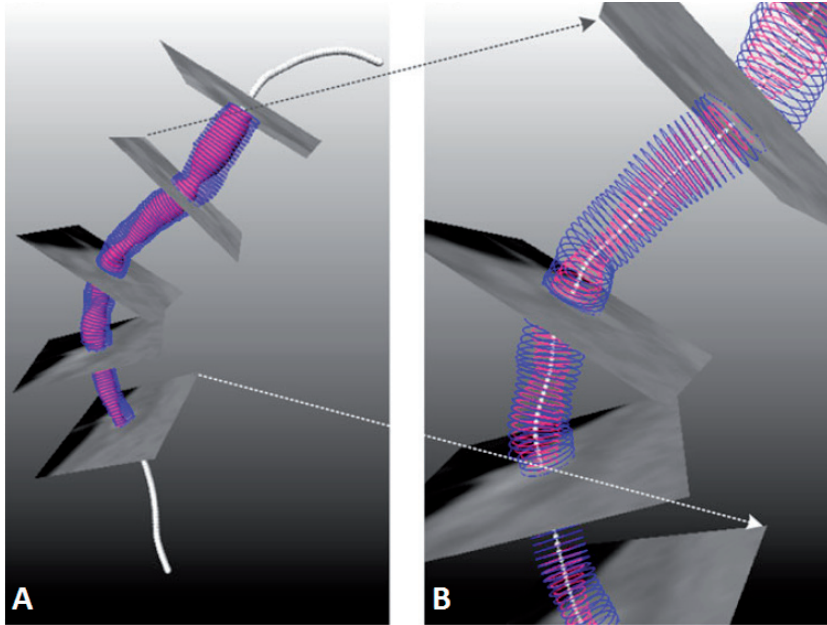
Fig 4: Example of fusion of CTA and IVUS data. The 3D centerline from the coronary artery is reconstructed from the CTA data. The square planes show the CTA data perpendicular to the centerline. The pink contours represent the lumen contours segmented from IVUS data, the blue contours the outer wall. These contours were aligned perpendicular to 3D centerline. **A:** Full view of the reconstructed centerline of coronary artery. **B:** Close up of the middle segment of panel A. (Adjusted from Van der Giessen et al.[86])

construction procedure is time consuming and cannot be performed online. Moreover, a single pull-back does not provide any information about the side branches. In order to incorporate side braches multiple pull backs are required. Finally, an OCT pull-back cannot be ECG-gated what makes it subjective to heart beat artifacts.

Boundary conditions

Boundary conditions are needed to be imposed in order to solve the Navier-Stokes equations. There are multiple possibilities to prescribe boundary conditions. First, it is possible to directly impose measured values. Second, reduced-order models can be coupled to the boundaries of the 3D domain. These models can incorporate various degrees of physics, (patho-) physiology and patient-specific parameters. Third, it is also possible to apply geometry-based scaling laws to impose as boundary conditions.

Measured boundary conditions

Hemodynamic data that can be used to define boundary conditions are pressure, velocity or flow measurements. X-ray angiography relies on insertion of a contrast agent.

With videodensitometry can directly provide a representative measure for coronary flow by tracking the propagation speed of the contrast agent. In TIMI-frame count the flow is quantified by registering the frame count in combination with the frame rate[90,91]. Although this techniques seems attractive because it does not need additional equipment, its precision is limited by the 2D observation of a 3D path and subjectivity in determining the wave front of the bolus[92].

Hemodynamic data can be measure invasively. A pressure wire is a catheter-mounted pressure sensor and they are commonly used to measure FFR. Catheter-based velocity measurements were also developed; most of them make use of the Doppler principle[93,94]. Alternatively, techniques were explored that are based on the principle of heat transfer and the sensitivity resistance of a piezo-electric crystal to that heat: thermodilution[95,96] and thermoconvection[97]. These techniques show great promise but are not yet ready for routine use during intervention. Subsequently, catheters became available that can simultaneously measure the pressure and velocity[98].

Improvements in temporal resolution and coverage of CT technology have led to the advent of dynamic CT-perfusion (CTP) imaging[99]. Myocardial perfusion is measured in time through imaging the uptake of the contrast agent by the myocardium. CTP is typically performed as a stress test to effectively detect myocardial ischemia. With the current standard of scanners a CTP measurement takes approximately 30 s with a temporal sampling interval of 2-4 s depending on heart rate. It has proven to be an effective measure for qualitative assessment of myocardial perfusion[100–102]. Since, it is a relatively new technique the verification of quantitative measure is still ongoing[102,103].

All the above mentioned measurements give direct patient-specific information. However, all reliable measurement techniques are at least minimal invasive or require the insertion of additional catheters.

Reduced-order models

An alternative to prescribing velocity profiles or pressure as a boundary condition are reduced order models[104–106] (Fig 5). The 0D models, or lumped-parameter models, define a locale relationship between pressure and flow often using electric circuit analogies. The main advantage is the lower numbers of parameters needed as input, in order to represent the properties distal vasculature. These 0D models can be used to make a full representation of the arterial system, using the distributed 0D approach[107,108]. Often though, the 0D models are combined with higher-order models to represent the main properties of the distal vasculature locally[109–111].

1D models, or pulse-wave propagation models, can be thought of as simplification of the full 3D formulation of the Navier-Stokes equations. Hughes et al. showed that by compounding the physics in a cross sectional direction a 1D formulation can be obtained[112]. This 1D formulation proved suitable to describe the pressure and wave

phenomena that occur in the arterial system[113–115]. Other approaches of formulating 1D wave propagations schemes can be based on Womersley's oscillatory flow theory[116] or electrical transmission line theory[117]. Previous studies showed the large range of possibilities of coupling the 3D to 1D formulations[118,119].

The reduced-order models can incorporate patient-specific parameters and are able to describe a broad range of pathophysiology of the heart, depending on the complexity of the models. They are able to capture time-dependent phenomena. Nonetheless, it should be noted that with higher levels of sophistication more patient-specific parameters are needed. The accuracy and added value critically depend on the accuracy of the parameters that describe the mechanical behaviour of the vasculature it is representing. Atherosclerosis for instance, focally affects the mechanical properties of coronary wall. It is not straightforward to find the proper distributed patient-specific parameters for 1D or 0D models to capture this effect.

Scaling laws

In 1926 Murray searched for a theoretical foundation that could explain why fluid transport systems in the human body are organized the way they are[120]. With the en-
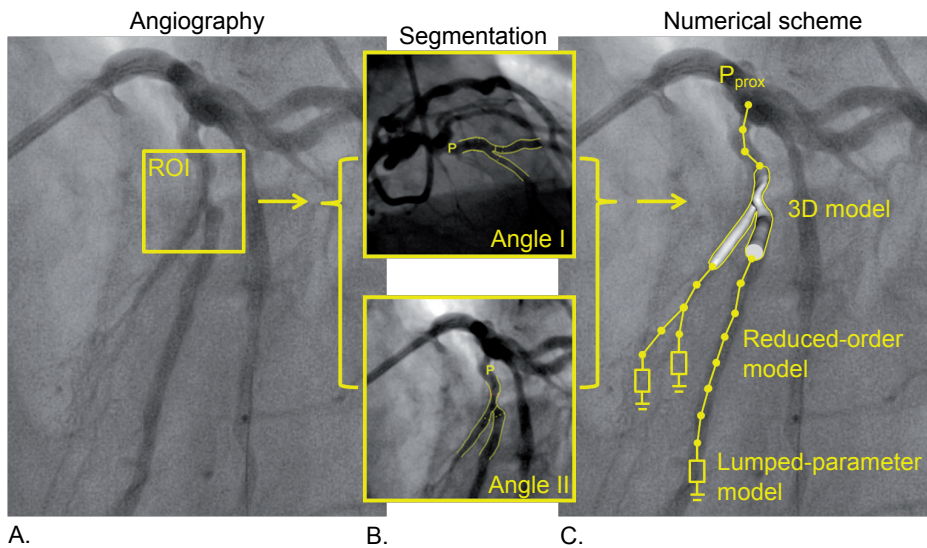
Fig 5: Example of a framework to couple reduced-order models to a 3D domain for WSS computations. A: Angiography image of coronary artery with stenosed segment, i.e. the region of interest (ROI). **B:** Two angiography images of the stenosed region at different angles. Based on these two images a 3D reconstruction suited for CFD computations can be made. **C:** Illustration of the computational scheme is superimposed on the angiography image. WSS can be computed with CFD in the 3D model. The dotted lines represent the epicardial vessels for which reduced-order models based could be used. The scheme is closed off proximally with pressure p_{prox}, and distally with a lumped-parameter model for the myocardium.

ergy balance at the basis he found a simple requirement for maximum efficiency in the circulation. That is that the blood flow (q) past any point in the system has the same cubed relation to the diameter (d³) of any vessel. This concept went almost unnoticed for nearly half a century until Sherman pointed out its validity in a large range of data from cardiovascular systems[121]. LaBarbera later contributed to the general acceptation of these ideas in biological systems[122]. Other investigators continued the work of Murray and found that the flow might be proportional to the diameters to a power different than 3 (dˣ). A power of 3 implies, apart for from minimizing the required energy for transport, that the WSS is constant throughout a system independent of the diameters. In system where the flow is proportional to diameter to the power of 2 the mean blood flow velocity is constant regardless of the diameter. For example in the study by Zamir et al. a power of 2 was found for the large branches of the aorta[123]. In this study a corrosion cast model was used in combination with assumptions on flow symmetry since flow measurements were not available.

For coronary arteries values for the exponent were reported between 2 and 3. Some examples of such studies are given here. In a report by Van Bavel and Spaan a computer model was constructed based on anatomy measurements of two swine hearts[124]. The model contained arteries with diameters ranging from 10 to 500 μm. A power of 2.35 was reported for the arteries in their model greater than 200 μm. In a similar approach by Mittal et al. flow was simulated in a computer model of a swine heart having the full range of diameters, from the large vessels down to the capillary level[125,126]. Here a power ranging from 2.1 to 2.2 was found for the three major arteries. Zhou et al performed videodensitometry measurements in swine hearts and reported a value of 2.7[127]. In another study by Zhou et al. the authors defined more elaborate design rules by accounting for the resistance of the distal vasculature. In the report by Kassab these design rules were investigated using multiple datasets of different parts of the vascular system of different species[128]. For the major branches of the coronary tree of a swine the x ranging from 2.39 to 2.43 was reported.

Doriot et al. performed a series of *in vivo* measurements of coronary flow in human coronary bifurcations suspected of atherosclerosis[129]. The combination of both measured flow and diameter in a patient group were used by Van der Giessen to derive[130]:

$$q = 1.43d^{2.27}$$

$$\frac{q_2}{q_1} = \left(\frac{d_2}{d_1}\right)^{2.55}$$

Here d1 is the diameter of the larger daughter vessel of a bifurcation and d2 the diameter of the smaller daughter. Similarly, q1 is the flow in the larger daughter vessel and q2

the flow in smaller branch. The main advantage of these relations is that only a diameter (d) measurement is needed to estimate flow or flow distribution. Imaging data can thus suffice to prescribe boundary conditions. Murray's law was used by other investigators to set the outflow conditions[55,131–134]. However, since it is based on solely the diameter it uses relatively little patient-specific information. When an outflow ratio is prescribed as a boundary condition the transient flow phenomena caused by the distal vasculature cannot be captured. Note that outflow ratio as outlet boundary condition cannot be combined with a pressure inlet boundary condition, but the flow rate at the inlet needs to be prescribed.

Computational fluid dynamic for coronary flow

The relationship between WSS and human coronary atherosclerosis was the topic of many studies. These studies were reviewed recently[27]. Most of these studies relied on the fusion of biplane angiography and IVUS for the 3D reconstruction of the lumen, and they applied a variety of boundary condition, ranging from TIMI flow count to invasive Doppler measurements. They resulted in valuable insights regarding the impact of low WSS and the early localization of atherosclerotic plaques and the remodelling towards more advanced lesions[29,135,136]. Furthermore, these studies were used to gain insight on the influence of WSS on neotintima formation after stent placement[76,137–139]. Both research teams computed the flow in between (major) side branches, thereby omitting potential interesting bifurcated areas that are known sites for the onset of atherosclerosis.

In the studies by Samady et al. and Eshtehardi et al. the side branches were taken into account[46,75]. The reconstructions were again made using angiography and IVUS data, but the inflow and outflow boundary conditions were prescribed using flow intravascular flow measurement. The study by Samady et al. showed that regions exposed to low WSS develop greater plaque and necrotic cores progression. The data further suggested that the regions exposed to high WSS over a plaque will lead to a more vulnerable plaque phenotype, similar to what Gijsen et al found[140]. Remarkably, Eshtehardi et al. found that also low WSS is associated with vulnerable plaque phenotype.

All these techniques that correlate computed WSS to a marker of atherosclerosis have so far only been used for research goals. Clinical application is currently not feasible. For this the reconstruction of the 3D geometry is still time-consuming and requires special training and therefore the procedure cannot be performed online yet.

An example of CFD that has further advanced towards clinical application is computed FFR using CFD, instead of in vivo measurements during intervention. Taylor et al. devised an approach which computed FFR based on CTA-images that could be acquired prior to invasive intervention[141] (Fig. 6). This method evolved in software that was approved

for clinical use. In three large scale clinical trials the method showed a high accuracy in determining if the FFR was either positive or negative[142–144]. Other investigators later introduced methods to compute FFR based on angiography images[145,146]. The advancement made in computed FFR as a clinically approved tool for diagnosing coronary hemodynamics shows the potential of applying CFD in routine clinical practice[147].

OUTLINE

The work in this thesis was carried out in the context of the project 'Fusion of imaging parameters for prediction of plaque rupture in human coronary arteries' funded by the Dutch technology foundation (Stichting Technische Wetenschappen). The aim of that project was to develop a clinical tool that combines two imaged-based risk factors in one risk map, i.e. angiography-based WSS and cap-thickness from OCT. The fact that the WSS computations are developed for a clinical setting requires them to be fast and cost-effective.
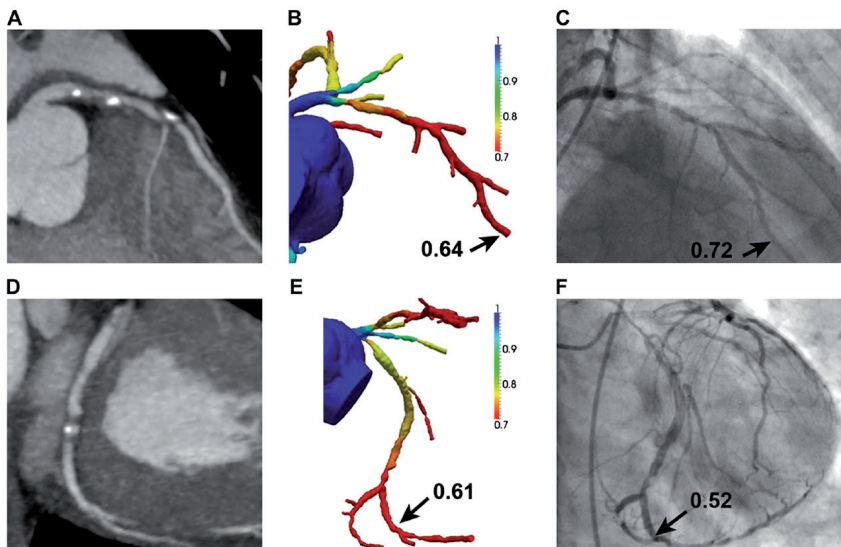
Fig 6: Example of computed FFR based on CTA data with the method developed by Taylor et al. in a 66-year-old man with multivessel coronary artery disease. **A:** CTA demonstrating stenosis in the LAD. **B:** The computations results in an FFR of 0.64. **C:** Angiography projection of the LAD. The FFR measured in vivo results in 0.72. **D:** CTA demonstrating stenosis in the LCx. **E:** The computations results in an FFR of 0.61. **F:** Angiography projection of the LAD. The FFR measured in vivo results in 0.52 (Adjusted from Taylor et al.[141])

Fusion techniques that combine imaging data from different modalities result in 3D reconstruction with the highest level of detail. So far the detailed visualizations and reconstructions have been applied for research goals only. The barrier towards mainstream clinical application can largely be attributed to the fact that generating the 3D reconstruction is still time-consuming, requires special training and needs insertion of additional catheters. Also addition of side branches remains troublesome because this requires multiple pull backs. On the other hand, WSS can potentially quickly be obtained when reconstructions are based on angiography alone. The size of the 3D domain in which the flow is computed strongly influences the computational time. The time to compute WSS can be minimized by choosing the size of the 3D domain wisely in combination with appropriate boundary condition. Reduced-order models and scaling laws have both proven valuable as boundary conditions. Again taking the concept of making WSS quickly available, these boundary conditions should preferentially be based on angiography.

The aim of this work was to develop tools to assess WSS in human coronary bifurcations. In particular it was investigated how non-catheter-based imaging data can best be applied to extract patient-specific WSS patterns in mildly diseased human coronary bifurcations. In chapter 2 the influence of reconstruction errors in angiography-based 3D reconstruction on WSS is investigated. In chapters 3 and 4 two modelling approaches are presented that can serve as more advanced models for boundary conditions and be coupled to 3D computations. Chapter 5 covers the effect of applying scaling laws for outflow boundary conditions using CTP flow measurements. In chapter 6 both the inlet and outlet boundary conditions were scaled compared to fully measured boundary conditions derived from intravascular measurements. Finally, in chapter 7 a risk-map is composed based on WSS patterns in combination with cap-thickness measurements from OCT.
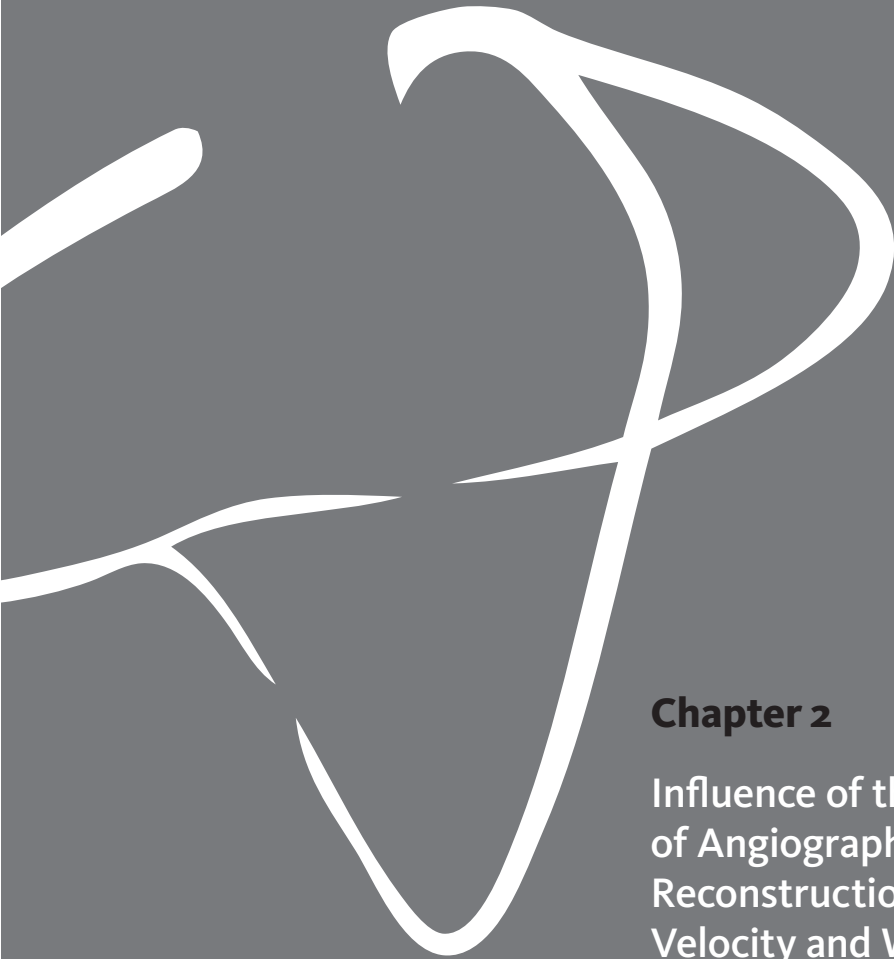
Chapter 2

Influence of the Accuracy of Angiography-Based Reconstructions on Velocity and Wall Shear Stress Computations in Coronary Bifurcations: A Phantom Study

ABSTRACT

Wall shear stress (WSS) plays a key role in the onset and progression of atherosclerosis in human coronary arteries. Especially sites with low and oscillating WSS near bifurcations have a higher propensity to develop atherosclerosis. WSS computations in coronary bifurcations can be performed in angiography-based 3D reconstructions. It is essential to evaluate how reconstruction errors influence WSS computations in mildly-diseased coronary bifurcations. In mildly-diseased lesions WSS could potentially provide more insight in plaque progression.

Four Plexiglas phantom models of coronary bifurcations were imaged with bi-plane angiography. The lumens were segmented by two clinically experienced readers. Based on the segmentations 3D models were generated. This resulted in three models per phantom: one gold-standard from the phantom model itself, and one from each reader. Steady-state and transient simulations were performed with computational fluid dynamics to compute the WSS. A similarity index and a noninferiority test were used to compare the WSS in the phantoms and their reconstructions. The margin for this test was based on the resolution constraints of angiography.

The reconstruction errors were similar to previously reported data; in seven out of eight reconstructions less than 0.10 mm. WSS in the regions proximal and far distal of the stenosis showed a good agreement. However, the low WSS areas directly distal of the stenosis showed some disagreement between the phantoms and the readers. This was due to small deviations in the reconstruction of the stenosis that caused differences in the resulting jet, and consequently the size and location of the low WSS area.

This study showed that WSS can accurately be computed within angiography-based 3D reconstructions of coronary arteries with early stage atherosclerosis. Qualitatively, there was a good agreement between the phantoms and the readers. Quantitatively, the low WSS regions directly distal to the stenosis were sensitive to small reconstruction errors.

INTRODUCTION

Atherosclerosis is a chronic disease of the arterial system which leads to plaque formation. Plaque formation is a focal phenomenon, characterized by the accumulation of (low-density) lipoproteins, inflammatory cells and extra-cellular matrix in the arterial wall[1]. At first this process leads to thickening and outward remodeling of the arterial wall, which can subsequently progress to growth of plaque into the lumen. Rupture of plaques located in coronary arteries trigger thrombotic events, which are the main cause of acute myocardial infarction[2]. Understanding plaque development, progression and rupture is therefore of great clinical importance.

In the earliest phase of the disease, plaque development is triggered in zones of low or oscillatory wall shear stress (WSS)[3]. Especially sites near bifurcations or with a high curvature are prone to develop plaques. The largest study focusing on the effect of WSS on the progression of atherosclerosis in human coronary arteries was published by Stone et al.[4]. They investigated the role of WSS on plaque growth in 824 coronary arteries. They found that low WSS was an independent predictor of increased plaque burden and luminal obstruction over a 6 month period. Identification of low WSS regions in a clinical setting can therefore help identifying arterial segments that are prone to harbor progressing plaques leading to lumen narrowing. The role of WSS in the final phase of the disease process –plaque rupture- is less well established. Recent studies however indicated that increased WSS is related to changes in plaque composition that enhance plaque vulnerability[5–7]. These preliminary data are supported by clinical observations that regions exposed to elevated WSS are associated with the location of plaque rupture[8–11]. In summary, low WSS is associated with plaque progression and clinical lumen narrowing, while high WSS is potentially important to identify plaque locations that are at increased risk for plaque rupture.

WSS in coronary arteries cannot directly be measured in-vivo, but it can be computed with computational fluid dynamics (CFD). In order to perform CFD the geometry of the lumen is required, together with the inflow and outflow boundary conditions and the properties of the blood. Previous studies used a combination of angiography and intra-vascular ultrasound (IVUS) to reconstruct coronary arteries [12–14]. IVUS enabled high resolution reconstructions of the lumen. Nonetheless, reconstruction techniques using IVUS are time-consuming and require an additional catheter. The preferred imaging technique during percutaneous coronary interventions is angiography, which visualizes the lumen of coronary arteries. Reconstructions of coronary arteries can be made in real-time based on bi-plane angiography[15,16]. It was previously shown that accurate reconstructions can be made based solely on angiography[17] and they can potentially serve as the basis for WSS computation during clinical interventions[18–20]. The 3D reconstructions are based on segmentations on the two 2D projections. One of the main

sources of errors in the reconstructions arises from inaccuracies of the segmentations by readers, what in turn is related to the resolution constraints. These reconstruction errors consequently influence the outcome of CFD.

Other studies explored the influence of imaging procedures on CFD results in coronary arteries. Most of these studies did not include ground truth data[20–25]. The study of Wellnhofer et al. on 3D coronary reconstruction based on angiography does not have ground truth data either, but they compare coronary reconstructions based on segmentation from different readers, concluding that the average difference is small[26]. However, the standard deviations reported in that study are fairly large, potentially leading to large differences in WSS. Goubergrits et al. used phantoms to validate image-based reconstruction procedures on geometry and WSS patterns[27]. They found that although the differences between the outer surfaces of the geometries were not negligible, WSS patterns were not affected significantly due to reconstruction inaccuracies[19]. This study focused steady flow simulations in a single scaled up healthy left coronary bifurcation model without atherosclerotic disease. Furthermore, the influence of user input on the segmentation procedure was not investigated.

The aim of this study was to analyze the effect of reconstructions errors on computed velocity and WSS in mildly-diseased coronary bifurcations using phantom models[28]. Mildly-diseased coronary arteries were investigated because these sites are affected by atherosclerosis but are normally left untreated. WSS can potentially give insight in the progression to more advance lesions and rupture risk. Secondly bifurcated regions were chosen. Although they are more difficult to reconstruct in 3D than single vessel segments, they are also more interesting since they are predilection sites for the onset of atherosclerosis. The phantom models were imaged with bi-plane angiography and two clinically experienced readers segmented lumen on the images. Based on the segmentations 3D reconstructions were made which were used for CFD computations. The simulations were performed to assess steady WSS, time-averaged WSS (TAWSS) and the oscillatory shear index (OSI). Computations were first performed in the original design of the phantom models and the results served as the ground truth. The results were quantitatively compared to those from computations in the 3D reconstructions.

METHODS

Phantoms

Plexiglass phantom models of diseased coronary bifurcations with concentric stenosis were previously created (Fig. 1A)[28]. With computer-aided design three subsequent bifurcations were modeled, having at least one stenosis per bifurcation with the stenosis degree ranging from 40% to 80%. The phantoms had representative branch and stenosis
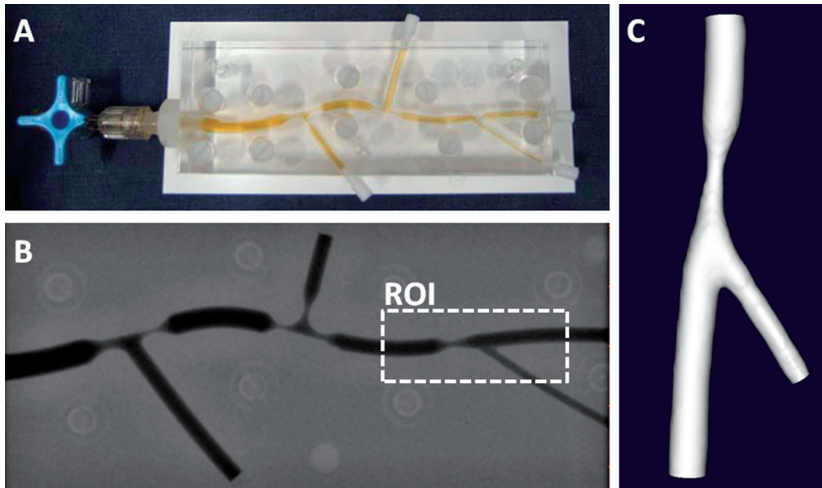
Fig 1: Overview of the 3D reconstruction steps of a phantom model with bi-plane angiography. **A:** Original phantom model filled with contrast agent. **B:** An angiography recording of the phantom. A region of interest (ROI) is indicated around a section that can be regarded as mildly stenosed. **C:** Final 3D reconstruction.

lengths, diameters, and bifurcation angles. This study focused on flow phenomena in mildly diseased bifurcations. Four phantoms each had one bifurcation region that was representative for that status. These four regions of interest (ROI) consisted of a side branch and one stenosis in the main branch having an area stenosis of 60%. In three cases the stenosis was proximal to the side branch and in one case distal. The fabrication process of the phantom models was described in detail in Girasis et al.[28]. Briefly, the phantoms were designed with a computer-aided design program. The 3D models were used to instruct a computer controlled milling machine to mill these models in Perspex (Plexiglass). The accuracy of the machining process was reported to be within 10μm.

Imaging & Reconstruction

Digital angiograms were acquired with a bi-plane angiography (Axiom ArtisTM; Siemens, Forchheim, Germany). The phantoms were filled with contrast agent (100% Iodixanol 320, VisipaqueTM, GE Healthcare, Cork, Ireland) and imaged in a 20 cm field of view (Fig 1A &B)[17]. Of each phantom one set of bi-plane angiography images was selected. The angles were selected to achieve the best possible quantification of the side branch length and angle, as well as the degree of stenosis. The phantoms were acquired with a resolution ranging from 0.17 to 0.21 mm. The contrast-filled lumens in the 2D images were segmented by two clinically experienced readers blinded to the original geometry (AK, NvD). Based on the segmentations 3D models were generated with validated commercially available software: Cardiovascular Angiography Analysis System (CAAS v5.11, Pie Medical Imaging, Maastricht, the Netherlands[16,17]).

Mesh

First, the computer-aided designs of the phantoms were used to generate surface meshes of the ROI of the phantoms. Next, based on the 3D reconstructions of the two readers, surface meshes were generated using a newly developed module within the CAAS software package. A grid dependency study was performed prior to the final simulation. In subsequent steps the grid size was decreased until the pressure and wall shear stress did not differ more than 3% for each node. In particular attention was paid to the zone distal of the stenosis. This resulted in a typical cell size of 0.08 mm. Additionally a prism layer of 5 elements was added at the wall. The final mesh size was typically 3.10^6 cells per mesh depending on the volume of the lumen (ICEM-CFD 14.5, Ansys Inc, Canonsburg, US). This resulted in three meshes per phantom: one gold-standard from the phantom model itself, and one mesh from each reader. From now on these models will be referred to as: phantom, reconstruction 1 and reconstruction 2. The radii of the reconstructions were acquired with VMTK (VMTK, Orbix, Bergamo, Italy) and compared to the radii of the phantom models. The mean Hausdorff distance between each point on the surface of phantoms and the surface of the reconstructions was computed using MeshLab (v1.3.3, open-source, http://meshlab.sourceforge.net/)

Computational fluid dynamics

Steady-state and transient CFD computations were performed with a commercially available finite volume solver (Fluent v14.5, Ansys Inc, Canonsburg, US). For the steady-state computations a Poiseuille profile was defined at the inlet of all models with a peak velocity of 15 cm/s, representative for normal physiological flow[29]. At the inlet this resulted in a Reynolds number of approximately 60 and at the stenosis approximately 200. For the transient simulations, typical flows curves of the coronary circulation were generated with a model developed by Bovendeerd et al.[30]. The flow cycles were defined to be 0.8 s. The flow curves were scaled such that the average flow corresponded to the flows in the steady-state simulations. Womersely profiles were prescribed at the inlet. Two full cardiac cycles were computed. Pilot studies showed that start-up effects were absent in the second cardiac cycle. Each flow cycle consisted of a 100 time steps. At the outlets of the bifurcations the flow ratio was defined using a diameter-based scaling law[31]. The wall was modeled as rigid. The blood was modeled as a non-Newtonian fluid using a Carreau model with the parameters taken from Cho and Kensey[32], and a density of 1060 kg/m3.

Wall Shear Stress analysis

The 3D WSS magnitude ($|\vec{\tau}|$) at the wall was extracted from the results of the steady-state computations. From the transient computations the 3D WSS vector ($\vec{\tau}$) was extracted, which was used to compute the time-averaged WSS (TAWSS):

$$\text{TAWSS} = \frac{1}{T}\int_0^T |\vec{\tau}|\,dt$$

In order to identify regions with oscillatory flow, the oscillatory shear index (OSI) was used [33]:

$$\text{OSI} = \frac{1}{2}\left[1 - \frac{\left|\int_0^T \vec{\tau}\,dt\right|}{\int_0^T |\vec{\tau}|\,dt}\right]$$

The OSI has a range from 0 to 0.5. Positions at the wall that experience flow in one consistent direction have an OSI of 0. An OSI of 0.5 is indicative of flow in two opposite directions alternating equal amounts of time during a cycle. TAWSS and OSI showed to provide complementary information [34]. TAWSS is indicative for the average WSS magnitude throughout a cardiac cycle, while OSI identifies regions exposed to oscillatory flow regardless of the magnitude of WSS. Both TAWSS and OSI were designed to identify regions at risk of developing plaque[35]

Previous investigations have established a cut-off of 0.5 Pa for low WSS. Areas exposed to WSS below this threshold can be regarded to be at risk. To resulting areas of low WSS in the phantoms (lWSS$_{phantom}$) and in the reconstructions from the readers (lWSS$_{reader}$) were compared using the similarity index (SI)[31]. This index determines the overlap of the areas and is defined as:

$$SI = \frac{2(lWSS_{phantom} \cap lWSS_{reader})}{lWSS_{phantom} + lWSS_{reader}}$$

The SI ranges between 0 and 1, where 0 indicates no overlap and 1 indicates full overlap. The SI values for the steady-state computations were presented. Because the areas exposed to TAWSS below 0.5 Pa were small, minor deviation could quickly lead to misrepresentative SI values.

A second quantitative analysis was comparing the axial and circumferential means per region of the bifurcations. Three regions were investigated separately: the proximal region, the stenosis region and the distal region. The proximal and distal regions were defined as the region where the diameter of the phantom was constant (Fig. 2&3). Wentzel et al. showed that relevant information can be extracted from the axial mean at 22.5° intervals[36]. Stone et al. showed that taking the full circumferential mean is useful to derive clinically relevant information from WSS computations[4]. The 3D WSS maps were converted to a 2D coordinate system to allow for a direct quantitative comparison. First, planes were defined perpendicular to the centerline at 0.45 mm intervals. Those planes
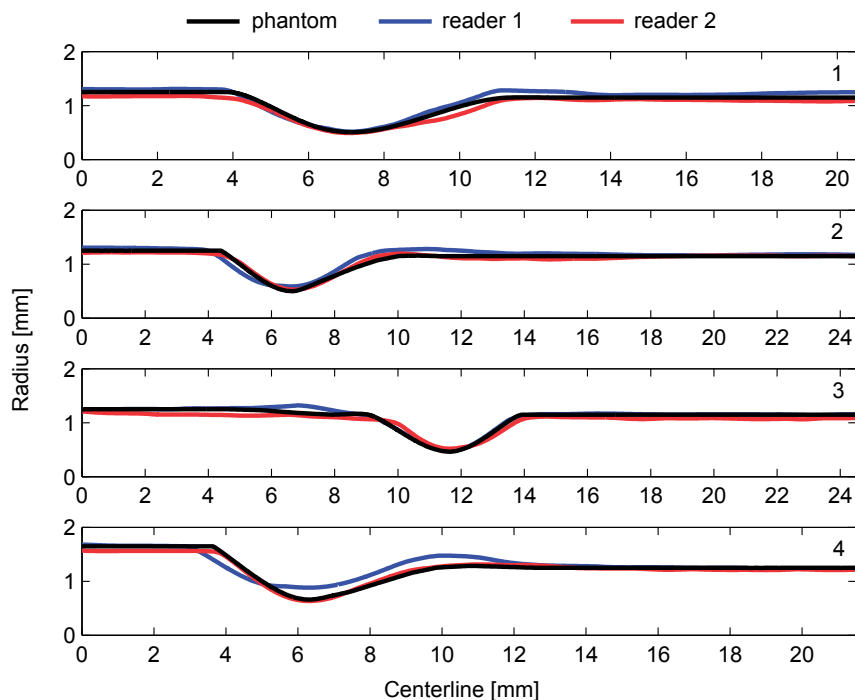
Fig 2: The radii of the main branch of the four original phantom models and of the two reconstructions based on the segmentation by the two readers.
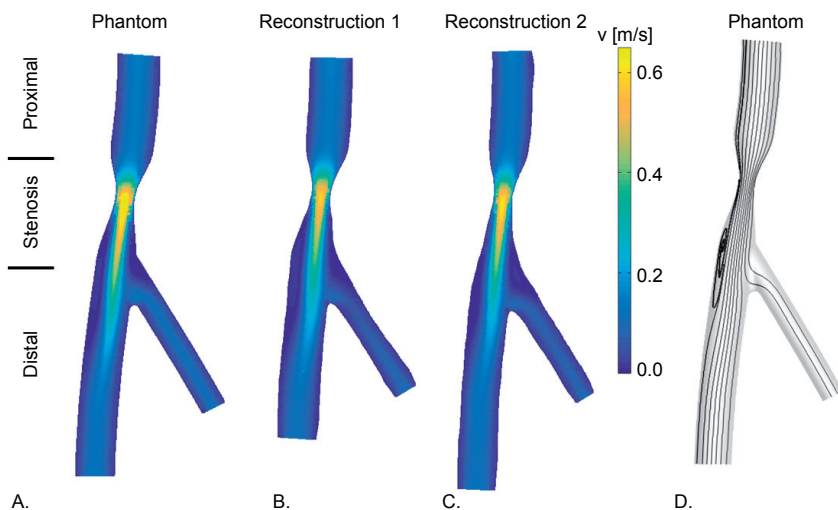
Fig 3: The velocity results of the CFD computations in a plane through the center of phantom 1 and its two reconstructions. In all models a jet forms at the neck of the stenosis and directly distal of the stenosis a recirculation zone is observed. **A:** Results in the phantom model. **B:** Reconstruction based on the segmentations from reader 1. **C:** Reconstruction based on the segmentations from reader 2. **D:** General streamlines observed in the computations.

were subdivided in 22.5° intervals. The average WSS values within the resulting bins were mapped to a 2D representation. The 2D maps from the phantom and two readers were clipped to represent identical areas.

Statistics

In order to test if two methods provided equal outcomes, a noninferiority test was employed[37]. A significance level of α=0.05 rejects the null hypothesis which states that the absolute WSS difference between the phantom and the reader is larger than a chosen margin. In this study that margin was based on the resolution limitations of angiography and the effect this has on the precision with which WSS can be computed. The WSS is defined as the derivative of the velocity normal to the wall. With a definition for the velocity profiles in the proximal region given by Schrauwen et al., an analytical expression for the WSS was derived[38]:

$$\tau = \frac{q(\beta + 2)\mu}{\pi a^3}$$

Here μ was viscosity and the wall was defined at r=a. Parameter β describes the shape of the velocity profile and q is flow. Due to the resolution limitation of angiography there is an uncertainty δ on the wall reconstruction:

$$a' = a \pm \delta$$

This directly affects the computed WSS:

$$\tau' = \tau(a')$$

The relative error ($\hat{\varepsilon}$) between the actual WSS and the WSS computed using the reconstruction therefore becomes:

$$\hat{\varepsilon} = \left(1 - \frac{\tau'}{\tau}\right) * 100\%$$

In a coronary artery with a radius of for example 1.25 mm and an angiography system with a resolution of 0.1 mm, the relative error ranges from -28% to 21%. From the analytical solution we know that in the proximal and distal regions the WSS is in the order of 1 Pa. With a conservative assumption of ±25% for the relative error, the equivalence margin was set at 0.25 Pa.

Due to more complex definition of OSI it is challenging to define an equivalence margin. Nonetheless, the maximum in the axial and circumferential means of the OSI were 0.2. With the ±25% relative error in mind, the equivalence margin for OSI was set at 0.05. This value is in accordance with a previous study stating that an OSI of 0.05 is not considered physiological significant[39].

The overall agreement of the WSS was assessed per region. To this end the percentage of area was reported where the computed WSS difference was less than the defined equivalence margin.

RESULTS

Fig. 2 shows the radius in the phantom and two readers of the four phantoms. For both readers the mean absolute difference ($<\delta r>$) between the radius of the phantom and the radius of the reconstructions was less than 0.10 mm (Table 1). Only the reconstruction by reader 1 of the stenosis in phantom 4 had a difference of 0.21 mm. In 7 out of 8 the mean Hausdorff distance was within 0.20 mm, and in only one reconstruction this was 0.23 mm. The flow rates in the simulation were based on an inlet peak velocity of 15cm/s. The inflow is acquired by multiplying the velocity with the inlet area. The deviations in the reconstruction of the inlet area resulted in different inflow rates.

Velocity

The flow rates in the simulation were based on an inlet peak velocity of 15cm/s. By multiplying the velocity with the inlet area the inflow is acquired. The deviations in the reconstruction of the inlet area resulted in different inflow rates. Fig. 3A-C shows the computed velocity fields of the steady-state computations in a plane through the center of phantom 1 and the two reconstructions as an example. In all three reconstructions a jet formed at the stenosis, with a peak velocity of 0.69 m/s, 0.59 m/s and 0.63 m/s in the phantom and two reconstructions respectively. Fig. 3D illustrates the streamlines in these geometries. Downstream of the stenosis a recirculation zone was formed and the main direction of the jet was shifted towards the opposite wall. The deviations observed in the reconstruction of the stenosis region, caused alterations in the length and width of the recirculation zone. The transient computations showed a similar velocity field. The recirculation zone was present during the whole cycle, but differed in size due to the pulsation.

	<δr> prox [mm]	<δr> sten [mm]	<δr> dist [mm]	Length stenosis [mm]	Mean Hausdorff distance [mm]	Area Stenosis [%]	Inflow [ml/s]	outflow ratio [%/%]
Phantom 1								
CAD				7,5		60.0	0.37	25 / 75
Reader 1	0.05±0.00	0.01±0.01	0.08±0.03	7,5	0.14	60.4	0.40	25 / 75
Reader 2	-0.08±0.00	-0.01±0.00	-0.04±0.02	7,9	0.14	58.0	0.32	20 / 80
Phantom 2								
CAD				7,0		60.0	0.37	24 / 76
Reader 1	0.03±0.04	0.07±0.01	0.05±0.03	6,4	0.16	54.1	0.38	23 / 77
Reader 2	-0.04±0.01	0.02±0.02	-0.02±0.02	5,8	0.12	56.5	0.34	22 / 78
Phantom 3								
CAD				5,0		60.0	0.37	24 / 76
Reader 1	0.01±0.01	0.03±0.01	0.01±0.01	5,1	0.20	61.0	0.35	23 / 77
Reader 2	-0.08±0.02	0.05±0.01	-0.07±0.01	4,8	0.10	56.6	0.33	24 / 76
Phantom 4								
CAD				6,5		60.0	0.64	48 / 52
Reader 1	0.02±0.01	0.21±0.01	0.10±0.34	7,0	0.23	47.2	0.64	48 / 52
Reader 2	-0.08±0.00	-0.03±0.01	0.03±0.12	6,5	0.12	59.4	0.58	45 / 55

Table 1: Characteristics of the reconstructions of the four phantoms based on the segmentations of two readers. The mean absolute difference (<δr>) between the radius of the phantom and the radius of the reconstruction is analyzed in the proximal, stenosis and distal region.

Wall shear stress

2D representations of the 3D WSS results in the main branch of phantom 1 are given in Fig. 4. The color maps are saturated to visualize the low WSS patterns. The white areas correspond to the location of the side branches (asterisk). Fig. 4a shows the WSS magnitude from the steady-state computations in the phantom. In the proximal region the WSS was fairly constant. Distal of the stenosis a crescent-shaped area of low WSS occurs, caused by the recirculation zone. The area between the white dashed lines had retrograde flow near the wall. The point where the WSS is zero indicates the transition to antegrade flow downstream of the crescent-shaped area. The differences in the low WSS patterns between the phantom and the reconstructions are related to the differences seen in the jet formation and the resulting recirculation zone (Fig. 4B-C). The area of low WSS in reconstructions 1 was skewed caused by a slight offset in the angle of the side branch, and in reconstruction 2 this was smaller. Directly distal of the stenosis in reconstructions 1 and 2 the transition to low WSS shows a ridged edge caused by unevenness in the reconstructions. The TAWSS had the same pattern as the WSS, although the mean TAWSS and its gradients were lower due to the pulsation of the flow (Fig. 4D-F) The pulsation also resulted in a point in the distal region subjected to high oscillatory flow, having an OSI of 0.5 (Fig. 4G-I). The crescent-shaped zones of elevated OSI corresponded to the zones of low WSS and low TAWSS.

As a quantitative comparison the areas exposed to low WSS in the phantoms and the reconstructions were compared. In the steady computations on average 11.5% of the phantom was exposed to low WSS, in reader 1 this was 14.8% and in reader 2 this was 12.8%. Hence, the mean difference of area exposed to low WSS was 2.8 percentage points. In the transient computations on average 6.8% of the phantom was exposed to low TAWSS, this was 13.3% for reader 1 and 10.0% for reader 2. For the transient computations the mean difference was 5.1 percentage points.

In Fig. 5 the SI of WSS is analyzed for phantom 1.Panels A-C show contour plots of the WSS in phantom and the 2 reconstructions. The crescent shaped areas of low WSS in the distal regions qualitatively match, but the location of the low WSS is influenced by the reconstruction errors. In Fig.5 panels D and E give a visualization of the SI. The

Fig 4 → : 2D maps of the WSS, TAWSS and OSI in the main branch phantom 1. The arrow indicates the stenosis and the asterisk the location of the side branch. **A-C:** Results of the WSS in the phantom (A), reconstruction 1 (B) and reconstruction 2 (C). The color map was saturated to visualize the low WSS. In the area directly distal to the stenosis there was retrograde flow (in between the white dashed lines). The crescent-shaped line where the WSS is zero indicates the transition from retrograde to antegrade flow. **D-F:** TAWSS results. Similar patterns were observed as for the WSS, although for the TAWSS the results were more averaged out. **G-I:** OSI results. Due to the pulsatility a zone of high oscillatory shear is formed in the distal region. This zone is indicative for the movement of the transition zone from retrograde to antegrade flow throughout a cycle.
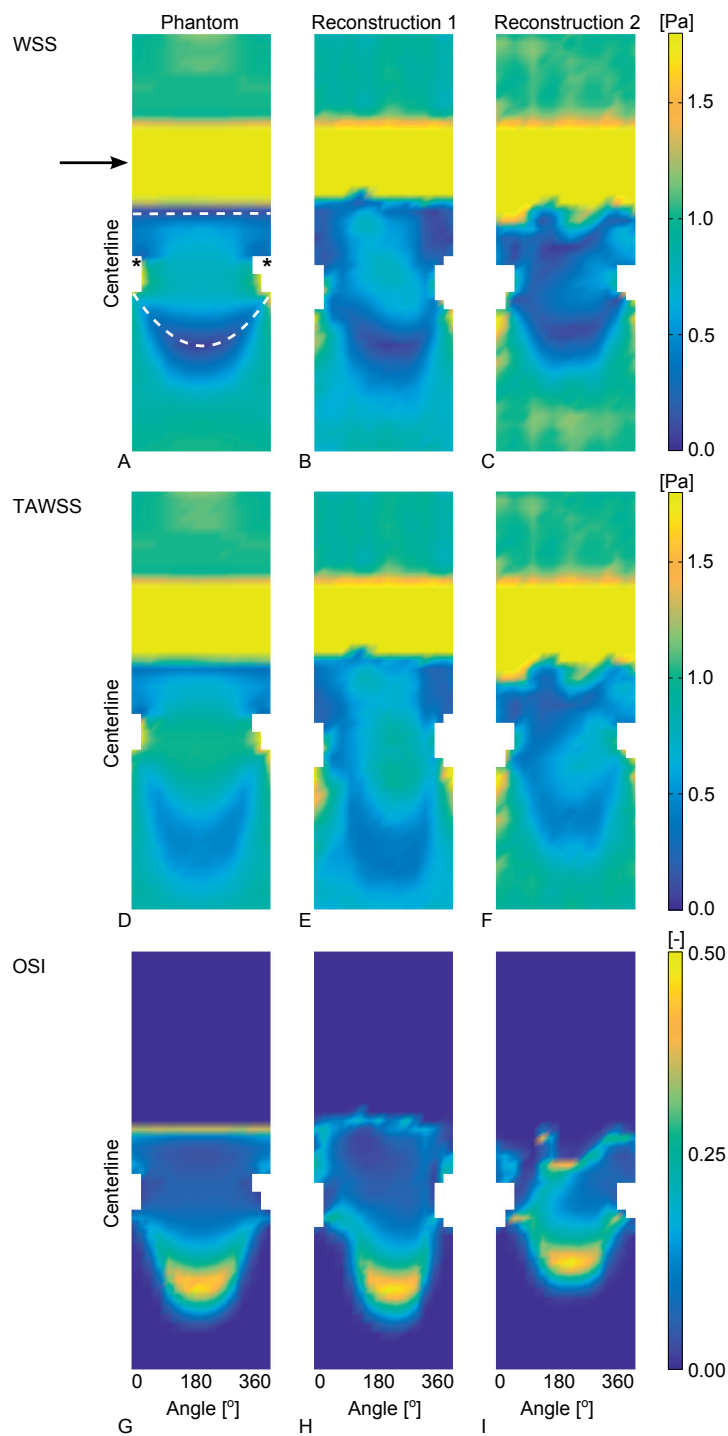
Fig 4

white areas indicate where the WSS was above 0.5 in both the phantom and one of the reconstructions, and the black areas indicates where the WSS was lower than 0.5. The gray areas in panels D and E indicate low WSS in only found in either the phantom or the reconstruction. The SI for the reconstruction 1 was 0.76 and for reconstruction 2 this was 0.46. In Table 2 all SI values are given. In phantom 1 and 3 a relatively high SI was found for the steady-state computations. In phantom 2 the SI was reasonable and in phantom 4 it was low.

The mean absolute differences in WSS between the four phantoms and their reconstructions were computed. The mean absolute WSS difference in the proximal regions ranged from 0.05±0.04 Pa to 0.17±0.06 Pa. In the stenosis region this ranged from 0.73±1.14 Pa to 2.59±4.00 Pa, and in the distal region from 0.12±0.15 Pa to 0.36±0.42 Pa. This lead to average absolute difference of the two readers in the four phantoms of 0.08 Pa in the proximal region, 1.34 Pa in the stenosis region and 0.20 Pa in the distal region. The TAWSS resulted in similar differences; on average the differences in the proximal, stenosis and the distal region were 0.09 Pa, 1.59 Pa and 0.23 Pa respectively. The OSI in the proximal region was 0 and no differences were observed. On average the mean absolute difference of the OSI in the stenosis region was 0.03, and in the distal region this was 0.05.
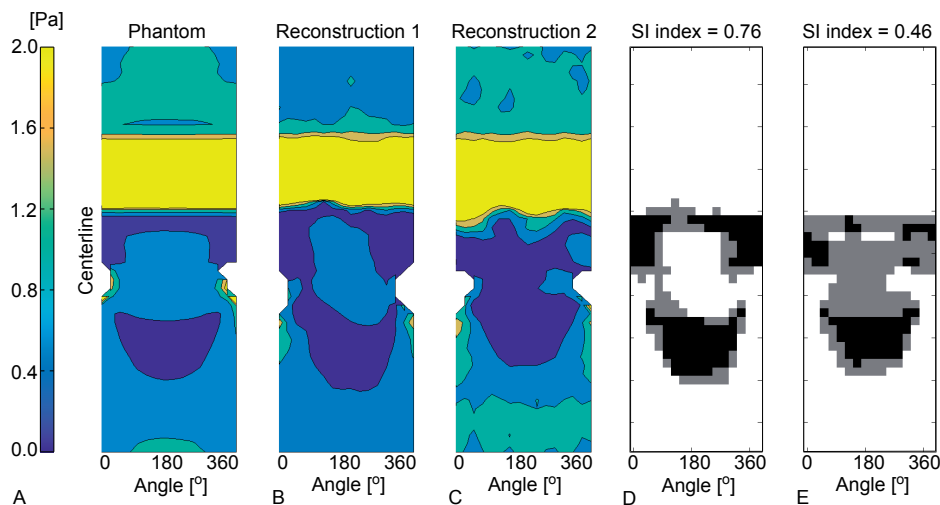
Fig. 5: Analysis of SI of WSS in phantom 1 and the corresponding reconstructions. A: Contour plot of the WSS. Similar as Fig.4 a low WSS region is located directly distal of the stenosis and distal of the side branch. B: Contour plot of the WSS in the reconstruction based on the segmentation from reader 1. C: Contour plot in reconstruction 2. D: Plot of the SI between the phantom and reconstruction 1. The white indicates WSS above 0.5 Pa in both the phantom and the reconstruction. Gray indicates low WSS in either the phantom or the reconstruction. Black indicates low WSS in both the phantom and the reconstruction. E: SI between the phantom and reconstruction 2.

	Similarity index	
	Reader 1	Reader 2
Phantom 1	0,76	0,46
Phantom 2	0,40	0,36
Phantom 3	0,75	0,37
Phantom 4	0,03	0,52

Table 2: SI of the areas of the phantoms and the reconstructions exposed to low WSS.
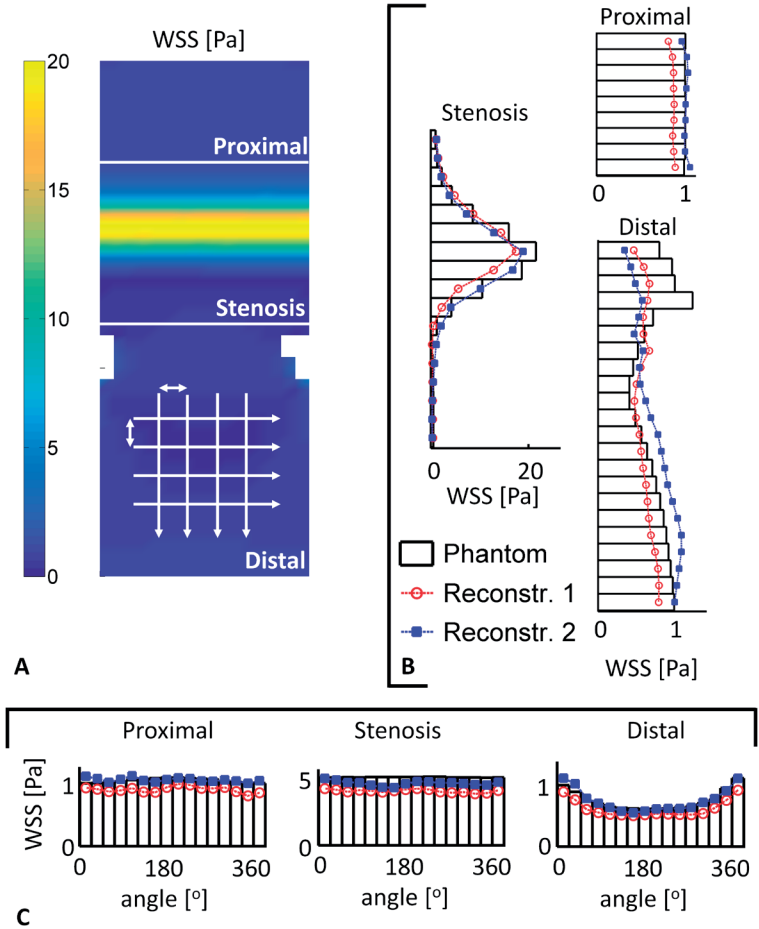
Fig 6: Quantitative analysis of the WSS in phantom 1. The white lines mark the three regions. **A:** 2D WSS map of phantom 1.The arrows indicate the direction of the averaging procedure. **B:** The circumferential means in the three regions. The bars indicate the mean circumferential WSS in the phantom and the lines the WSS from reconstruction 1 (red circle) and reconstruction 2 (blue square). In the proximal and stenosis region the WSS from the readers match the WSS in the phantom. In the distal region more pronounced differences are observed, primarily directly after the stenosis. **C:** Axial means in the three regions. In all regions the WSS from the readers match the WSS in the phantom.
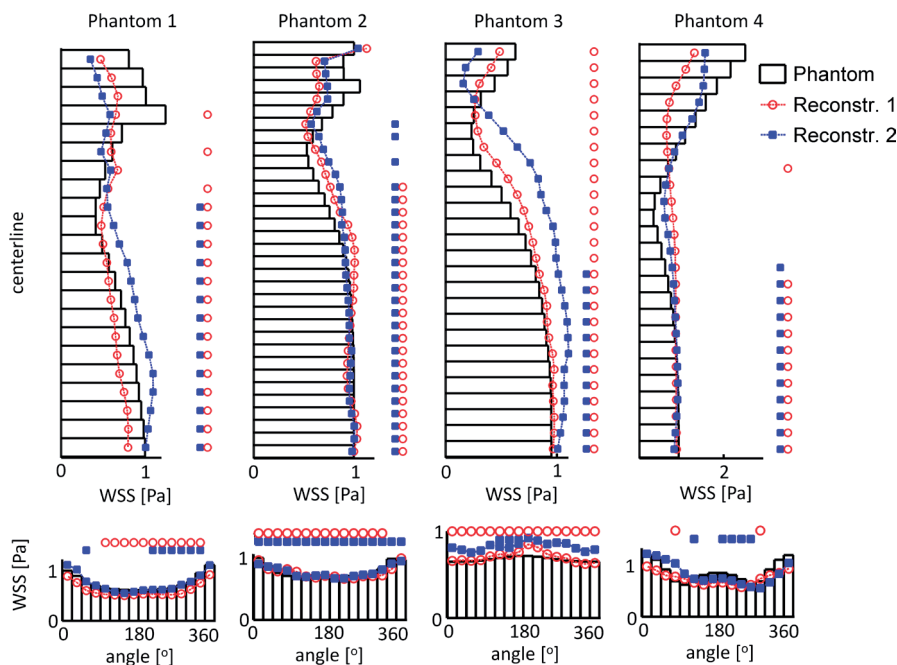
Fig 7: Circumferential and axial mean WSS in the four phantoms and reconstructions 1 and 2. The asterisks indicate the locations where the WSS in the phantom and the readers did not reach clinical equivalence. Particularly in the region directly distal of the stenosis the WSS is not clinically equivalent. Far distal the circumferential means are clinically equivalent. The axial means in the readers are similar as the phantom, though equivalence in not reached everywhere.

Averaging and equivalence test

Fig. 6 shows the axial and circumferential means of phantom 1. The axial means in all regions of the reconstructions matched those computed in the phantom, especially

Circumferential	Percentage of equivalence		
	proximal	stenosis	distal
Steady	100	18	66
TAWSS	100	20	58
OSI	100	81	49

Axial	Percentage of equivalence		
	proximal	stenosis	distal
Steady	99	0	58
TAWSS	100	0	53
OSI	100	64	45

Table 3: Overview of the average percentage of area where equivalence was observed in the four phantoms for the WSS, TAWSS and OSI.

immediately distal of the stenosis. The circumferential means in the proximal and stenosis region agreed nicely, although it was consistently lower in reconstruction 1. In the distal region the differences between the reconstructions and the phantom became more pronounced. This was consistent in all four phantoms (Fig. 7). The symbols in Fig. 7 indicate where the results were equivalent. Particularly immediately downstream of the stenoses the computed WSS were not equivalent.

In Table 3 the average percentage of equivalence per region is reported of all four phantoms. In the proximal regions the means in both directions were clinically equivalent. In the stenosis region, where the WSS were much higher, only the circumferential means shows some overlap in the order of approximately 30%. In the distal region the percentage of equivalence ranges from 40% to 80%. For the TAWSS, the percentage of equivalence in the regions was similar as reported for the WSS. The OSI in the proximal regions was 0 in all cases and therefore tested equivalent. The circumferential means in the stenosis region had more than 80% equivalence in six cases. In the distal region the equivalence typically ranged from 40% to 80% in both directions.

Wall shear stress vs. time-averaged wall shear stress

The middle row of Fig. 4 shows that qualitatively the TAWSS was similar to the WSS, although the low WSS in the distal region was more spread out. The equivalence test on the results from the phantom computations revealed that the proximal region was entirely equivalent (Table 4). The circular means in the stenosis region were equivalent in 70% of that region. In the distal region the equivalence in both circular and axial direction ranged from 50% to 80%.

Circ	proximal	stenosis	distal
1	100	71	68
2	100	73	70
3	100	67	77
4	100	74	56
Axial	proximal	stenosis	distal
1	100	0	50
2	100	0	81
3	100	0	63
4	100	0	63

Table 4: Percentage of equivalence between the WSS and TAWSS in the two original phantoms.

DISCUSSION

This study investigated the influence of angiography-based reconstructions on velocity and WSS computations in models of diseased coronary bifurcations. WSS computations in four phantom models served as the ground truth and were compared to the outcome of WSS computations in angiography-based reconstructions. Proximal to, and at the stenosis the WSS results quantitatively agreed nicely. Distal to the stenosis the same phenomena were observed, but subtle deviations in the reconstruction caused differences in jet characteristics and therefore the size and location of the low WSS regions. An equivalence test revealed that the results in the proximal part were statistically equal. However, directly distal of the stenosis significant variations were observed between the WSS in the phantoms and the reconstructions.

Velocity

Several studies focusing on the accuracy of the 3D reconstructions previously validated the CAAS 3D software. The most recent study reported an overall measurement error of approximately 0.02 mm for the lumen and 0.04 mm for the stenosis diameter[17], similar to the findings in this study. The previously reported Hausdorff distances between ground truth and reconstructed scaled up coronary artery geometries are also comparable[27]. Although the segmentation errors were small, they directly influenced the velocity patterns. Deviations in the reconstruction of the stenosis were immediately reflected in the peak velocity of the jet. The peak velocity in turn influenced the size and shape of the recirculation zone. The segmentation errors downstream of the stenosis mainly influenced the orientation of the jet.

   The reason that this jet could be influenced by the small reconstruction errors is related to design of the phantom. The planar phantom models with concentric stenoses were designed to investigate the precision of the image reconstruction techniques with regard to length and stenosis degree. However, this design resulted in symmetry of the flow, what could easily be disturbed by small deviations in the reconstructions. Curvature and eccentricity of stenoses on the other hand, can both cause helical flow patterns[20,39,40]. It was hypothesized that helical flows induces more stability[41–43]. So the computations in this study could be regarded as more challenging and provided a more rigorous test than curved models with eccentric stenoses might have been. For clinical purposes it would be interesting next step investigate this type of models.

Wall shear stress

The WSS in the two reconstructions were similar to the WSS in the phantoms. In the proximal and far distal regions the WSS agreed particularly well, and the WSS values were equivalent. From these results it follows that WSS can accurately be computed with

angiography-based 3D reconstructions in coronary arteries suffering from early stage atherosclerosis. The accurate prediction of absolute high and low WSS regions at and distal of the –admittedly challenging- symmetric stenoses proved to be more difficult. At the neck of the stenosis the maximal WSS differed between the phantom and the re-constructions. In these high WSS regions, reconstruction errors significantly influenced the absolute values, making studies focusing on absolute WSS for rupture risk prediction based on angiography alone difficult[35]. The regions directly distal of the stenoses were all exposed to low WSS, but the size of those regions varied. This was reflected in the results from the similarity index and the equivalence test. In the presence of a more advanced stenosis, angiography-based reconstruction might not suffice in providing the required precision to assess low WSS immediately distal of a –concentric- stenosis. An accurate WSS assessment in this region is important because of possible plaque progression[35]. To obtain the required reconstruction precision, intra-vascular imaging techniques, such as IVUS or OCT, can be used[12,15,44,45]. If angiography alone will be used, concentric stenoses must be regarded with caution. Furthermore, normalized WSS has proven to be a more robust parameter than absolute WSS[46], and might be a useful alternative to study the relationship between WSS and atherosclerosis in general.

Similar to previous reports[20,39,45], the results from steady-state and transient simulations matched qualitatively. With the noninferiority test this study demonstrated to what extent these results were statistical equivalent. In the proximal and far distal region they were equivalent, but mainly in the area directly distal of the stenosis the results differed. Thus, steady-state simulations might be valuable in mildly diseased coronary arteries, but the low WSS are not captured well in case of a lumen intruding plaques. Future stud-ies should be directed to find evidence that links WSS from steady-state computations to the natural history of atherosclerosis.

As stated by Peiffer et al., a point-to-point analysis of WSS in coronary arteries represents an ideal method for determining relationships between WSS and wall parameters[47]. Since WSS is a derived value from the velocity field at the wall it is highly sensitive to deviations in the reconstruction of the lumen. Even in the proximal region, where the WSS results matched to a high degree, a point-to-point comparison would still render statistically different. Numerous studies therefore employed other averaging techniques to analyze WSS. Goubergits et al. compared WSS in a phantom and an angiography-based reconstruction, and performed an analysis by construction normalized histo-grams[19]. This allowed for an elegant comparison of the global WSS distribution, but local information is lost. Other investigators used either axial or circumferential averaging[4,36]. While this is a form of data reduction as well, some local information is retained. Both averaging techniques were used in this study, and subsequently a test was introduced

to find statistical evidence for equivalence of the computed WSS. The combination of averaging techniques and testing for statistical equivalence could be a powerful tool in longitudinal studies that investigate the role of WSS in atherosclerotic disease progression.

Limitations

This study was limited at some points. First, in this study phantom models were used, while the final goal is an application in human coronary arteries. The main advantage of using phantoms is that the exact geometry was known allowing for a quantitative comparison of WSS patterns. Also by using these models motion artifacts were excluded. This allowed ruling out all effects other than reconstruction errors influencing WSS computations. However, in a clinical setting motion artifacts might play an important role, even when applying high frame rate imaging. For example, in diastole the velocity of a coronary artery can be in the order of 5 mm/s due to cardiac motion[48]. With a frame rate of 30 frames per second the resulting error can be in the same order as the imaging resolution. Future studies should focus on finding the influence of motion artifacts in angiography-based 3D reconstructions.

Next, in this study the phantoms were filled with contrast agent. In a clinical setting the imaging quality could be influenced by the mixing of the contrast agent with the blood. Similarly, the presence of bone and other tissue of the thorax that surround coronary arteries could influence the quality as well.

Finally, the outcome of the noninferiority test critically depends on the chosen margin of equivalence[37]. Our study demonstrated the added value of this technique, but also revealed the difficulty in setting the margins. Future studies should strive to reach a consensus on what margin can be regarded as clinically equivalent. Knowing that the precision of WSS computations cannot excel beyond the resolution limits of the used imaging modality, it seems compelling to take into account the sensitivity of the error due to the resolution limitation.

Conclusion

In conclusion, this study showed that WSS can accurately be computed within angiography-based 3D reconstructions of coronary arteries with early stage atherosclerosis. Fusion of angiography with intra-vascular techniques, such as IVUS or OCT, might be of added value for WSS computations in the presence of more advanced atherosclerosis.
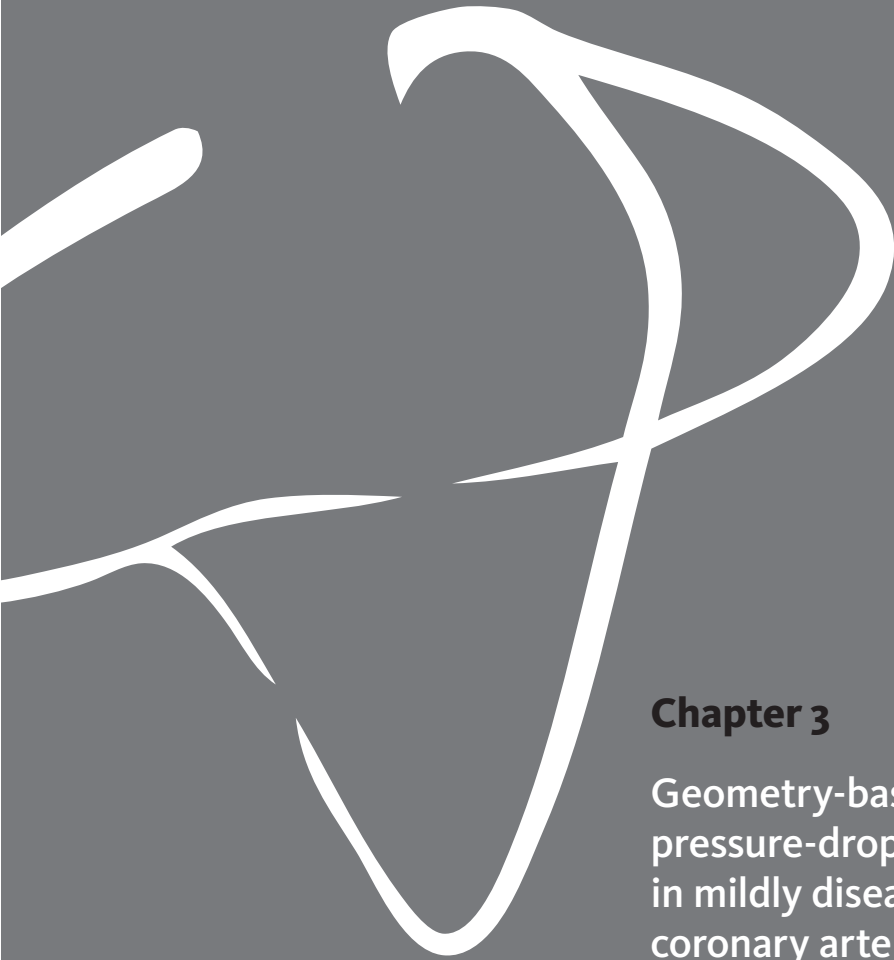
Chapter 3

Geometry-based pressure-drop prediction in mildly diseased human coronary arteries

ABSTRACT

Pressure drop (Δp) estimations in human coronary arteries have several important applications, including determination of appropriate boundary conditions for CFD and estimation of fractional flow reserve (FFR). In this study a Δp prediction was made based on geometrical features derived from patient specific imaging data. Twenty-two mildly diseased human coronary arteries were imaged with computed tomography and intravascular ultrasound. Each artery was modelled in three consecutive steps: from straight to tapered, to stenosed, to curved model. CFD was performed to compute the additional Δp in each model under steady flow for a wide range of Reynolds numbers. The correlations between the added geometrical complexity and additional Δp were used to compute a predicted Δp. This predicted Δp based on geometry was compared to CFD results. The mean Δp calculated with CFD was 855±666 Pa. Tapering and curvature added significantly to the total Δp, accounting for 31.4±19.0% and 18.0±10.9% respectively at Re=250. Using tapering angle, maximum area stenosis and angularity of the centerline, we were able to generate a good estimate for the predicted Δp with a low mean but high standard deviation: average error of 41.1±287.8 Pa at Re=250. Furthermore, the predicted Δp was used to accurately estimate FFR (r=0.93). The effect of the geometric features was determined and the pressure drop in mildly diseased human coronary arteries was predicted quickly based solely on geometry. This pressure drop estimation could serve as a boundary condition in CFD to model the impact of distal epicardial vessels.

INTRODUCTION

Atherosclerosis is a cardiovascular disease, characterized by plaque buildup in the vessel wall. A subset of atherosclerotic plaques, referred to as vulnerable plaques, contain a necrotic core, covered by a thin fibrous cap often infiltrated by inflammatory cells[1]. Rupture of the fibrous cap is the main cause of myocardial infarctions[2]. In previous studies we showed a close association between high wall shear stress (WSS) and plaque weakening in human coronary arteries[3,4]. Furthermore cap ruptures are often observed in the upstream region of the plaque where WSS presumably is high[5–7]. The combination of high WSS and a thin fibrous cap is therefore potentially a valuable parameter to identify the risk for coronary plaque rupture. WSS distribution in human coronary arteries can be obtained by combining 3D lumen reconstruction methods with computational fluid dynamics (CFD)[8–11]. Both lumen reconstruction and CFD are time consuming, especially if a large part of the coronary tree is included in the analysis. However, if WSS would serve as a risk stratification tool to be determined during an intervention, it needs to be calculated rapidly. To reduce the computational time CFD can be restricted to a 3D region of interest, e.g. a coronary bifurcation containing an atherosclerotic plaque. Appropriate boundary conditions should be defined to replace the proximal and distal regions. In steady flow simulations in a bifurcation region, the flow ratio over the side branches highly influences the WSS distribution and is determined by the pressure drop in the vessels distal to the bifurcation[12]. This pressure drop is composed of an epicardial part and a microvascular part. In this study we focus on the epicardial part. The goal of our study was to develop a pressure drop estimate based on geometry which can be used as a boundary condition to replace the proximal and distal regions in CFD. We chose to investigate mildly diseased vessels, because although they are left untreated, the regions around a plaque are often affected by atherosclerosis as well[13]. The lumen of the epicardial coronary tree can be imaged with biplane angiography and reliable 3D lumen reconstructions can be generated in real time[14,15]. This 3D lumen data can potentially serve to estimate the pressure drop in the epicardial vessels.

Real time image based pressure drop estimation in stenosed epicardial vessels can also be useful to determine the fractional flow reserve (FFR). FFR is an important indicator for the hemodynamic significance of a coronary stenosis[16]. It is defined as the pressure drop over the stenosis for minimal myocardial resistance. Treatment of the stenosis is warranted if the FFR is below 0.8[17]. During an intervention the FFR is measured with a pressure catheter. With an image based estimate of the pressure drop in a stenosed vessel it is also possible to calculate the FFR instead of measuring it.

Young and Tsai measured the pressure drop over idealized concentric and eccentric stenoses in a straight tube for a wide range of flow conditions[18,19]. They found a good relationship between the measured pressure drop and the Reynolds number, stenosis

length and severity. Gould et al. applied the relationship to compare the measured pressure drop in coronary arteries to the ones predicted from angiographic data with moderate success[20]. One of the reasons for this is that the relationship developed by Young and Tsai is based on idealized stenoses, while in vivo data show that lesions are much more complex.

This study sets out to find a new estimation of the pressure drop in human coronary arteries using imaging data. The method is based on stepwise adding a complexity to the geometry. The geometrical complexity is increased in three steps, where each additional geometrical feature leads to an increase in pressure drop. The added geometrical feature is subsequently correlated to the additional pressure drop it causes. The image based pressure drop was primarily investigated as a potential boundary condition in CFD, but is in this study it was also applied to predict FFR.

MATERIAL & METHODS

Patient selection

We investigated the coronary arteries of 33 patients from a subpopulation of the PROS-PECT trail (ClinicalTrails.gov identifier NCT00180466[21]). The patients were treated for an acute myocardial infarction or unstable angina. The coronary arteries were imaged with multi slice computed tomography (MSCT) and intravascular ultrasound (IVUS). Accurate 3D reconstructions of 54 mildly diseased arteries were generated based on a previously developed method[11]. Mildly diseased segments were selected because the aim of the study was to investigate regions proximal and distal to a plaque. These regions don't have a significant stenosis but are often affected as well and are considered mildly diseased[13]. To ensure a significant pressure drop, twenty-two segments were selected (9x LAD, 9x LCx, 4x RCA) with a maximum diameter stenosis of 4x 20-30%, 5x 30-40%, 10x 40-50%, 1x 50-60% and 2x 60-70%.

Coronary artery models

Four models of each artery were generated to investigate the effect of the geometrical features on the pressure drop. In each subsequent model a geometrical complexity was added and a feature describing this change in geometrical complexity was correlated to the change in pressure drop it caused (Fig 1, right panel). Firstly, a straight cylindrical model was created with the radius equal to the inlet radius of the 3D reconstruction. Secondly, a linearly tapered model was generated. The inlet radius, the outlet radius and the length were based on the full 3D reconstruction. Thirdly, in the stenosed model, the lumen contours obtained with IVUS replaced the lumen of the tapered model. Finally, a curved model was created by adding the centerline obtained with MSCT, which resulted

Models

Curved

Stenosed

Tapered

Straight
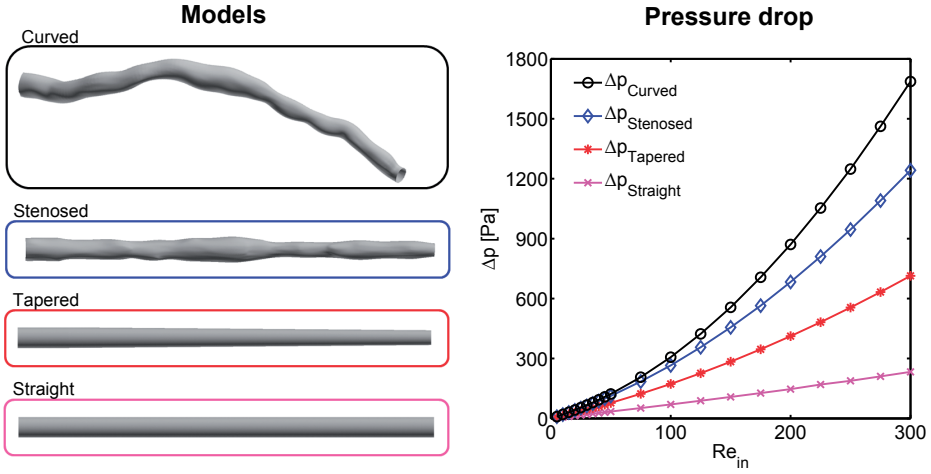
Pressure drop

Fig. 1: For each patient specific coronary artery four models with increasing complexity were generated, a straight, tapered, stenosed and curved model (left panel). In each model the pressure drop was calculated using CFD for Reynolds numbers ranging from 0 to 300 (right panel).

in the complete 3D reconstruction of the artery. The models were generated using in-house developed image processing techniques (Mevislab, Bremen, Germany).

CFD

The pressure drop in each model was calculated with CFD. A tetrahedral mesh with linear elements was generated for all geometries (Gambit, Ansys, anonsburg, U.S.). Mesh refine-ment studies resulted in an element size of 1.25·10−2 mm. The Navier-Stokes equations were solved using standard numerical techniques (FIDAP, Ansys, Canonsburg, U.S.). The pressure drop was calculated under steady flow conditions for inlet Reynolds numbers (Re) ranging from 5 to 300, with increments of 5 between 5 and 50 and increments of 25 above that. To mimic the coronary flow conditions we extended the inlet with five times the radius (VMTK, Orobix, Bergamo, Italy) and prescribed plug flow. The outlets were stress free. A typical result of the CFD can be seen in Fig. 1 (left panel), which shows the pressure drops at the different Re in the three geometrical models of an artery.

Modeling the pressure drop

Previous studies already analyzed the typical shape seen in the results of Fig. 1[18]. At low flow (Re <40), the pressure loss is a linear function of the average velocity (linear domain). At higher flow, the pressure drop is also influenced by convective losses, causing a non-linear pressure drop (non-linear domain). Previous studies found that the pressure drop can be described by a second order polynomial:

$$\Delta p = \gamma v + \varepsilon v^2 \tag{3.1}$$

Here γ and ε are geometry dependent parameters related to the linear and non-linear domain and v the mean velocity at the inlet. If a correlation can be found between these parameters and geometry, the pressure drop in a vessel can be calculated based on geometry.

In addition to Eq. 3.1, an expression for the pressure drop in the linear domain for a tapered vessel can be derived. Similarly to the Poiseuille-Hagen derivation, we assumed that the flow is fully developed and axisymmetric, but now with the boundary conditions:

$$v_z = 0 \text{ at } r = \frac{r_0 - r_i}{L} + r_i \tag{3.2}$$

$$\frac{\partial v_z}{\partial r} = 0 \text{ at } r = 0 \tag{3.3}$$

Where r_i is the inlet radius and r_o the outlet radius. This leads to:

$$\Delta p_{tap,0} = \frac{8\mu L}{3} \left[\frac{r_0^{-3} - r_i^{-3}}{r_0 - r_i}\right] r_i^2 v \tag{3.4}$$

For the derivation it was assumed that there were no radial velocity components. Although the assumptions that lead to the expression are not entirely valid in the tapered model, Eq. 3.5 was used as a first estimate for the pressure drop in the tapered model in the linear domain. The expression was fitted to the CFD result in the linear domain with an additional parameter γ$_{tap}$. The pressure drop in the non-linear domain in the tapered model was found by fitting ε$_{tap}$. This gives the expression for the total pressure drop in the tapered model, without having to calculate the pressure drop in a straight tube first:

$$\Delta p_{tap} = \gamma_{tap} \cdot \Delta p_{tap,0} + \varepsilon_{tap} v^2 \tag{3.5}$$

$$= \gamma_{tap} \cdot \frac{8\mu L}{3} \left[\frac{r_0^{-3} - r_i^{-3}}{r_0 - r_i}\right] r_i^2 v \tag{3.6}$$

Subsequently, we set out to find an expression for the additional pressure drop in the stenosed model. The pressure difference between a tapered and stenosed model was fitted providing the fitting parameters γ$_{tap\grave{a}sten}$ and ε$_{tap\grave{a}sten}$ in:

$$\Delta p_{tap \rightarrow sten} = \Delta p_{sten} - \Delta p_{tap} \tag{3.7}$$

$$= \gamma_{tap \rightarrow sten} \cdot v + \varepsilon_{tap \rightarrow sten} \cdot v^2 \tag{3.8}$$

The same approach was followed to fit the pressure between the stenosed and curved model, resulting in an expression for $\Delta p_{sten\rightarrow curv}$. Together this lead to the expression for the total pressure drop which was used to fit Δp for all 22 vessels:

$$\Delta p = \gamma_{tap} \cdot \Delta p_{tap,0} + \varepsilon_{tap} v^2$$

$$+\gamma_{tap\rightarrow sten} \cdot v + \varepsilon_{tap\rightarrow sten} \cdot v^2$$

$$+\gamma_{sten\rightarrow curv} \cdot v + \varepsilon_{sten\rightarrow curv} \cdot v^2$$

(3.9)

Geometric parameters

The next step involved correlating the fitting parameters to the geometrical features of the models. In the tapered model, the only relevant geometrical parameter was the tapering angle, depicted in Fig. 2a with tan(α). The stenosed geometry was quantified by three geometrical parameters. If an arterial segment contains a focal stenosis, this might potentially dominates the total pressure drop. We therefore included area stenosis (AS=max((A_{tap}-A_{sten})/A_{sten}). In a more diffusely diseased segment, the gradual changes of the lumen might be a better predictor for the pressure drop. An integral measure of this gradual luminal change can be obtained by computing V_{diff} (V_{diff} =V_{sten}-V_{tap}, gray area in Fig. 2b). Finally, we included V_{ratio} to define a geometrical parameter independent of volume of the tapered model (V_{ratio}=V_{tap}/V_{sten}).

The curved model was quantified by two parameters. We used tortuosity of the centerline, defined as the ratio of the absolute length between the start and end point of the centerline and the whole length of the centerline. Bijari et al. used this parameter to study the influence of geometry on flow disturbances in carotid bifurcations[22]. Secondly, we quantified the curvature by summing the angles between the points along the discretized centerline normalized by the step size: $\Sigma\varphi/\Delta s$ (Fig. 2c). This parameter attributes more weight to the local curvature of vessel.

The Pearson r test was used to check for linear regression between the pressure drops and the geometrical features. It is conceivable that combinations of geometrical features influence the resulting pressure drop. Therefore we also correlated cross terms of the quantified geometrical features of subsequent modeling steps to the pressure drops. The FFR is defined as the ratio between the distal pressure Pd and the aortic pressure Pa under hyperemia. For hyperemic conditions, we used Re=250. Average aortic pressure was assumed to be 90 mmHg[23]. Distal pressure was obtained subtracting the pressure drop from aortic pressure. The pressure drop was derived from CFD to compute the ground truth (FFR_{CFD}) or from Eq 3.9 to determine $FFR_{estimation}$.
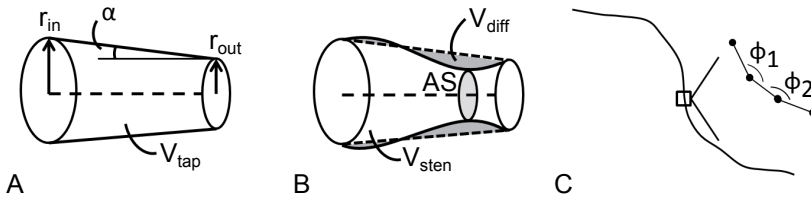
Fig. 2: The geometrical features that were quantified in the three models. **A:** The tapered model was quantified with tapering angle α and volume V_{tap}. Here r_i and r_o are the inlet and outlet radius. **B:** The stenosed model, where V_{diff} indicates the volume difference (V_{diff}) between the tapered model and the stenosed model (V_{sten}). The maximum degree of stenoses is indicated with AS. **C:** The centerline of the curved model was quantified with the angular change from the 3D centerline with the sum of angle of angle $Φ_i$.

RESULTS

The 3D pressure distribution for three different Re in three arteries is presented in Fig. 3. The coronary arteries in this study included a representative set of mildly diseased segments, with varying length, tapering, degree of stenosis and curvature. As a consequence, a large variation in pressure drops computed with CFD was observed. In general, large pressure drops were observed after stenosis (Fig. 3, arrow A) and higher curvature (Fig. 3, arrow B). The pressure drop showed a non-linear increase as a function of the Re.

The mean pressure drop of the twenty-two coronaries at three representative Re is given in Table 1. The pressure drop shows a non-linear increase as a function of the Re: An increase in the Re of 150% leads to an increase in pressure drop of 300%. The high standard deviation indicates a large variety of pressures drops found for the twenty-two models. Comparatively high contributions from the straight and tapered model were found. The contributions from the tapered and stenosed models are hardly influenced by the Re, respectively varying between 31.4% and 32.3% and between 16.1% and 18.7%. With increasing Re, the relative contribution from the straight model decreases from 41.9% at to 31.9%, while the contribution due to curvature increases from 9.7% to 18.0%. At Re=250 the contribution of pressure drop in the tapered model is approximately equal to that of the straight tube and the contribution of the curved model is approximately equal to that of the stenosed model.

Results of the fitting and correlating procedures are given in Table 2. In the tapered model the angle was correlated to the pressure drop. For $γ_{tap}$ and $ε_{tap}$ a correlation with the tapering angle of r=0.99 and r=0.77 was found respectively. In the stenosed model we found that $γ_{tapàsten}$ had the highest correlation with V_{ratio} (r=0.85). For $ε_{tapàsten}$ the correlation was highest for AS (r=0.79). Due to the minimal pressure drop in the linear domain, no significant correlations were found for $γ_{stenàcurv}$. For $ε_{stenàcurv}$ we found the strongest correlation with the sum of the angles with r=0.59. Additionally, we found one
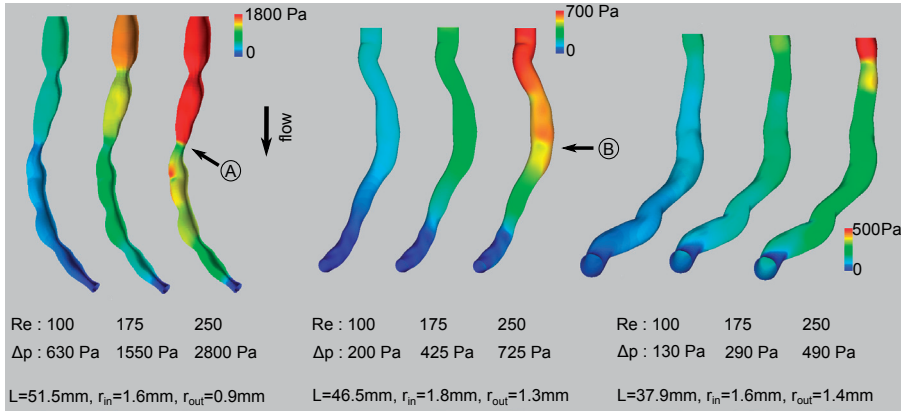
Fig. 3: Three examples of patient specific coronary reconstruction, where the color map represents the pressure drop from CFD. Each artery is depicted at Re= 100, 175 and 250. Large pressure drops mainly occur in stenosed areas (A) and near curves (B). Below the values are given for the pressure drops, length of the vessel and inlet and outlet radius. A large variation in pressure drop and geometry can be seen in the three examples. Note that the color bars were adjusted to optimize visualization of the pressure drop for all Reynolds numbers and the color bars do not cover the full range.

Re	$<P_{CFD}>$ [Pa (mmHg)]	straight [%]	tapered [%]	stenosed [%]	curved [%]
100	214±153 (1.6±1.1)	41.9±31.7	32.3±18.5	16.1±22.1	9.7±8.5
175	487±368 (3.7±2.8)	35.8±28.8	31.8±18.8	17.7±20.0	14.8±10.0
250	855±666 (6.4±5.0)	31.9±26.7	31.4±19.0	18.7±18.9	18.0±10.9

Table 1: On the left the mean total pressure drop at Reynolds number of 100, 175 and 250. The four columns on the right give the mean additional percentage an added geometrical feature had with respect to the total pressure drop.

r	tan α	AS	V_{diff}	V_{ratio}	Tortuosity	$\Sigma\varphi_i/\Delta s$	AS · tan α	Expression
γ_{tap}	**0.99**							7.76 (tan α) + 1
ε_{tap}	0.77							-
$\gamma_{tap\rightarrow sten}$		0.76	-0.77	**0.85**				18.82 (V_{ratio}) - 16.62
$\varepsilon_{tap\rightarrow sten}$		0.79	-0.37	0.50				-
$\gamma_{sten\rightarrow curv}$					-	-		-
$\varepsilon_{sten\rightarrow curv}$					-0.21	**0.59**		2.48·10⁻⁶ ($\Sigma\varphi_i/\Delta s$) - 0.19
ε_{sten}							**0.89**	34.95 (AS · tan α) + 0.13

Table 2: Overview of correlation between pressure drops and quantified geometrical complexities. The numbers in bold were used in the prediction. The last column shows the found relations between the fitting factors and the geometrical feature.

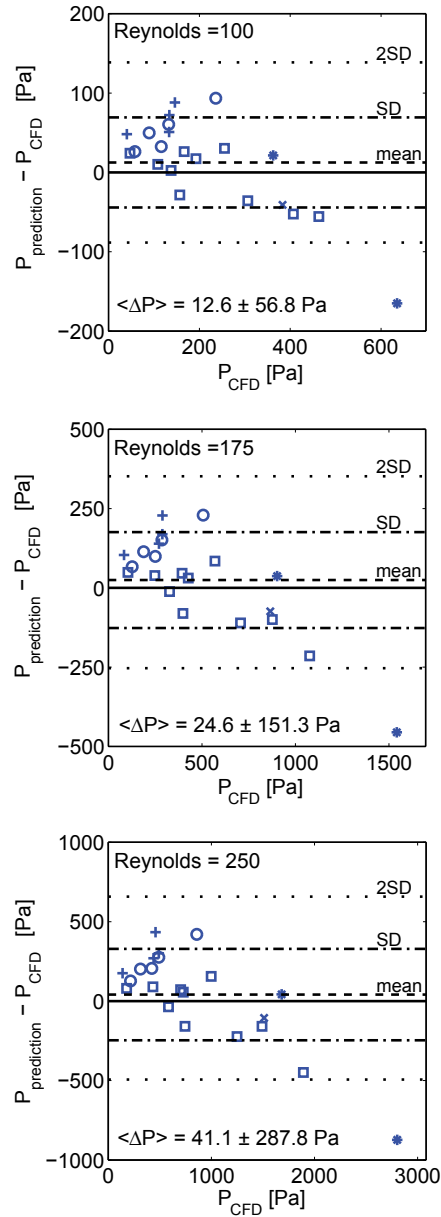**Fig. 4**: Difference between the pressure found with CFD and the predicted pressure at Reynolds is 100, 175 and 250. The mean difference at all Reynolds is small and most pressure drop predictions fall within the range of 1 SD of the computed pressure drop. The different symbols indicate the maximum degree of stenosis: + is 20-30%, o is 30-40%, □ 40-50%, × is 50-60% and * is 60-70%.

cross terms of two geometrical parameters that had a higher r-value than the separate parameters combined. The product of the tapering angle and AS correlated with ε_{sten} with r=0.89. This ε_{sten} can thus replace ε_{tap} plus $\varepsilon_{tap\grave{a}sten}$ in Eq. 3.9. All the above stated correlations were significant with the Pearson r test for p<0.05. The functions describing the best correlation between the fitting parameters and geometrical features are given in Table 2.

   The results from the pressure drop estimation, based on geometry, were compared to the pressure drop found by CFD. The difference between computed and estimated pressure drop as a function of the computed pressure drop is given in Fig. 4 and Table 3. The mean difference in pressure drop is relatively low for all Reynolds numbers, never exceeding 5.4%. However, per vessel considerable relative deviations were observed. At Re=100, 90% of the predictions had a relative deviation between −26.0% and 55.7%. At Re=175 this was between −29.5% and 60.6% and at Re=250 between −31.1% and 64.8%. The symbols in Fig. 4 indicate the maximum degree of stenosis. The symbols are not grouped according to the pressure drop obtained with CFD. This means that the pressure drop is not solely determined by the degree of stenosis but is also by other features, such as tapering and curvature.

Re	$<p_{CFD}>$ [Pa]	$<\Delta p = p_{pred} - p_{CFD}>$ [Pa]
100	214±153	12.6±56.8
175	487±368	24.6±151.3
250	855±666	41.1±287.8

Table 3: Mean pressure drop from CFD and the mean difference between the pressure drop from CFD and from the prediction:
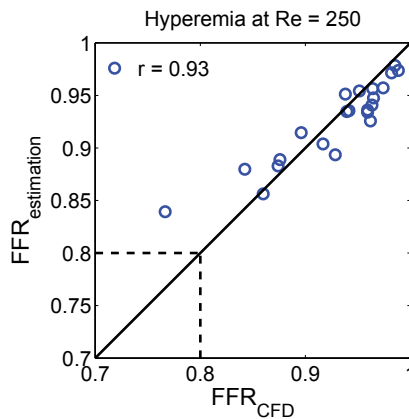
$\Delta p = p_{pred} - p_{cfd}$

Fig. 5: The correlation between the FFR obtained from CFD and the FFR obtained from our predictions at Re=250.

The FFR was estimated based on the pressure drop prediction for each vessel. FFR$_{estimation}$ showed a high correlation with FFR$_{CFD}$ at hyperemia (r=0.93, Fig 5) and at lower Reynolds numbers (r=0.95 at Re=100, and r=0.93 at Re=175). The values for r indicate that the quality of the prediction is independent of the assumed hyperemic flow.

DISCUSSION

We used patient-specific geometries to estimate the pressure drop in 22 mildly diseased human coronary arteries. We showed how different geometrical features contribute to the total pressure drop in human coronary arteries. This allowed us to find the correlation between the additional pressure drops and geometric features. This lead to an expression that can predict the pressure drop in coronaries based on its geometry.

The 3D patient specific coronary models were deconstructed into four models with increasing complexity. This enabled us to quantify the relative contribution to the total pressure drop for each model separately. When compared to the straight model all other models showed a higher contribution with increasing Re. This can be expected since increased Re cause changes in velocity profiles that generally contain more dissipation and therefore increase the pressure drop in a non-linear fashion. The fact that the relative increase for the tapered and the stenosed model is approximately equal and somewhat lower for the curved model is fully determined by the 3D shape and the degree of stenosis and therefore specific for the data set used in this study. At Re=250, the contribution of the tapered model is approximately equal to the straight model and that of curved model approximately equal to the stenosed model. This implies that the tapering and 3D curvature, ignored in many previous studies[18,19,24–26], should be included when estimating the pressure drop in human coronaries.

Our results show that the additional pressure drop in the tapered model can be estimated very accurately in the linear regime based on Eq. 3.5 and adequately in the non-linear regime. The resulting difference between the computed and estimated pressure drop was only 4.3±15.9 Pa at Re=100 and -0.4±111.8 Pa at Re=250, indicating that the effect of tapering on the pressure drop can be accounted for. This result was expected since in this regime the Poiseuille flow approximation is also expected to hold. 3D curvature inherently induces more complex disturbances in the velocity field and it is therefore not surprising that the effect was not captured that adequately with a single geometrical feature.

For the stenosed model we found that the relative pressure drop was mainly influenced by AS, a finding that is in agreement with the findings from Young and Tsai. They calculated the pressure drop based on Eq. 3.1, with γ and ε determined by K_v, K_t and a measure

for the lumen narrowing. Gould et al. applied this equation to angiographic images to predict the pressure drop with moderate success in human coronary arteries with a high degree of stenosis[20]. However, due to the high degree of stenosis, different flow regimes occur in these vessels compared to the mildly diseased regions we investigated. They observed a difference between the measured and predicted pressure drop on a vessel to vessel basis of 2,500 Pa. Not only were the stenoses not idealized in this study, the aforementioned effects of tapering and 3D curvature were not included either. Despite that our pressure drop prediction shows deviations on a vessel to vessel basis, we did incorporate key geometrical features that determine the pressure drop into the model. This leads us to belief that our model is more suitable for quick pressure drop predictions in mildly diseased regions than predictions based on the models originating from Young & Tsai, since these models were developed for high degrees of stenoses.

The pressure drop prediction in Fig. 4 presents a downward trend. This might be caused by the few cases that present a higher degree of stenosis. As discussed above, regions with a higher degree of stenosis probably present different flow regimes. The model was fitted on mainly mildly diseased cases. The downward trend shows that the model was not able to capture the effects that occur in both the mildly and more heavily diseased regions. A possible solution to capture the effects of the different flow regimes is to use samples from the entire range of stenosis degrees. The model can then be fitted on multiple ranges of stenosis degree.

A high correlation was found between FFR_{CFD} and $FFR_{estimation}$. Despite the observed discrepancy between computed and estimated pressure drop the relatively high arterial pressure leads to a very good FFR prediction.

Another study developed a model to predict FFR with CFD in a reconstruction of the entire coronary tree based on CT data[27]. This model was applied on large patient populations and the computed FFR was compared to the in vivo measured FFR which served as the gold standard. Moderate to good correlations were found in these studies for a wide range of FFR; r=0.72 and r=0.63 [28,29].Whether or not a simpler and faster approach to estimate FFR on imaging data alone can also give valuable results, depends on how well the pressure drop predictions perform in more stenosed segments with lower FFR values. In future studies the clinical relevance of the current findings should be assessed by including more heavily diseased coronary arteries, as well as comparing the predicted FFR to in vivo measurements.

There are several limitations to this study. We selected geometrical features that can be obtained with standard imaging techniques and were thought to cause pressure losses. The possibility that other features, not included in this study, can also be indicative for pressure losses cannot be ruled out. One way to possibly overcome this limitation is to derive a pressure drop estimation from the Navier-Stokes equations. Our good results

of the derivation in the tapered geometry illustrate the potential of this approach and could be explored for the stenosed and curved geometries.

The same data set was used to first fit the model and subsequently analyze the predicting quality of that model. This approach leads to a minimal average error. In future studies a larger data set would allow the separation of the training and testing procedure leading to a more thorough analysis of the model.

In the reconstructions of the segments, side branches were not included, but this should have no effect on the comparison between CFD result and the prediction. However, when compared to in vivo measurements the effect of tapering can be overestimated.

This method might be used to determine outflow boundary conditions in CFD. However, the approach in this study is only suited for the vessels visible on imaging data. This implies that this pressure drop prediction cannot be applied on vessels of the microvasculature which is important as well. An estimate for pressure drop in the microvasculature needs to be included as well. Other models can be used for this, although many questions remain about diseased distal beds[8,30–32].

Previous studies used time-averaged WSS to investigate the relation between disease progression and WSS[10,21,33]. Results from previous studies suggest that cycle averaged WSS patterns are in good agreement with steady flow patterns[34–36]. Steady flow simulations can thus provide relevant WSS data and are much quicker to perform than transient simulations. Additionally, FFR is calculated as a moving average from pressure data. Therefore this study focused on steady flow. Following from the choice of steady flow simulations, using rigid walls doesn't influence the outcome in here. Elastic walls only play a role in transient situations where they induce a windkessel effect. In steady simulations this effect cannot occur and therefore the walls can be assumed rigid.

In this study we derived an expression for the pressure drop in mildly diseased coronary arteries based solely on imaging data. On average the predicted pressure drop shows good agreement with the computed pressure drop. The image based pressure drop estimation can be used for quick determination of boundary conditions, paving the way to assess WSS in a clinical setting.
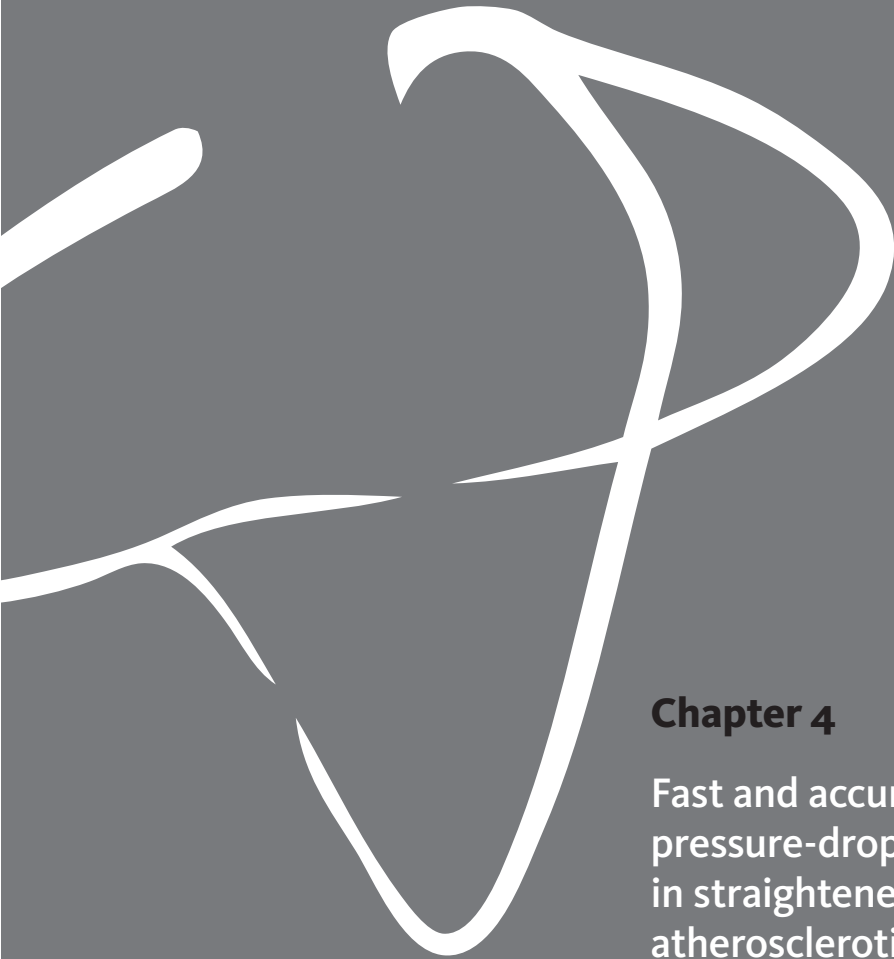
Chapter 4

Fast and accurate pressure-drop prediction in straightened atherosclerotic coronary arteries

ABSTRACT

Atherosclerotic disease progression in coronary arteries is influenced by wall shear stress. To compute patient-specific wall shear stress, computational fluid dynamics (CFD) is required. In this study we propose a method for computing the pressure-drop in regions proximal and distal to a plaque, which can serve as a boundary condition in CFD. As a first step towards exploring the proposed method we investigated ten straightened coronary arteries. First, the flow fields were calculated with CFD and velocity profiles were fitted on the results. Second, the Navier-Stokes equation was simplified and solved with the found velocity profiles to obtain a pressure-drop estimate ($\Delta p_{(1)}$). Next, $\Delta p_{(1)}$ was compared to the pressure-drop from CFD (Δp_{CFD}) as a validation step. Finally, the velocity profiles, and thus the pressure-drop were predicted based on geometry and flow, resulting in Δp_{geom}. We found that $\Delta p_{(1)}$ adequately estimated Δp_{CFD} with velocity profiles that have one free parameter β. This β was successfully related to geometry and flow, resulting in an excellent agreement between Δp_{CFD} and Δp_{geom}: 3.9±4.9% difference at Re=150. We showed that this method can quickly and accurately predict pressure-drop on the basis of geometry and flow in straightened coronary arteries that are mildly diseased.

INTRODUCTION

Ruptures of atherosclerotic plaques in coronary arteries are viewed as the main cause of acute coronary syndrome[1]. Whether a plaque is rupture-prone is largely governed by its composition[2,3]. As increasing evidence shows, plaque composition and rupture location are influenced by wall shear stress (WSS)[4–6]. If the WSS over plaques in individual patients could be quantified, it might prove useful in steering treatment, especially in combination with other plaque specific markers for vulnerability, e.g. cap-thickness.

While WSS in coronary arteries cannot directly be measured *in vivo,* it can be examined with computational fluid dynamics (CFD), which numerically solves the Navier-Stokes (NS) equation. With an accurate reconstruction of the geometry of the coronary artery and appropriate boundary conditions, CFD can compute the entire flow field (e.g. Kim et al. 2010). But while software packages can obtain the 3D geometry of the coronary arteries directly[8,9], CFD remains time consuming with conventional technology. To use WSS for decision support during an intervention, CFD must be performed within a limited time frame.

One approach to reducing computational time is to only compute flow dynamics with CFD in the stenosed region, and use reduced-order models for epicardial arteries proximal and distal to the stenosed region[10–12]. This approach is illustrated in . A 3D reconstruction suited for CFD computations is created based on multi-planar angiography of the stenosed region. The dotted lines represent the epicardial vessels for which reduced-order models based on imaging data could be used (Right panel). At the proximal end of the scheme the proximal pressure (p_{prox}) is imposed that is routinely available during catheterization, and at the distal end a lumped-parameter model is used for the the myocardium (Right panel).

This study focused on finding a reduced-order model based on the geometry of the epicardial arteries for pressure-drop estimation. Past studies presented methods to predict pressure-drop solely on the basis of geometry. In a landmark study, Tsai & Young derived an expression for the pressure-drop over an idealized stenosis as a function of velocity and geometry[13,14]. This work was later used to estimate the pressure-drop in stenosed human coronary arteries[15]. Previous work from our group extended those models to incorporate more patient-specific geometrical features[16]. On average these models performed well, but large deviations can occur per individual vessel.

In this study we propose a method for computing the flow dynamics in regions proximal and distal to a plaque, which can serve as a boundary condition in CFD. The NS equation was simplified and solved with assumed velocity profiles based on the geometry. With this approach we investigated whether the pressure-drop can quickly and accurately be estimated on the basis of geometry and flow.

MATERIALS & METHODS

As a first step towards exploring the proposed method we investigated straightened coronary arteries, as straightening reduces the complexity of the flow field. First, the flow fields were computed with CFD and on the results two functions for the velocity profiles were fitted: $v_z^{(1)}$ with one free parameter and $v_z^{(3)}$ with three free parameters. Second, the NS equation was simplified and solved with the fitted velocity profiles to obtain the pressure-drop. Third, the resulting pressure-drop estimate was compared with the pressure-drop from CFD as a validation step. Finally, it was found how to predict the velocity profile $v_z^{(1)}$, and thus the pressure-drop, on the basis of geometry and flow.

Case selection

In the Prospect trial the three main coronary arteries from patients with acute coronary syndrome were imaged with multi-slice computed tomography and intravascular ultrasound (IVUS)[17]. From this study we took the IVUS data of the coronary arteries that did not contain the plaque that had caused the myocardial event. These segments were all affected by atherosclerosis and considered to be mildly diseased. They therefore represent segments proximal and distal to a plaque, since they are often mildly diseased as well[18]. We used three left anterior descending, five left circumflex and two right coronary arteries with excellent image quality and with the maximal area stenosis within a representative range. The average diameter was 2.8±0.5 mm and the average length 44.1±10.5 mm. The maximal area stenoses in the segments were; 1x 20-30%, 6x 40-50%, 1x 50-60% and 2x 60-70%. All patients gave written informed consent.

Geometrical reconstruction & CFD

In the IVUS images the lumen was segmented[19]. The centers of the lumen contours were aligned and the distance between the contours was obtained from the IVUS data. From the lumen contours a surface was created (Mevis lab, Bremen, Germany), resulting in the reconstructions of straightened coronary arteries (Fig 2 top). The side branches were not taken into account in this study. An inlet of five times the inlet radius was added to the reconstruction (VMTK, www.vmtk.org)[16].

The geometries were meshed with GAMBIT (ANSYS, Inc., Canonsburg, PA, USA). Mesh independency studies were conducted, resulting in a surface mesh of triangular elements with an element size of 1.25×10^{-2} mm and a volume mesh with approximately $1 \cdot 10^{6}$ tetrahedral elements. CFD was performed with FIDAP (ANSYS, Inc., Canonsburg, PA, USA) and steady flow was simulated. At the inlet a plug flow was prescribed. The inlet flow was defined on the basis of the Reynolds number (Re), which ranged from 25 to 250 with steps of 25. The outflow conditions were defined as stress free. The blood was modeled as a Newtonian fluid with a density of $1.0 \cdot 10^{3}$ kg/m^{3} and a viscosity of $4.0 \cdot 10^{-3}$ Pa·s.
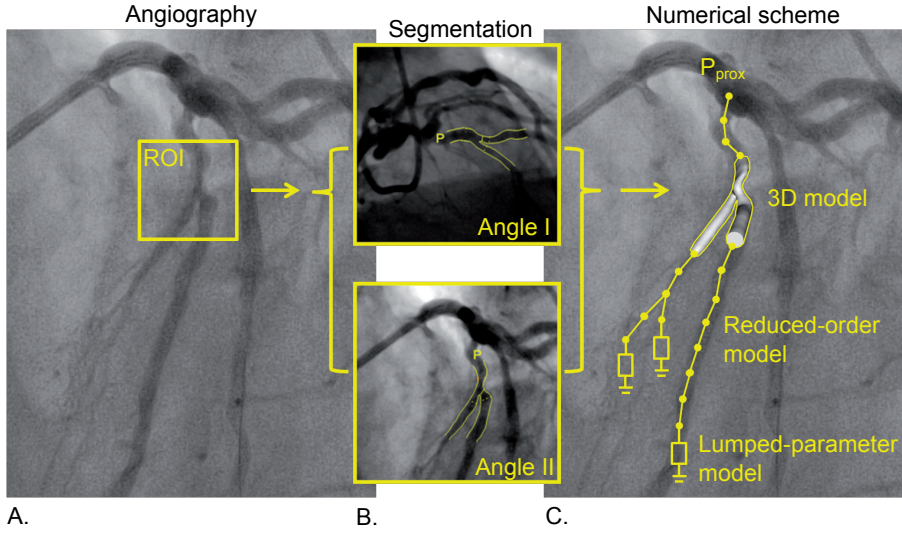
Fig. 1: Pipeline for online WSS computations. **Left panel:** Angiography image of coronary artery with stenosed segment, i.e. the region of interest (ROI). **Middle panels:** Two angiography images of the stenosed region at different angels. Based on these two images a 3D reconstruction suited for CFD computations can be made. **Right panel:** Illustration of the scheme is superimposed on the angiography image. WSS can be computed with CFD in the 3D model. The dotted lines represent the epicardial vessels for which reduced-order models based on imaging data could be used. The scheme is closed off proximally with pressure p_{prox}, and distally with a lumped-parameter model for the myocardium.

Navier-Stokes equation

Flow dynamics is described by the combination of the NS equation and the continuity equation. The NS equation is defined as:

$$\rho \left(\frac{\partial \vec{v}}{\partial t} + \vec{v} \cdot \nabla \vec{v} \right) = -\nabla p + \mu \nabla^2 \vec{v} \tag{4.1}$$

In this study we investigated how the NS equation could be simplified to a form in which it can be solved quickly and still provides a good approximation of the pressure-drop. As the pressure-drop was assumed to be predominately in the axial direction, the radial pressure-drop was assumed to be zero and only the axial component of the NS equation had to be solved. Together with assumed axisymmetry and steady flow, the NS equation simplifies to:

$$\rho \left(v_r \frac{\partial v_z}{\partial r} + v_z \frac{\partial v_z}{\partial z} \right) = -\frac{\partial p}{\partial z} + \mu \left(\frac{1}{r} \frac{\partial}{\partial r} \left(r \frac{\partial v_z}{\partial r} \right) + \frac{\partial^2 v_z}{\partial z^2} \right) \tag{4.2}$$

If a form of v_z can be assumed that adequately describes the velocity profiles, Eq.4.2 can quickly be solved for the axial pressure-drop.
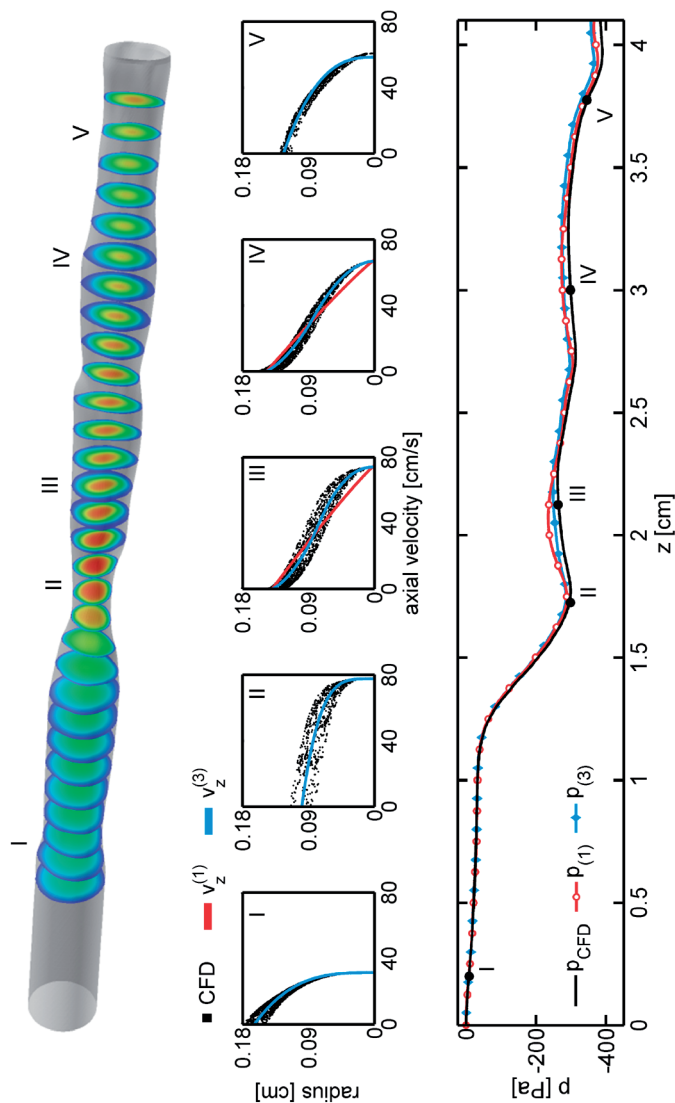
Fig. 2, Top: A straightened coronary artery based on IVUS data. The iso-planes show the velocity magnitude calculated by CFD. The roman numerals indicate five regions of interest. **Middle row:** Each panel shows the velocity data from CFD (black dots), with on the horizontal axis the axial velocity and on the vertical axis the distance to center of the lumen. The spread in the velocity data in radial direction is due to the patient-specific lumen which is not circular. In the panels three typical profiles are shown; a parabolic profile in I and V; a plug profile in II; and a sigmoid-shaped profile in II and IV. On the CFD data two functions with different complexity were fitted; $v_z^{(1)}$ (blue) with one free parameter and $v_z^{(3)}$ (red) with three free parameters. Both $v_z^{(1)}$ and $v_z^{(3)}$ captured the parabolic and plug profiles. Only $v_z^{(3)}$ was able to capture the sigmoid-shaped profiles. **Bottom:** The pressure-drop as a function axial coordinate. The pressure-drop from CFD (black line) was regarded as the gold standard. The pressure-drop Δp_1 was computed with the fits from $v_z^{(3)}$, and Δp_3 with the fits from $v_z^{(3)}$.
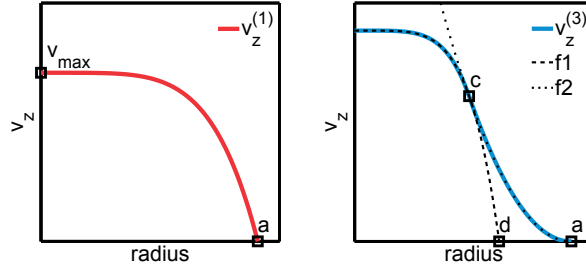
Fig. 3: The two functions $v_z^{(1)}$ and $v_z^{(3)}$ were used to describe the axial velocity profiles. **Left;** the power-law profile $v_z^{(1)}$ with one free parameter β. **Right;** $v_z^{(3)}$ with three free parameters. $v_z^{(3)}$ is piece-wise defined by f_1 and f_2, that intersect at point c. f_1 is again a power-law profile that describes the axial velocity in the core. f_2 is a second-order polynomial and that can describe zero flow near the wall. Point d determines the transition width of the sigmoid-shape.

Axial velocity profiles

The velocity profiles that occur in the selected geometries were studied (Fig. 2, middle row) and based on the CFD results, two functions with different complexities were defined to describe the axial velocity profile. First, a simple power-law function was proposed (Fig. 3, Left), previously used by[12,20,21]:

$$v_z^{(1)} = v_{z,\max} \left(1 - \left(\frac{r}{a}\right)^{\beta} \right) \qquad \text{with} \quad r \in [0, a] \tag{4.3}$$

was defined as the radius of the geometry. a(z) was derived as the average radius from the irregular IVUS cross sections. With this a(z) a corresponding A(z) was calculated. The flow q is constant throughout the geometry:

$$q = \int v_z^{(1)} dA \tag{4.4}$$

Eq. 4.3 was rewritten to:

$$v_z^{(1)} = \frac{q}{\pi a^2} \frac{\beta+2}{\beta} \left(1 - \left(\frac{r}{a}\right)^{\beta} \right) \tag{4.5}$$

This function has one free parameter β(z), which determines the shape of the profile. If β=2, Eq. 5 results in a Poiseuille profile and a β>2 results in a more plugged profile. The lower limit of β was set to be larger than 1 to ensure a smooth and continuous profile.

As the power-law profile has only one free parameter, it cannot adapt to all the velocity profiles observed in the CFD results, and is especially unable to capture the sigmoid-shaped profiles that can occur in segments with increasing lumen area (Fig 2, middle row, Panels III and IV). We therefore introduced a second velocity profile $v_z^{(3)}$, which has three free parameters (β, c and d). The two additional parameters provide more freedom

to match the observed profiles. $v_z^{(3)}$ is a piecewise function defined by f_1 and f_2 (Fig. 3, Right):

$$v_z^{(3)} = \begin{cases} f_1 & if \ 0 \leq r \leq c \\ f_2 & if \ c \leq r \leq a \end{cases} \tag{4.6}$$

Point c ($0 < c \leq a$) separates the two functions. The above power-law function described above is retained to describe the profile between the center and point c.

$$f_1 = \frac{q}{\pi d^2} \frac{\beta+2}{\beta} \left(1 - \left(\frac{r}{d}\right)^{\beta}\right) \qquad with \quad r \in [0, c] \tag{4.7}$$

In f_1, point d ($c < d \leq a$) determines the transition width in sigmoid-shaped profiles. Function f_2 describes the profile between point c and the wall:

$$f_2 = \gamma_3 r^2 + \gamma_2 r + \gamma_3 \qquad with \quad r \in [c, a] \tag{4.8}$$

Function f_2 is able to describe zero flow and reversed flow near the wall. The transition between f_1 and f_2 must be continuous and smooth. f_2 must therefore satisfy:

$$f_2(a) = 0$$

$$f_2(c) = f_1(c) \tag{4.9a, b, c}$$

$$\left.\frac{df_2}{dr}\right|_c = \left.\frac{df_1}{dr}\right|_c$$

With these three conditions the values for the three γ's in Eq. 4.7 were found directly. Functions f_1 and f_2 combined lead to $\hat{v}_z^{(3)}$. This profile has to be scaled to the assigned flow q. The flow with $\hat{v}_z^{(3)}$ is:

$$q_n = \int v_z^{(3)} dA \tag{4.10}$$

With it $\hat{v}_z^{(3)}$ was scaled:

$$v_z^{(3)} = \hat{v}_z^{(3)} \frac{q}{q_n} \tag{4.11}$$

Radial velocity profiles

Eq. 4.2 also contains the radial velocity v_r. This was derived from the expression for the conservation of mass:

$$\frac{1}{r}\frac{\partial}{\partial r}(rv_r) + \frac{1}{r}\frac{\partial v_\theta}{\partial \theta} + \frac{\partial v_z}{\partial z} = 0 \tag{4.12}$$

If v_z is known and axisymmetry is assumed, v_r becomes the only unknown in Eq. 4.12. $v_z^{(1)}$ enabled us to find an analytical solution for v_r:

$$v_r = \frac{qr}{\pi a^3}\frac{\beta+2}{\beta}\left(1-\left(\frac{r}{a}\right)^\beta\right)\frac{\partial a}{\partial z} + \frac{qr}{\pi a^2 \beta}\left(\left(\frac{r}{a}\right)^\beta \ln\left(\frac{r}{a}\right) + \frac{1}{\beta}\left(1-\left(\frac{r}{a}\right)^\beta\right)\right)\frac{\partial \beta}{\partial z} \quad (4.13)$$

In the case of $v_z^{(3)}$ the radial velocity was derived numerically.

Numerical implementation

With the axial and radial velocities defined, the pressure-drop can be computed directly with Eq. 4.2. First, Eq. 4.2 was integrated in the cross sectional direction:

$$\int \frac{dp}{dz}dA = \int f(v_r, v_z)dA \qquad (4.14)$$

$f(v_z, v_r)$ represents the terms in Eq. 4.2 that contain the velocities. To obtain the pressure-drop, Eq. 4.14 was subsequently integrated in the axial direction:

$$\Delta p = \int \frac{dp_{area}}{dz}dz, \qquad (4.15)$$

where $\frac{dp_{area}}{dz}$ follows from Eq. 4.14 after integration. The computations were performed with a Matlab code developed in-house (Matlab 2011b, Mathworks, Natick, U.S.), and generally lasted 10^{-1} s.

Validation

The pressure-drop from CFD was considered as the gold standard. To validate the method, the estimated pressure-drop was compared to the pressure-drop from CFD (Δp_{CFD}). Velocity data from CFD were obtained per cross section with a step size of $\Delta z = 0.25$ mm. The pressure-drop prediction was independent of the step size at $\Delta z = 0.25$ mm. $v_z^{(1)}$ and $v_z^{(3)}$ were fitted on the CFD data (Fig 2, middle). The fits of $v_z^{(1)}$ gave $\beta_{(1)}$ and those of $v_z^{(3)}$ in $\beta_{(3)}$, c and d. With the fits the pressure-drop was computed with the above described method: $v_z^{(1)}$ resulted in $\Delta p_{(1)}$ and $v_z^{(3)}$ in $\Delta p_{(3)}$. The comparison between the pressure-drops showed how well the proposed method performs when the velocity profile is optimally captured.

Pressure-drop prediction

The next step was to predict the velocity profiles and thus the parameter $\beta_{(1)}$, to derive the pressure-drop solely on the basis of geometry. Although the addition of the two parameters in $v_z^{(3)}$ improved the fits of the velocity profile, it did not improve the pressure-drop prediction (as shown in the result section). Therefore the prediction of the

velocity profiles was only performed for $v_z^{(1)}$, which has one free parameter β. At a given location $v_z^{(1)}$ depends on the local geometry and on the velocity profile in the preceding cross section. β was related to the geometry by the cross sectional area change $\left(\frac{\partial A}{\partial z}\right)$. The β in the preceding cross section was noted as $\beta(z-\Delta z)$. With these dependencies, the behavior of β was described by a first-order polynomial:

$$\beta(z) = 2 + C_1 \frac{\partial A}{\partial z} \Delta z + C_2 (\beta(z - \Delta z) - 2)\Delta z \tag{4.16}$$

The β's per cross section were obtained from the fits on the CFD results and combined with the corresponding geometrical parameters. Eq. 4.16 was fitted on this data with a least squares method (Matlab 2011b, Mathworks, Natick, U.S.). The average values of C_i were obtained for each Re. The relation between C_i and Re was described with a second-order polynomial:

$$C_i(Re) = D_{1i}Re^2 + D_{2i}Re + D_{3i} \tag{17}$$

By fitting on the C_i's, the values of the coefficients D_{ij} in Eq. 4.17 were obtained. The coefficients D_{ij} can be used to predict $\beta(z)$ in all geometries.

CFD was performed in ten geometries for ten different Re, resulting in 100 cases. To validate the prediction method, leave-one-out cross-validation was used. For this, one case was selected and the coefficients in Eq. 4.17 were found with the 81 remaining cases consisting of the other nine geometries and nine inlet flows. The coefficients that were found were used to predict $\beta(z)$ for the selected case. $\beta(z)$ was then used to directly predict the pressure-drop (Δp_{geom}). This procedure was repeated for all 100 cases.

Variables were presented as means ± 1 standard deviation.
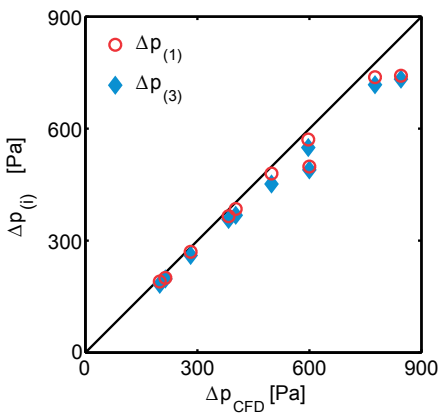

Fig. 4: Comparison of the found pressure-drops in the ten geometries at Re=150. Δp_{CFD} is the pressure-drop computed with CFD and $\Delta p_{(i)}$ is the pressure-drop based on fits with either $v_z^{(1)}$ or $v_z^{(3)}$. A similar pressure-drop was found with Δp_1 (circle) and Δp_3 (diamond), and an good agreement with Δp_{CFD} was found for both.
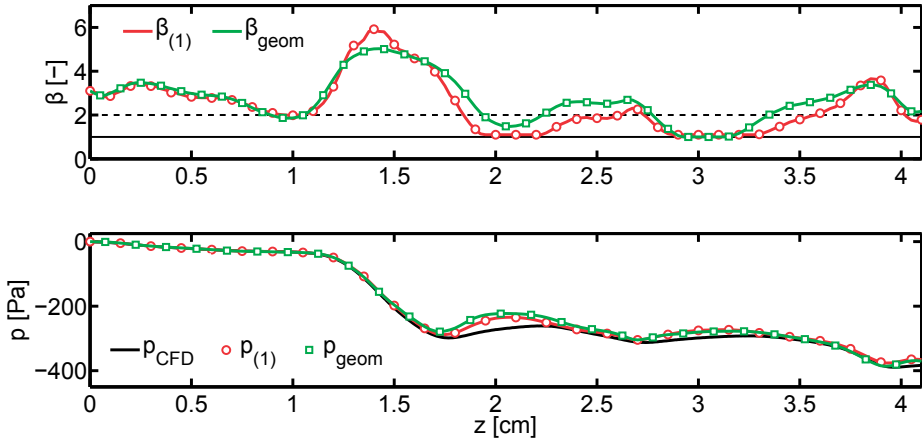
Fig. 5, Top: The distribution of β as a function of the axial coordinate of the geometry shown in Fig. 1. $\beta_{(1)}$ (red) was found by fitting $v_z^{(1)}$ on the CFD data. β_{geom} (green) was predicted based on geometry and closely followed $\beta_{(1)}$. Around z=1.5cm the geometry narrows causing a plug profile that resulted in the high values for β. Around z=2cm and z=3cm, the lumen area increases. Here a sigmoid-shaped profile was observed, what results in a β close to 1. **Bottom:** The pressure-drop as a function of the axial coordinate, where p_{CFD} (black) is found by CFD, $p_{(1)}$ (red) was calculated with the velocity profiles defined by β_1, and p_{geom} (green) by β_{geom}.

RESULTS

The five panels in the middle row of Fig. 2 illustrate the various profiles that occurred in the straightened coronary arteries. The results of CFD were displayed by plotting the axial velocity components versus the distance to center of the cross section. The cross-sections are patient-specific and thus not circular, which resulted in the different velocities at a given radius. At the entrance the velocity profile was nearly parabolic (Panel I). Where the lumen narrowed a plug profile developed (Panel II), while a sigmoid-shaped profile appeared in sections where the lumen widened (panel III and IV). $v_z^{(1)}$ adequately fitted on the parabolic and plug-shaped profile, but was not able to capture the sigmoid-shaped profile. $v_z^{(3)}$ captured all the effects seen in the CFD results.

The pressure-drop in Fig. 2 declined rapidly in the stenosed regions (point II). As the lumen widened again the pressure recuperates somewhat. The behavior of Δp_{CFD} is captured well by both $\Delta p_{(1)}$ and $\Delta p_{(3)}$, except that the pressure recuperation is slightly overestimated. At Re=150 (high physiological flow conditions), $\Delta p_{(1)}$ and $\Delta p_{(3)}$ both met the benchmark of Δp_{CFD}. They did, however, underestimate Δp_{CFD} increasingly for higher Re (Fig. 4). For the ten geometries, the mean difference between $\Delta p_{(1)}$ and $\Delta p_{(3)}$ never exceeded 3.3%.

	D_{1i}	D_{2i}	D_{3i}
C_1	$4.6 \cdot 10^{-4} \pm 9.0 \cdot 10^{-5}$	$-32.8 \cdot 10^{-2} \pm 2.9 \cdot 10^{-2}$	-39.3 ± 2.3
C_2	$-0.9 \cdot 10^{-4} \pm 1.5 \cdot 10^{-5}$	$3.2 \cdot 10^{-2} \pm 0.5 \cdot 10^{-2}$	35.5 ± 0.3

Table 1: Coefficients and the standard deviation of Eq. 4.17 found with leave-one-out cross-validation
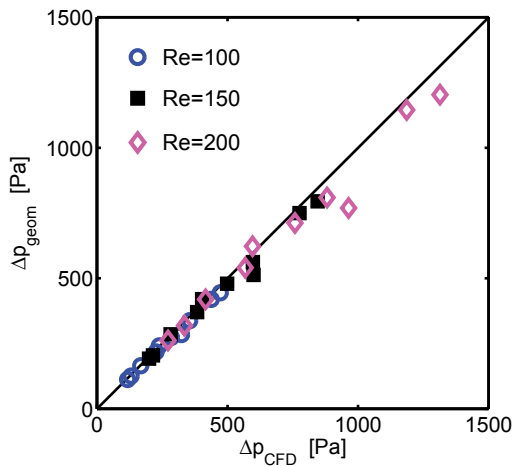
Fig. 6: The pressure-drop in the ten geometries at Re=100, 150 and 200. The Δp_{CFD} was regarded as the gold standard and compared to the pressure-drop predicted based on geometry Δp_{geom}. An excellent agreement was found between Δp_{CFD} and Δp_{geom}.
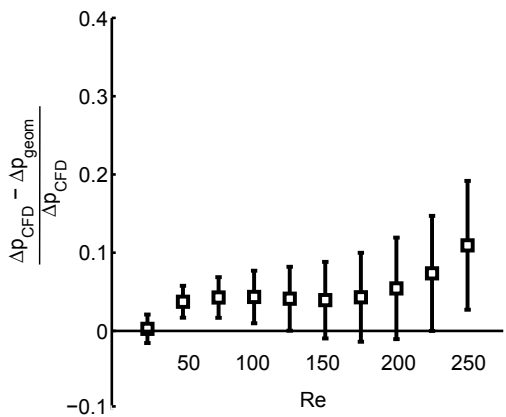
Fig. 7: The mean relative difference between Δp_{CFD} and the predicted pressure-drop Δp_{geom} in the ten geometries as a function of Re. In the physiological range, below Re=200, the relative difference is less than 5%. Above Re=200, the difference increased exponentially.

Since the pressure-drop could accurately be computed with $v_z^{(1)}$, only the β in $v_z^{(1)}$ needed to be predicted and not in $v_z^{(3)}$. The behavior of $\beta_{(1)}$ in the geometry from Fig. 2 was first derived from CFD the result and plotted in Fig. 5. The flow was nearly developed at the entrance, resulting in a $\beta_{(1)}$ between 2 and 3. A plug-profile developed in segments where the lumen narrowed, which caused $\beta_{(1)}$ to increase up to approximately 6. The sigmoid-shaped profile is not captured well, resulting in a $\beta_{(1)}$ at the limit of 1. Subsequently, β_{geom} was predicted on the basis of geometry and Re, and closely followed $\beta_{(1)}$ (Figure 5, Top). With β_{geom}, the pressure-drop Δp_{geom} was accurately predicted (Figure 5, Bottom). The mean and standard deviation of the coefficients for β_{geom} were found with leave-one-out cross-correlation are presented in Table 1.

The Δp_{geom} was estimated with high accuracy in all ten geometries. Fig.6 shows that Δp_{geom} nicely meets the benchmark Δp_{CFD} at Re=100, Re=150 and Re=200. The absolute difference between Δp_{CFD} and Δp_{geom} was small compared to the mean pressure-drop. At Re=150, the difference was 35.7±36.0 Pa where the mean Δp_{CFD} was 479.7 Pa. At Re=250 this increased to 109.9±124.6 Pa and a mean Δp_{CFD} of 1025.6 Pa. And thus the relative differences were 3.9±4.9% at Re=150 and 10.9±8.2% at Re=250. Up to Re=200 the relative difference was less than 5%, after Re=200 the difference increased exponentially (Fig. 7).

DISCUSSION

In this study we investigated a method for predicting the pressure-drop in straightened coronary arteries that are mildly diseased. By straightening the coronary arteries the complexity of the flow field was reduced. The NS equation was simplified and assumed velocity profiles were used to compute the pressure-drop. We found that the pressure-drop computed with velocity profiles that have only one free parameter β, matched the pressure-drop from CFD, which was regarded as the gold standard. This β was successfully related to geometry and flow. This approach quickly and accurately predicts the pressure-drop at physiological conditions, and slightly underestimates it at higher Re. Combining the model proposed in this study with proximal pressure measurements, a model of the microvascular resistance, and a 3D model for the region of interest, will allow us to compute the shear stress distribution in the 3D segment.

Despite that the momentum balance is not fully taken into account, the pressure-drop was estimated with high accuracy. Only in regions with a relatively large change in lumen area the pressure-drop estimation deviated from the CFD result. The radial pressure-drop was neglected and it becomes higher in areas with a large change in lumen area, and therefore the estimated total pressure-drops $\Delta p_{(1)}$ and $\Delta p_{(3)}$ deviated more. This

explains the deviation seen at higher Re as well. Subsequently we checked if the type of fit on the velocity fields influenced the pressure-drop estimation. Although $v_z^{(3)}$ matched the velocity profiles from CFD better than $v_z^{(1)}$, it did not improve the pressure-drop estimation much. This means that the deviation of the pressure-drop estimation can mainly be attributed to neglecting the radial term in the NS equation. Since the axial pressure-drop is much larger than the radial, the pressure-drop is predicted adequately with the simplification of the NS equation for mildly diseased straightened vessels. An estimate for the error associated with neglecting the radial component can be obtained by using the standard deviation of Dij given in table 1. A second finding that follows from the accurate pressure-drop estimation with $v_z^{(1)}$, is that only one free parameter β was needed. Even though $β_{(1)}$ sometimes hit the imposed limit of β>1 the estimation remained accurate. Subsequently, $β_{geom}$ was found with a linear combination of a geometrical measure and a preceding β. In straightened coronary arteries with patient-specific cross sections this gave an excellent prediction of the pressure-drop $Δp_{geom}$.

The proposed method was developed to be used in combination with steady flow simulations. Steady flow is interesting because it is indicative of the WSS that endothelial cells are exposed to over a prolonged period. Clinical studies showed that with this concept relevant information regarding plaque development is obtained[17,22,23]. Secondly, because parameters used in clinical practice, such as fractional flow reserve[24], are based on moving averages. This can be modeled by steady flow simulations as well. Since steady flow simulations only need the geometry at one chosen time point, effects such as cardiac motions or non-rigid walls can be discarded.

This study was designed to help speed up WSS computations in atherosclerotic coronary arteries with CFD. Segments proximal and distal to a plaque can be quantified from imaging data such as angiography or CT. With that imaging data patient-specific boundary condition for CFD can be imposed. For similar purposes, other studies coupled CFD to 1D models [10,20,25]. These models are based on 1D formulations of the NS equation[26–33]. These studies were able to obtain valuable time-dependent solutions. However, the models require an estimate for the capacitance of vessel wall, which is difficult to obtain for diseased wall segments. Our model used the 3D formulation as a starting point and solved it with velocity profiles based on geometrical features. Although the derivation from NS in this study was done differently than the above mentioned models, our model can still be coupled to CFD in a similar fashion. If our method is extended to a formulation that incorporates curvature, it would be interesting to see how well it performs compared to the previously developed 1D-models, since those models cannot distinguish between different degrees of curvature.

A limiting factor for a patient-specific assessment of the WSS is that curvature still has to be implemented. A previous study showed that, for instance, at Re=175 this increase was 14.8±10.0%[16]. A first possibility is to choose the same approach as that shown here, but with a curvilinear formulation rather than a cylindrical. While this leads to a mathematically more extensive formulation, it might still be possible to evaluate it. In a curvilinear form an assumed velocity profile can again be defined and subsequently be solved for the pressure-drop. A second, more pragmatic, approach would be to find a geometric measure for the curvature and relate this to the additional pressure-drop the curvature causes[16]. Apart from including 3D curvature, another limitation for accurate WSS assessment is that the microcirculation has to be taken into account, since this is a key determinant for the flow distribution. However, it cannot be visualized directly with the available imaging techniques. Although several models have already modeled the microcirculation[27,34,35], further research is still needed for the resistance distal to diseased coronary arteries. A third requirement is that the lumen segmentations in a clinical setting are based on automatic reconstructions from (bi-plane) angiography, while in this study patient-specific lumen data from IVUS were used which have more detail. The simplification of the lumen might influence the pressure-drop calculations. If so, it is possible to obtain more detail of the lumen with rotational angiography or multiple views. Fourthly, in order for the model to be included in a scheme as presented in Fig. 1, it should be expanded to model the pressure drop in a bifurcation. Next, the spatial derivative of lumen area was taken into account, but the temporal derivative was not. Although we focused on steady flows, it cannot be disregarded that the lumen area changes in time, and that the choice for a fixed lumen area could influence the outcome. Finally, for this study $\beta(0)$ was taken from CFD results. Since this method aims to replace CFD this value will not be available in later applications. We found a linear relation to estimate $\beta(0)$ based on Re: $\beta_0(Re) = 1.72 + Re*15e\text{-}4$. This relation is only based on the ten geometries from this study and might therefore not be generally applicable.

In conclusion, we found that it is possible to quickly and accurately predict pressure-drop on the basis of geometry and flow in straightened coronary arteries that are mildly diseased. Future studies should focus on adding curvature to further advance to patient-specific pressure-drops predictions.
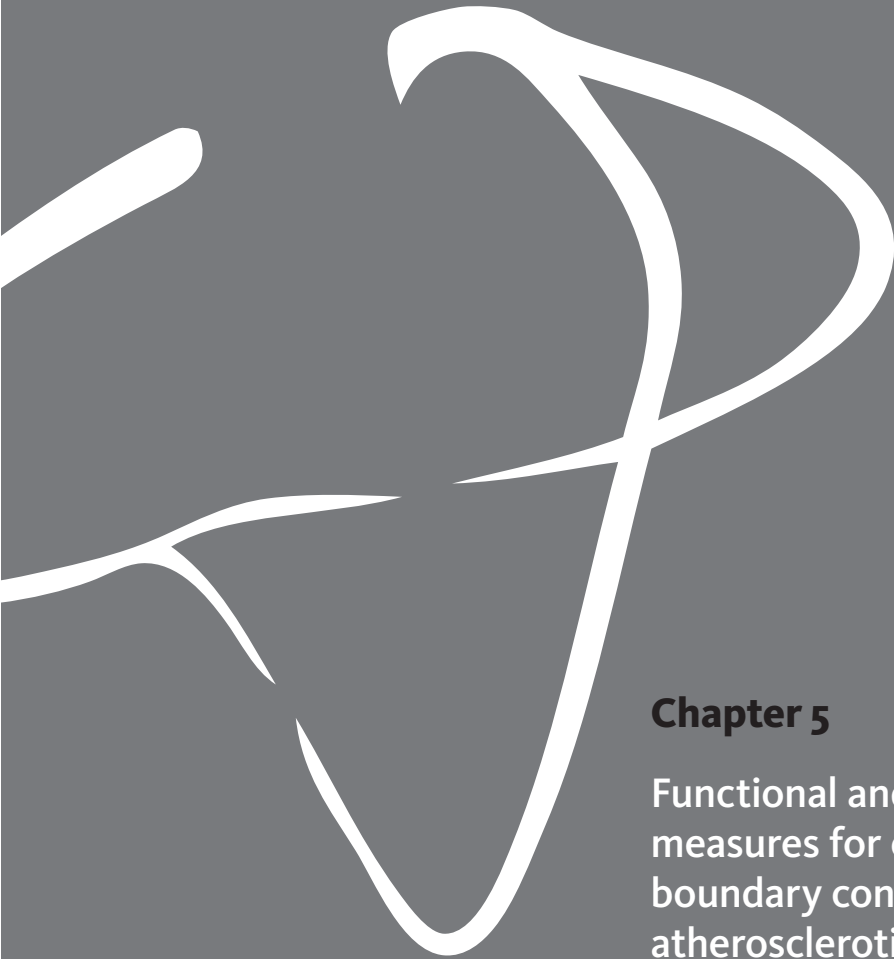
Chapter 5

Functional and anatomical measures for outflow boundary conditions in atherosclerotic coronary bifurcations

ABSTRACT

The aim of this research was finding the influence of anatomy-based and functional-based outflow boundary conditions for computational fluid dynamics (CFD) on fractional flow reserve (FFR) and wall shear stress (WSS) in mildly diseased coronary bifurcations. For ten patient-specific bifurcations three simulations were set up with different outflow conditions, while the inflow was kept constant. First, the outflow conditions were based on the diameter of the outlets. Second, they were based on the volume estimates of the myocardium that depended on the outlets. Third, they were based on a myocardial flow measure derived from computed tomography perfusion imaging (CTP). The difference in outflow ratio between the perfusion-based and the diameter-based approach was -7 p.p. [-14 p.p.: 7 p.p.] (median percentage point and interquartiles), and between the perfusion-based and volume-based this was -2 p.p. [-2 p.p.: 1 p.p.]. Despite of these differences the computed FFRs matched very well. A quantitative analysis of the WSS results showed very high correlations between the methods with an r^2 ranging from 0.90 to 1.00. But despite the high correlations the diameter-based and volume-based approach generally underestimated the WSS compared to the perfusion-based approach. These differences disappeared after normalization. We demonstrated the potential of CTP for setting patient-specific boundary conditions for atherosclerotic coronary bifurcations. FFR and normalized WSS were unaffected by the variations in outflow ratios. In order to compute absolute WSS a functional measure to set the outflow ratio might be of added value in this type of vessels.

INTRODUCTION

When studying atherosclerosis in coronary arteries several hemodynamic parameters are of interest. Two of them can directly be obtained with computational fluid dynamics (CFD). The first is fractional flow reserve (FFR), a well-established parameter in clinical practice to direct treatment of coronary artery disease[1]. FFR is defined as the pressure ratio over a coronary stenosis during hyperemia, which in clinical practice is derived from time-averaged pressure measurements[2]. The second parameter is time-averaged wall shear stress (WSS), for which there is mounting evidence that it plays a key role in atherosclerotic disease progression. Sites with low or oscillatory WSS patterns have a higher propensity to develop atherosclerosis, yielding coronary bifurcations to be at high risk of developing lesions[3–5]. WSS computed with CFD could potentially help detecting regions at risk in mildly diseased bifurcation before they can progress to advanced stages of atherosclerosis.

In order to perform CFD computations the geometry of a coronary bifurcation is needed, together with boundary conditions for the inlet and outlets. Multiple tools are available to reconstruct the patient-specific geometry of coronary arteries[6]. But patient-specific models for outflow boundary conditions are lacking, especially when applying CFD to coronary bifurcations. Outflow boundary conditions can be based on in-vivo pressure or flow measurements. These types of measurements, however, require intracoronary insertion of catheters, are time-consuming and expose the patient to risk or inconvenience. We sought to investigate if we can determine outflow boundary conditions for coronary bifurcation based on non-invasive imaging techniques.

Dynamic computed tomography perfusion (CTP) is an emerging non-invasive imaging technique. It measures the myocardial blood flow based on the distribution of contrast medium [7]. The advantage of CTP over other myocardial perfusion imaging modalities, such as positron emission tomography and single-photon emission computed tomography, is that it captures both the anatomy and the myocardial perfusion. Myocardial volumes depending on a specific branches of the coronary tree can be segmented from CTA data[8]. By combining these volumes with CTP measurements the relative flow distribution in a bifurcation is obtained. Therefore CTP could provide a functional measure to determine the outflow boundary conditions of the bifurcations.

However, CTP requires scans at multiple time points and therefore exposes the patient to a relatively high radiation dose. In light of this, we also investigated two other methods that require less exposure to radiation. With the two methods anatomical measures were obtained and used to set the outflow boundary conditions. With computed tomography angiography (CTA) - that requires only one scan - the volume of the dependent myocardium was acquired. The size of myocardial volume can be regarded as representative for the flow demand[9]. For the diameter it was also hypothesized that its size adapts to

the flow demand at resting conditions[10]. CTA allowed for diameter measurements of the branches of the bifurcations as well.

The aim of this research was to find how outflow boundary conditions for CFD affect blood flow in atherosclerotic human coronary bifurcations. The outflow boundary conditions were either based on a functional measure from CTP or on an anatomical measure from CTA. This study focused on how the different outflow boundary conditions affect the computed FFR and WSS.

METHODS

Coronary bifurcations were imaged by CTA and subsequently reconstructed in order to perform CFD. In all computations the outflow conditions were defined as a flow ratio over the two outlets. Per bifurcations three different methodologies were followed to define the outflow ratios over the outlets. First, it was based on the diameter of the two branches distal to the bifurcation using a scaling law. Second, it was based on the volumes of the myocardium that depended on the outlets of the coronary bifurcation. Third, the outflow ratio was based on a myocardial flow measure derived from CTP. We studied how FFR and WSS obtained with the anatomy-based outflow ratios differ from the results from the CTP-based ratio. These steps are discussed in detail below.

Patient selection

For this study we selected ten bifurcations of patients suspected of coronary artery disease, who were scheduled for invasive coronary angiography and were included in a CTP study[11]. All patients underwent a CTA and CTP, and provided written informed consent. The ten bifurcations were selected based on four criteria: First, excellent CTA image quality; second, a bifurcation with a minimal main branch length of 25 mm allowing for a detailed evaluation of the flow dynamics, and no other side branches visible on the CTA data; third, no stents; fourth, no heavy calcifications. Five bifurcations were located in the left anterior descending (LAD), three in the left circumflex (LCx) and two in the right coronary artery (RCA).

Imaging

A detailed description of the scan protocols has previously been reported[11,12]. Briefly, all acquisitions were made with a second generation dual source CT scanner (Somatom Definition flash, Siemens, Forcheim, Germany). First the CTA acquisition was performed, with a resulting spatial resolution of 0.6x0.6x0.6 mm³. CTP is generally performed as a stress-test, using adenosine to induce maximal hyperemia, i.e. maximal myocardial flow. Intravenously infusion of adenosine was started three minutes prior to the CTP

acquisition. The CTP acquisition lasted 30 s. The myocardial contrast enhancement as a function of time was measured and a time-attenuation curve was constructed[7]. From this curve the myocardial blood flow was computed. The resulting blood flow is typically expressed in ml/100ml/min. The temporal sampling interval was 2 to 4 seconds depending on heart rate. The voxel size was 0.4x0.4x3.0 mm³ with approximate 7.3 cm coverage of the heart in cranial direction.

Volume and mesh generation

In order to reconstruct the coronary arteries, the lumen of the bifurcation was segmented with an in-house developed segmentation tool (Fig. 1A&B) (MevisLab, Bremen, Germany)[13,14]. In the CTA data the two centerlines of the bifurcation were manually annotated and subsequently perpendicular to the centerlines the lumen contours were segmented. The step size between the contours was set to 0.8 mm and reduced to 0.4 mm when lumen irregularities required it. From the resulting contours a volume was created. The volume was then smoothened (VMTK, Orbix, Bergamo, Italy[15]) to remove artifacts resulting from the volume reconstruction (Fig 1C). The inlet was extended with five times the radius to ensure a smooth inlet profile for the CFD computations. An outlet extension was added to exclude upstream effects due to the imposed boundary conditions. Prior simulations showed that an outlet extension of 5 times the radius was sufficient. From this volume a mesh with tetrahedral cells was created (ICEM-CFD 14.5, Ansys Inc, Canonsburg, US). Prior to the final computations a mesh independency study was performed. The cell size was decreased stepwise until in subsequent computations the WSS values per node did not differ more than 3%. Special attention was paid to critical zones at and surrounding a lumen narrowing. Finally, a typical cell size of 0.10
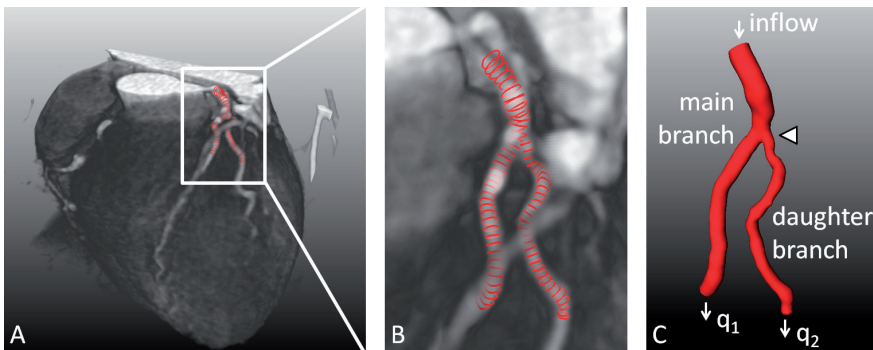
Fig. 1: 3D reconstruction of a coronary bifurcation based on CTA data. **A:** 3D visualization of the heart from CTA data. In a section of the LAD and the first diagonal contours of the lumen were segmented (red). **B:** Close-up of panel A. **C:** Based on the contours a 3D volume was generated that was used for flow computations. The white triangle indicates the diseased portion of the vessel. q_1 and q_2 indicate the two outflows of the bifurcation.

mm was used and a 5 element prism layer was added at the wall. This resulted in a mesh size between $3 \cdot 10^6$ and $6 \cdot 10^6$ cells per mesh depending on the volume of the lumen.

Computational Fluid Dynamics

A commercial available finite volume solver was used to perform steady-state flow computations (Fluent 14.5, Ansys Inc, Canonsburg, US). Steady-state flow simulations were chosen since FFR and WSS are based on time-averaged information. The wall was modeled as rigid. The blood was modeled as a non-Newtonian fluid with a Carreau model with the parameters taken from Cho and Kensey [16], and a density of 1060 kg/m^3.

In order to determine the influence of the different outflow boundary conditions, the inflow rate was kept constant while applying the three methodologies for each bifurcation. To find a representative inlet flow rate for each case, a diameter-flow relation was employed:

$$q_{in} = 1.43 \cdot d^{2.55}$$

This diameter-based relationship for baseline flow was previously derived from a patient group similar to one used in this study. Subsequently this flow rate was multiplied with a factor three corresponding to the increase in flow when hyperemia is induced with adenosine[17]. A Poiseuille profile was prescribed at the inlet based on the inflow rate. Hyperemic conditions were simulated because FFR and CTP were assessed at hyperemic conditions as well. This resulted in WSS at hyperemic conditions. CTP measurements at resting conditions were not available.

Outflow boundary conditions

In all computations the outlet boundary conditions were set as a flow ratio of q_1 over q_2 of the two outlets of a bifurcation (Fig. 1C). This outflow ratio was determined following three different methodologies (Fig. 2). For the first methodology, a trained reader measured the mean diameter in the daughter branches of the bifurcations. It was hypothesized that the diameter adapts to the chronic flow demand. In a previous report it was demonstrated that the flow distribution in coronary bifurcations is related to the diameters of the two daughter branches[18]. Therefore sections were selected based on the following requirements: First, with no discernible calcium and/or lumen intruding plaque were present in the original CTA images. Second, the section showed minimal tapering. Third, as close to the bifurcation as where the aforementioned criteria were met. The reader was free in selecting the length of a section. With the two diameters and a scaling law the first set of outflow ratios was determined (Fig. 2A, Table 1):

A. Diameters of the daughter branches

B. Volumes of the myocardium

C. CTP-derived flow
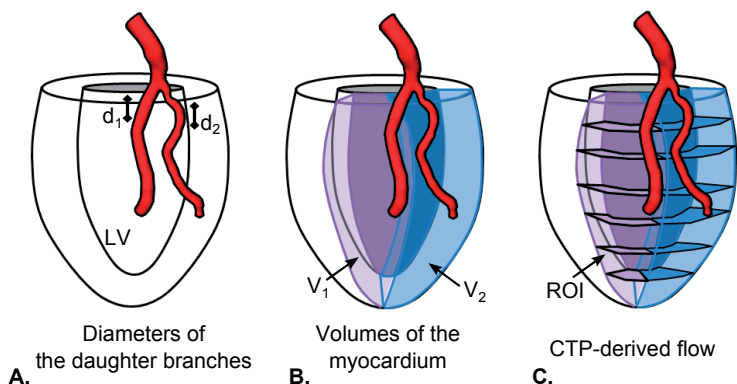
Fig. 2: For ten bifurcations three outflow ratios were determined using different methodologies. **A**: The flow ratio was determined based on the mean diameters (d1 and d2) of the daughter branches just distal of the bifurcation. **B:** For the second approach the two volumes (V1 and V2) of the myocardium depending on the outlets of the bifurcations were used to set the ratio. **C:** The third approach used the mean myocardial flow from ROIs within the CTP data of the two volumes. The volume multiplied by the mean myocardial flow within that volume was used to determine the flow ratio.

Case	Branch	Diameter [mm]	Flow ratio [%]	Volume [ml]	Flow ratio [%]	Perfusion [ml/100ml/min ± SD]	Flow ratio [%]
1	LAD	2.08	62	46.6	65	169.1 ± 14.8	71
	D1	1.69	38	24.8	35	130.5 ± 9.6	29
2	LCx	2.94	59	43.0	51	80.0 ± 14.6	52
	MO	2.52	41	41.1	49	77.5 ± 17.4	48
3	RDP	3.02	78	50.5	73	98.1 ± 10.9	75
	RPL	1.73	22	18.4	27	91.4 ± 76	25
4	LAD	1.74	48	58.6	70	131.2 ± 12.1	72
	D1	1.79	52	25.0	30	117.3 ± 10.5	28
5	LAD	2.19	49	49.9	55	109.5 ± 18.2	57
	D1	2.23	51	41.7	45	99.9 ± 12.7	43
6	LCX	2.46	54	27.9	42	37.0 ± 7.6	27
	MO	2.29	46	38.4	58	71.8 ± 5.9	73
7	LAD	2.56	46	41.3	60	64.1 ± 9.7	60
	D1	2.74	54	27.0	40	64.5 ± 14.2	40
8	RDP	2.78	57	47.2	69	64.9 ± 7.0	72
	RPL	2.45	43	21.4	31	56.8 ± 6.7	28
9	LAD	2.78	64	48.4	76	85.6 ± 14.0	78
	D1	2.15	36	15.1	24	76.8 ± 4.5	22
10	LCX	2.89	40	17.8	30	121.6 ± 7.5	32
	MO	3.48	60	41.1	70	114.3 ± 12.9	68
Median [25th - 75th]		2.46 [2.12 - 2.78]		41 [25 - 47]		88.5 [68.5 - 115.5]	

Table 1: Characteristics of the bifurcations: Mean diameter of the distal main branches and daughter branches, the myocardial volume corresponding to the outlet of the branches and mean perfusion in that volume. The reported flow ratios are defined using the characteristics. Bifurcations 1 and 2, and 7 and 8 are from the same patient.

$$\frac{q_2}{q_1} = \left(\frac{d_2}{d_1}\right)^{2.27}$$

For the second set of outflow ratios, estimates of the two myocardial volumes that depend on the two outlets of the bifurcation were used (Fig. 2B). The size of the myocardial volume can be regarded as representative for the flow demand[9]. The volumes were determined using a recently developed technique[8]. With it the centerlines of the epicardial arteries were automatically segmented from the CTA data (AZE Ltd., Tokyo, Japan). Subsequently, a seed point was placed at the carina of the bifurcation and the myocardial volume was segmented using a Voronoi-algorithm. This resulted in an estimate of the two volumes that were perfused by the two outlets. The ratio of the two volumes, V_1 and V2, were directly used to set the outflow ratio for the bifurcation.

For the third set of outflow ratios, the perfusion data from CTP was analyzed within both volumes V_1 and V_2 corresponding to the two branches of the bifurcation. Following the method previously published[11], multiple regions of interest (ROI) were drawn within the two myocardial volumes by an experienced reader. The ROIs were distributed evenly throughout the volume of interest at approximately 3 mm intervals corresponding to the resolution of the CTP data (Fig. 2C). The resulting ROIs within a volume were averaged to get the mean perfusion rate. This was then multiplied by the size of that volume to get the total flow rate for each outlet. The ratio of the flow rates was directly used as the third set of outflow ratios.

Post-processing

From the CFD results, the pressure and 3D WSS magnitude were extracted. The effects of the different outflow ratios on the FFR and the WSS results were analyzed. The FFR was defined as:

$$FFR = \frac{P_d}{P_a} = \frac{MAP - \Delta p}{MAP}$$

The mean arterial pressure (MAP) was computed using the measured systolic and diastolic pressure of each patient[19]. The distal pressure in the main branch (P_d) was defined as the MAP minus the pressure drop found with CFD (Δp).

The 3D WSS maps were converted to a 2D coordinate system for further post-processing. To this end, planes were defined perpendicular to the centerline at 0.45 mm intervals. Those planes were subdivided in 22.5° intervals. The mean WSS values within the result-

ing bins were mapped to a 2D representation. The WSS results in the main branch distal to the bifurcations were analyzed, since the largest differences in WSS between the three approaches were expected here. The WSS results from the perfusion-based approach were compared to the results from the volume-based and diameter-based approach. This was done by a point-to-point comparison of the WSS maps. On the resulting data points a linear function through the origin was fitted using a least-squares algorithm. The coefficients of the fits (k) were indicative for the general trend between the WSS results of the different methods. Finally, the WSS results were normalized to its 50th percentile to compare the relative WSS distributions resulting from the three approaches.

Summarized data is presented as the median and the 25th and 75th interquartiles. A Spearman correlation test was used as a measure for the linear dependency.

RESULTS

Outflow ratios

The median of the myocardial flow rate in this patient group was 88.5 ml/100ml/min. The first case for example had a myocardial flow rate of 169.1 ml/100ml/min through the distal main branch and 130.5 ml/100ml/min through the daughter branch (Table 1). The corresponding myocardial volumes were 46.6 ml and 24.8 ml, and the diameters of the
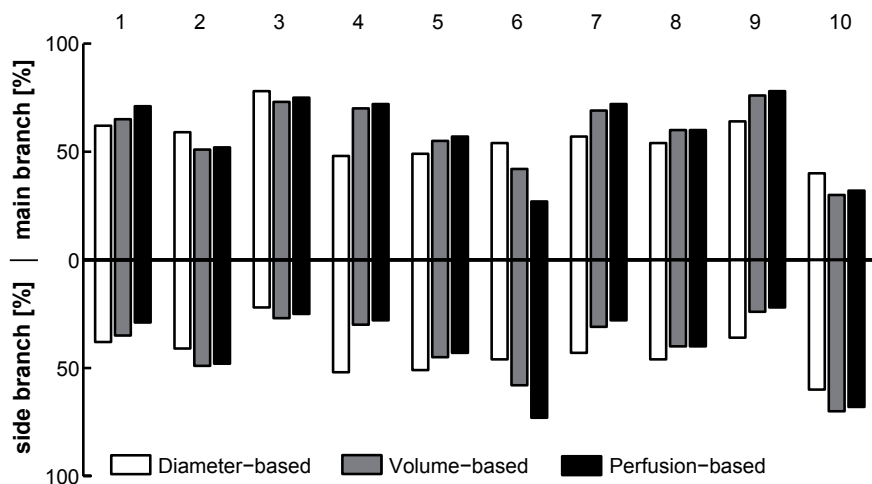
Fig. 3: The percentages of the flow going through the two daughter branches of the ten bifurcations are plotted. Per bifurcation three ratios are given that were determined by different approaches. The perfusion-based (black bars) and the volume-based (gray bars) flow ratios matched well on average. In most cases the diameter-based (white bars) ratio deviates more from the perfusion-based ratio.

branches were 2.08 mm and 1.69 mm. The flow ratios that follow from these numbers are 79%/29%, 65%/35% and 62%/38% (Fig. 3, first column). Fig. 3 shows an overview of the three flow ratios for the ten cases. First, the perfusion-based approach was compared to the volume-based approach. In general the differences were small: -2 p.p. [-2 p.p.: 1 p.p.] (percentage point), with a difference below 3 p.p. in eight out of the ten cases. Only case 1 had a 6 p.p. difference and case 6 had 15 p.p. difference. The differences between the perfusion-based and diameter-based results were larger and showed more spread: -7 p.p. [-14 p.p.: 7 p.p.]. Only case 3 had a difference less than 5 p.p., while in four cases the difference exceeded 14 p.p..

FFR

From the CFD computations the pressure drop was extracted. The pressure drop differences between the perfusion-based and the volume-based approach were small: 1% [0%:4%]. The pressure drop differences between the perfusion-based and the diameter-based computations were more pronounced: 7% [0%:18%], where five cases had a difference of more than 15%, with maxima above ±40%. With the pressure drops, the FFRs were computed. The FFRs computed with the volume-based approach (FFR_{volume}) matched the FFRs found with the perfusion-based approach ($FFR_{perfusion}$) extremely well (Fig. 4a). Fig. 4b shows the Bland-Altman plot. The mean difference between the perfusion-based and volume-based was 0.001±0.007, and for the perfusion-based versus the diameter-based this slightly increased to -0.002±0.010. Fig. 4b additionally shows that the error is
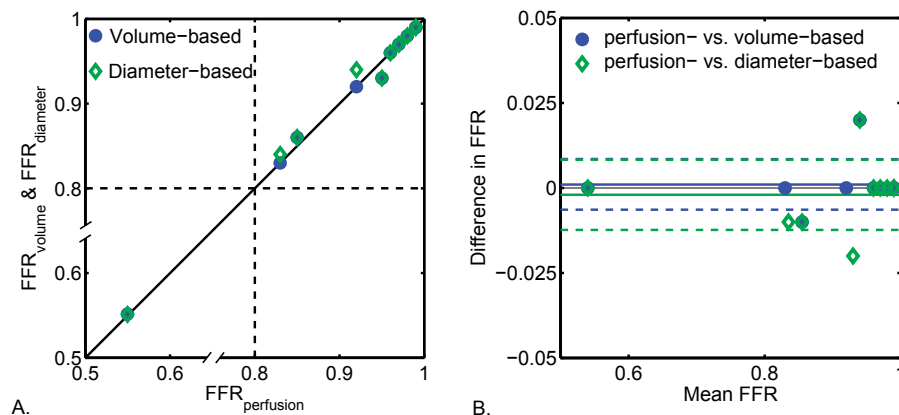
Fig. 4A: The FFR values for all ten cases computed with the three sets of outflow ratios. Both the FFR values from the volume-based (green diamond) and diameter-based approach (blue circle) matched the FFR values form the perfusion-based approach. **B:** Bland-Altman analysis of perfusion-based versus volume-based approach and perfusion-based versus the diameter-based approach.

independent of the FFR value. Thus, despite the larger differences in pressure drop, the FFRs from the diameter-based approach (FFR$_{diameter}$) performed almost equally well.

WSS

Fig. 5A shows the geometry of the first case with the WSS from the diameter-based approach. A 2D map of the same WSS is plotted in Fig. 5B. Overall high WSS were computed since hyperemic conditions were simulated. Around the ostium of the daughter branch (indicated with an asterisk) high WSS was observed, while the region directly opposite was exposed to low WSS. In the distal main branch streaks of high and low WSS were formed due to the unevenness of the underlying geometry. Qualitatively the results from the three methodologies agree nicely (Fig. 5B-D). A quantitative comparison revealed the differences in these WSS maps, shown by the point-to-point analysis in Fig. 6A. Despite the high correlations of r^2=1.00 and r^2=0.99 in case 1, the coefficients k's of 0.85 and 0.90 indicate that the diameter-based and volume-based approach generally underestimated the WSS compared to the perfusion-based approach. After normalization of the WSS data the results also quantitatively matched, with both k's being 1.00 (Fig. 6B).

In all ten cases the correlations between the absolute WSS values of the three approaches were generally very high: r^2 between 0.97 and 1.00. Only in three cases an r^2 of approximately 0.90 was found when comparing the perfusion-based and diameter-
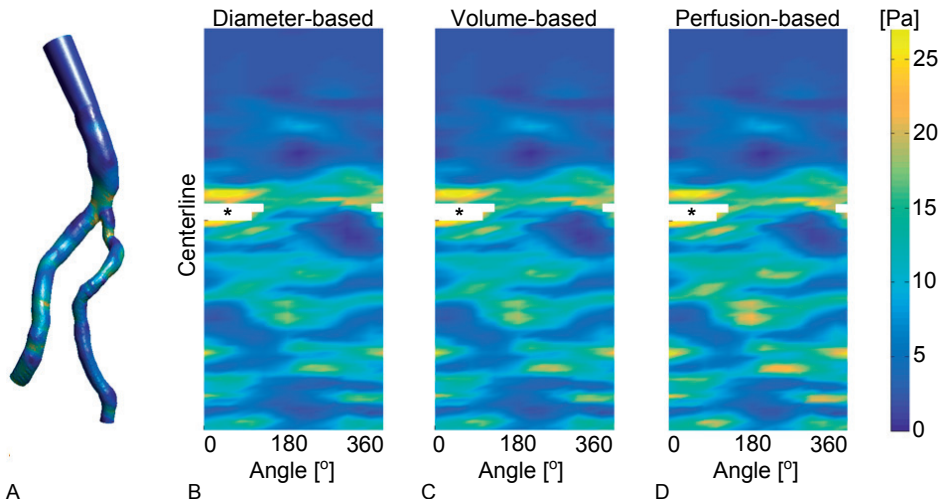
Fig. 5: WSS results in case 1 using three different approaches. **A:** The geometry of case 1 with the color map indicating the computed WSS using the perfusion-based approach. **B:** The 3D data in the main branch from the diameter-based approach was mapped to a 2D representation. **C:** 2D WSS results from the volume-based approach **D:** 2D WSS results from the perfusion-based approach. The WSS patterns from the three approaches generally matched. But the absolute values of the three approaches differed.
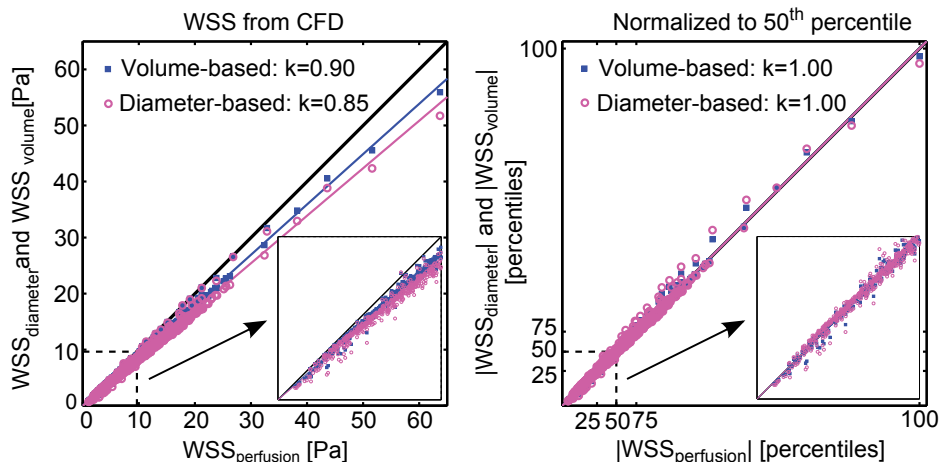
Fig. 6: A point-to-point comparison of the WSS between perfusion-based approach and the volume-based (blue square) or diameter-based approaches (pink circle). The black diagonal indicates the unity line. The blue line is a fit on the perfusion-based WSS versus the volume-based WSS. The pink line is for the perfusion-based WSS versus the diameter-based WSS. **A**: The coefficient k is 0.90 for the perfusion-based WSS versus the volume-based WSS. This coefficient is 0.85 for the perfusion-based WSS versus the diameter-based WSS. The sub-panel is a close up of the first 50th percentile of the data, indicated by the dotted line. **B**: The data from panel A is normalized to the 50th percentile. Now both coefficients are 1.00.

based approach. The mean k comparing the perfusion-based and diameter-based approach was 0.85±0.14, and with the volume-based approach this was 0.96±0.08.

After normalization, the Spearman correlations for the relative WSS were the same as for the absolute WSS values. The mean k for the diameter-based approach versus the perfusion-based approach was 0.98±0.03 after normalization. For the perfusion-based versus the volume-based approach this was 1.00±0.01.

DISCUSSION

The aim of this study was to investigate the influence of using either a functional or an anatomical measure to set outflow boundary conditions in mildly diseased coronary bifurcations. CTP data was used to derive a functional measure of the myocardium, and with CTA more conventional anatomical measures were obtained, i.e. the myocardial volume and outlet diameters. Outflow ratios from the perfusion-based and volume-based approaches matched very well, while the outflow ratio from the diameter-based approach showed larger differences. Despite those differences the computed FFRs were unaffected. The WSS on the other hand showed local deviations in the absolute values, but these differences disappeared after normalization.

Outflow ratios

The mean myocardial blood flow in this patient group was just above the previously re-ported cut-off values for diseased myocardium[11,20], which is representative for patients that are at risk of progressing to an advanced stage of atherosclerosis. In eight out of ten cases the flow did not differ more than 15 ml/100ml/min between two adjacent vol-umes. This homogeneity explains why the volume-based outflow ratio was comparable to that of the perfusion-based approach. These findings warrant further studies in larger patient populations to find if a volume measure is sufficiently representative to precisely determine the outflow ratio in bifurcations.

The diameter-based flow ratios generally deviated more from the perfusion-based ratios. The diameter-flow relationship was previously developed for mildly diseased coronary bifurcations. Two out of the four cases having the largest deviation in the flow ratios had stenosis degrees ranging from 20% to 50% near the bifurcation. This indicates that in cases with more advanced atherosclerosis the diameter-based approach might not suffice in obtaining a representative flow ratio.

FFR

Recently, the potential of CFD in clinical decision making has been shown as a non-invasive FFR measurement in support of CTA measurements[21]. The FFR computations in our study seemed relatively insensitive to the differences found for the outflow ratios. This insensitivity can be explained by the fact that the FFR is defined as the ratio of the distal and proximal pressure. A mild stenosis leads to a relatively low pressure-drop compared to the proximal pressure. Therefore, the errors made in the pressure-drop will have minor effects on the computed FFR. This further strengthens the idea that rapid FFR computation based on angiography and scaling laws could be clinically feasible and should be further explored[22–26].

WSS

For local WSS assessment proper outlet boundary conditions are essential[27–29]. In a previous study a diameter-based scaling law was derived to set the outflow for human coronary bifurcations, as an improvement on Murray's law[18,30]. Now, in a similar patient population, it was found that the absolute WSS outcome from this diameter-based ap-proach differed locally from the perfusion-based approach.

If we want to correlate WSS to markers of atherosclerosis, e.g. wall thickness, various approaches are available. A point-to-point analysis is preferable, but correlations are hard to establish due to the noisy nature of computed WSS[31]. Various averaging proce-dures were introduced to reduce to noise, resulting in multiple studies relating absolute WSS values to wall parameters[3,32]. Nonetheless, even after averaging absolute values will be different for physiological or scaled outflow boundary conditions. Relating WSS

to atherosclerosis might be accomplished by creating histograms of WSS distributions[33]. However, all local information will be lost. Alternatively by normalizing WSS local information is retained[34–36]. Due to the non-linear nature of flow phenomena in combination with the geometry features of diseased vessel walls and large difference in outflow ratios, it is difficult to predict if normalization of the WSS would yield similar results. The relative WSS, however, revealed identical regions of low and high WSS. The flow range within these types of vessels was small enough such that the normalization resulted in small differences in relative WSS. Relative WSS information might proof valuable to assess the relationship between WSS and atherosclerosis in general.

Limitations

Only a low number of patients was selected in this study. Future studies should focus on confirming the perfusion homogeneity found in this study in a larger patient cohort. For such an investigation the high image quality requirement is less pressing since a 3D reconstruction of the lumen would not be required. And although we were interested in mildly diseased bifurcations, the FFR values were relatively high. For future studies it would also be interesting to include patients with a low FFR, to investigate the perfusion homogeneity in that group. In future studies the outflow boundary conditions could also be imposed on subsequent bifurcations, opening up the selection for cases other not than single confined bifurcations.

Since only hyperemic CTP measurements were available, this study was limited to hyperemic WSS computations, while more commonly resting conditions are evaluated. However, if we consider a case where one of the two volumes distal of a bifurcation is heavily diseased, the flow demand at resting is probably still met for both volumes. The perfusion deficiency of that volume would become more apparent at hyperemic conditions. However, in our patient group a relatively homogeneous perfusion was observed at the hyperemic state. So it is likely that the flow ratio will be comparable under resting conditions. Therefore the conclusions regarding the flow ratio obtained from hyperemic CTP data are likely to hold for resting conditions.

The main advantage of combining CTA and CTP is that it allows for visualization of both the epicardial anatomy and myocardial blood flow. Nevertheless, the current study was limited to only using the relative flow information from CTP to set the outflow ratio. Given that CTP is a relatively new imaging modality, validation of it is still ongoing. Consequently, we chose to use relative and not absolute flow information. With new CT scanners being developed current limitations might be overcome, such as the temporal and spatial resolution or quantitative flow assessment. Next, the clinical validation of the used volume segmentation tool is currently limited to reliably segment myocardial area with low flow compared to single-photon emission computed tomography data. Nonetheless, the Voronoi algorithm on which it is based has proven to work for the myo-

cardium[37], but also for arterial networks[38] and smaller vessel in the subendocardium[39], making it likely that representative volume segmentations were obtained in this study as well.

In this study the inflow rate was kept constant to quantify the effect of the outflow ratio. However, also the inflow can be determined with different approaches: e.g. measurements, models or scaling laws. It is likely that different methods to set the inflow result in at least some variability. This variability in inflow could strongly influence the absolute WSS and FFR computations. Future studies should focus on quantifying the influence of the inflow variability.

Conclusions

In conclusion, we demonstrated the potential of using CTP to set patient-specific boundary conditions for CFD in atherosclerotic coronary bifurcations. We saw that FFR and normalized WSS were unaffected by the variations in outflow ratios. In order to compute absolute WSS a functional measure to set the outflow ratio might be of added value in this type of vessels.
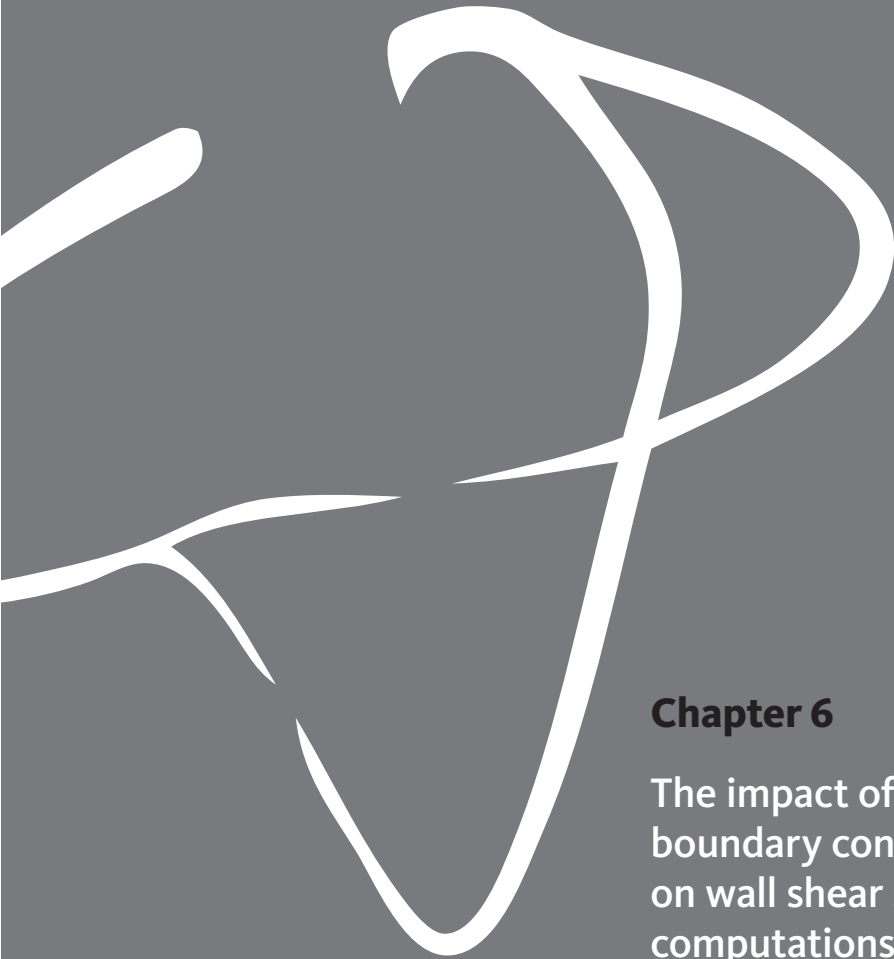
Chapter 6

The impact of scaled boundary conditions on wall shear stress computations in atherosclerotic human coronary bifurcations

ABSTRACT

The aim of this study was to determine if reliable patient-specific wall shear stress (WSS) can be computed when diameter-based scaling laws are used to impose the boundary conditions for computational fluid dynamics (CFD). This study focused on mildly diseased human coronary bifurcations since it is a known predilection site for atherosclerosis. Eight patients scheduled for percutaneous coronary intervention were imaged with angiography. The velocity proximal and distal of a bifurcation was acquired with intravascular Doppler measurements. These measurements were used to set the inflow and outflow conditions for the first set of WSS computations in the bifurcations. For the second set of computations the absolute inflow and the outflow ratio were imposed with geometry-based scaling laws based on angiography data. The WSS from the measured-approach and the scaled-approach were directly compared. A reasonable agreement was found between the measured and scaled inflows: With a median difference of 0.08 ml/s [-0.01; 0.20]. The measured and the scaled outflow ratios showed a good agreement: 1.5 percentage points [-19.0; 4.5]. The absolute WSS results showed to be sensitive to the inflow and outflow variations. The normalized WSS proved to be a robust method to acquire patient-specific WSS patterns. This study showed that normalized WSS can be obtained from angiography data alone by applying diameter-based scaling laws to define the boundary conditions. Caution should be taken when absolute WSS is assessed from computations that used scaled boundary conditions.

INTRODUCTION

Atherosclerosis in coronary arteries is accompanied by plaque development which is the underlying cause of stable angina and acute myocardial events[1]. Predilection sites for plaque development are regions near bifurcations exposed to low time-averaged wall shear stress (WSS)[2,3]. When a plaque grows and subsequently protrudes into the lumen, it becomes exposed to different WSS distributions[4]. At the location of the narrowing and proximal to that narrowing, the plaque is subjected to relatively high WSS. Evidence suggests that prolonged high WSS initiates pathobiological processes which promote plaque destabilization[5–8]. In order to better understand these processes a tool that can compute WSS in a clinical setting would be valuable.

WSS cannot be measured directly in coronary arteries, but it can be obtained by performing flow simulations with computational fluid dynamics (CFD). The first requirement to perform CFD in coronary arteries is to obtain an accurate representation of the lumen geometry. During interventions angiography is the preferred imaging technique and thus routinely available. Recent advancements in the field of image reconstruction led to on-line techniques for the reconstruction of coronary artery geometry based solely on angiography[9,10]. Angiography-based reconstruction techniques are therefore an attractive possibility to generate 3D lumen surfaces for WSS computations[11].

The second requirement for CFD in coronary bifurcations is imposing appropriate boundary conditions at the inlet and outlets. Boundary conditions can be determined based on flow measurements. Catheter-based Doppler measurements result in a quantitative velocity measure, and this technique was used in previous studies to set inflow boundary conditions for CFD[7,8,12]. While Doppler velocity measurements provide absolute velocity data, it does require insertion of an additional catheter. Instead of imposing measured velocities as boundary conditions, it is also possible to use image-based modeling techniques. Diameter-based scaling laws directly relate flow to the diameter at specific locations. The ideas were first formulated by Murray who postulated that blood flow is proportional to the diameter to the power 3 based on the assumption of energy efficiency[13]. Later studies found that the value of the power for the coronary vasculature ranged between 2 and 3 for the coronary system[14–19]. In the study by Van der Giessen et al. empirical relations were found specifically for mildly diseased coronary bifurcations[20]. These models are relatively simple and could prove to be effective in setting boundary conditions.

The accuracy of these scaling laws for boundary conditions, even in healthy arteries, is unknown. Application of these scaling laws in diseased vessels is further compromised by the fact that changes in the resistance of the distal vascular bed due to atherosclerosis are not accounted for. Nonetheless, these models are frequently used as boundary conditions[21–25]. Therefore this study investigates whether diameter-based scaling laws can be applied to impose boundary conditions to accurately compute patient-specific WSS

maps. We performed CFD simulations in mildly diseased human coronary bifurcations following two different methodologies: one where the boundary conditions were based on measurements and the other with boundary conditions derived from geometry-based scaling laws. This allowed for a direct comparison of the WSS resulting from the two approaches, and we determined whether angiography data alone is sufficient to obtain WSS data in mildly diseased human coronary bifurcations.

METHODS

Patient selection

The patient population used in this study was previously described in Nolte et al.[26]. Briefly, patients with stable angina pectoris scheduled for percutaneous coronary intervention were included. From this population, patients were retrospectively selected when three requirements were met: First, adequate image quality of the angiographic data and the angular projections needed to generate a 3D reconstruction of a coronary bifurcation. Second, two locations of guide wire-based velocity measurement had to be proximal

Measured boundary conditions

in

$$\overline{q}_{in} = \overline{v}_{in} \cdot A_{in}$$

Scaled boundary conditions

$$q_{in} = 1.43 \cdot d^{2.55}$$

$$\overline{q}_{out1} = \overline{v}_{out1} \cdot A_{out1}$$
$$\overline{q}_{out2} = \overline{q}_{in} - \overline{q}_{out1}$$

$$\frac{q_{out2}}{q_{out1}} = \left(\frac{d_{out2}}{d_{out1}}\right)^{2.27}$$

out 1   *out 2*
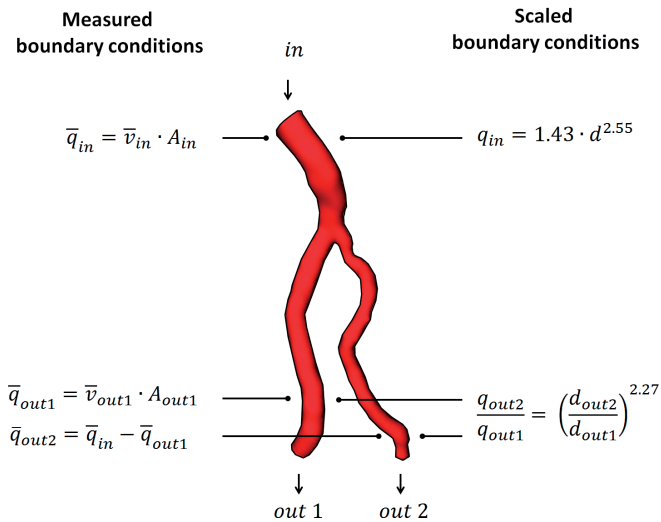
Fig. 1: Overview of a patient dataset. **A:** Angiography recording of a coronary bifurcation in the left anterior descending artery. The dashed lines indicate the region of interest. The two arrows point to the location where the velocity was measured. **B:** Second angiography recording from a different angel allowing for a 3D reconstruction. **C:** 3D reconstruction of the luminal surface of the coronary bifurcation. **D:** Intravascular velocity measurement at the proximal location. The recordings of multiple consecutive heartbeats are normalized to the length of their cardiac cycle (T) and superimposed (black lines). The purple line is the average of the recordings per time point in the cardiac cycle, with the blue area around it indicating the standard deviation.

and distal of that bifurcation, without any side branches visible on angiography other than the bifurcation (Fig. 1). Third, the velocity measurements were performed in an angiographically healthy segment. Ultimately, eight eligible cases were selected.

Geometry reconstruction

Angiography images were recorded with a Philips Integris H system (Philips Healthcare, Best, the Netherlands). Two projections were selected that optimally visualized the region of interest with minimal foreshortening and at least 30⁰ between the imaging angles. On the basis of those angiographic images 3D volumes of the coronary bifurcations were constructed using commercially available software (CAAS v3.11, Pie Medical imaging, Maastricht, the Netherlands).

Velocity measurements

The velocity in the coronary arteries was measured by catheter-based Doppler technique (Combowire XT, model 9500, Volcano Corp., San Diego, U.S.). The wire was advanced into the coronary artery where the peak cross-sectional velocity was recorded proximal and distal of the bifurcation. From these recordings multiple consecutive heartbeats during rest with a stable signal were selected (Fig. 1d); on average a period of 23±14 heart beats was used. From that period the time-averaged velocity was calculated. Velocity data was combined with diameter measurements to obtain the flow data. The local diameter was measured with conventional 2D QCA at the location of the Doppler-wire tip in the same two projections as used for the 3D reconstruction. From the mean of the diameters from two projections the cross-sectional area was determined, and by assuming a parabolic velocity distribution the flow was computed. The methodology was followed to determine the flow in the mother branch ($\bar{q}_{in}$) and in one daughter branch ($\bar{q}_{out1}$). The flow through the second daughter branch ($\bar{q}_{out2}$) was not measured but followed from conservation of mass.

Scaling laws

The flow through the inlet and daughter branches can be estimated with scaling laws. Van der Giessen et al. derived two diameter-based scaling laws from a patient population with mild coronary artery disease[20]. With the first scaling law the inflow was estimated and the second scaling law was used to estimate the outflow ratio. The first scaling law is defined as:

$$q_{in} = 1.43d^{2.55} \qquad (6.1)$$

resulting in a flow (q) for the inlet. The diameter (d) was measured at the same location as where the velocity was measured in the mother branch. The second scaling law for the outflow ratio was defined as:

$$\frac{q_2}{q_1} = \left(\frac{d_2}{d_1}\right)^{2.27} \qquad (6.2)$$

The diameter d1 was measured in the largest daughter branch and d2 in the other daughter branch. The diameters from the daughter branch with the Doppler wire was determined at the (angiographically healthy) location were the velocity was measured. In the other daughter branch the diameter was measured at an angiographically healthy section distal to the bifurcation near the ostium.

Computational Fluid Dynamics

Prior to the mesh generation flow extensions were added to the 3D volumes (VMTK, Orbix, Bergamo, Italy). To ensure a smooth inlet profile for the CFD computations the inlet was extended with five times the radius. An outlet extension of 5 times the radius was added to exclude upstream effects due to the imposed boundary conditions[27]. Meshes were built with commercially available software (ICEM v14.5, Ansys Inc., Canonsburg, US). A typical cell size of 0.1 mm was used and five prism layers at the wall were constructed. This resulted in a typical mesh size of 2×10^6 cells. Blood was modeled as a non-Newtonian fluid by applying a Carreau model with the parameters taken from Cho and Kensey[28]. The density was set at 1060 kg/m^3. The wall was modeled as rigid and a no-slip condition was imposed at the wall. A Poiseuille profile was prescribed at the inlet based on either the measured or scaled flow rate (Eq. 6.1, Fig. 2). At the outlets of the two daughter branches either the measured or the scaled outflow ratio (Eq. 6.2) was defined. Since the association of WSS with enhanced plaque vulnerability is based on time-averaged data we focused on steady flow simulations[29–32]. A finite volume solver
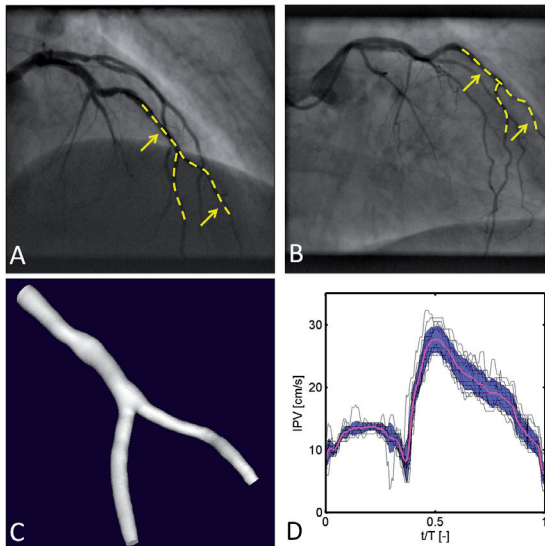
Fig. 2: Cartoon illustrating the study setup. The inflow and outflow boundary conditions for WSS computations in mildly diseased coronary plaques were set by two different approaches. First, the measured boundary conditions were used, for which the flow is measured in the mother branch and in one daughter branch. The overbars indicate time-averaged value was used. Second, the scaled-approach was used which sets the inflow and outflow conditions using diameter-based scaling laws.

was used to perform steady-state simulations using standard numerical techniques (Fluent v14.5, Ansys Inc., Canonsburg, US).

We performed two CFD simulations in 3D lumen reconstructions of all 8 geometries (Fig. 2). First intravascular velocity measurements were imposed as boundary conditions at both the inlet and outlets. Subsequently, the boundary conditions for the same cases were assigned using diameter-based scaling laws based on geometry.

Data analysis

The WSS magnitude was extracted from the CFD results and mapped to a 2D coordinate system for further analysis. First the centerline was traced (VMTK, Orobix, Bergamo, Italy). Next, cross sections were defined at 0.45 mm intervals perpendicular to the centerline. The cross sections were partitioned in sectors of 22.5^0, which resulted in 16 bins between two sequential cross sections[27]. The mean WSS of each of the bins was used to construct the 2D map. The 2D maps of the mother and daughter branches were analyzed separately. The mean WSS in the axial and circumferential direction was calculated per branch. Next, a point-to-point comparison was performed with the data from the 2D WSS maps of two approaches. A correlation plot was generated, with a linear fit going through the origin. The slope of the fit was characterized by coefficient k. A k value equal to 1 indicates that the WSS results of both methodologies are similar. Complementary to that, the value of |1-k| is a measure for the difference between the methods.

Normalized WSS was also investigated in addition to the absolute WSS. For the normalization procedure each 2D WSS map was normalized by its 50th percentile value.

Statistics

Summarized data is presented as the median and the 25th and 75th interquartiles. A Spearman correlation test was used as a measure of agreement between WSS resulting from the two methods. The outflow ratio over the outlet of the bifurcation is given in percentages of the total flow. The difference in outflow through a branch due to the different methods is therefore expressed in percentage points.

A noninferiority test was employed to find statistical evidence if the two models provide outcomes that can be regarded equivalent [33]. In this test the null-hypothesis states that the absolute WSS difference between the two models is larger than a chosen margin, which was rejected at a significance level of $\alpha=0.05$. In a previous report by Schrauwen et al. the margin to test for differences was set to 0.25 Pa, based on the resolution limitations of angiography and the effect this has on the precision with which absolute WSS can be computed [34]. The margin for normalized WSS was set using the previously reported 1.3 Pa baseline value for WSS in coronary arteries. The ration between 0.25 Pa and 1.3 Pa led to a 0.2 margin for normalized WSS.
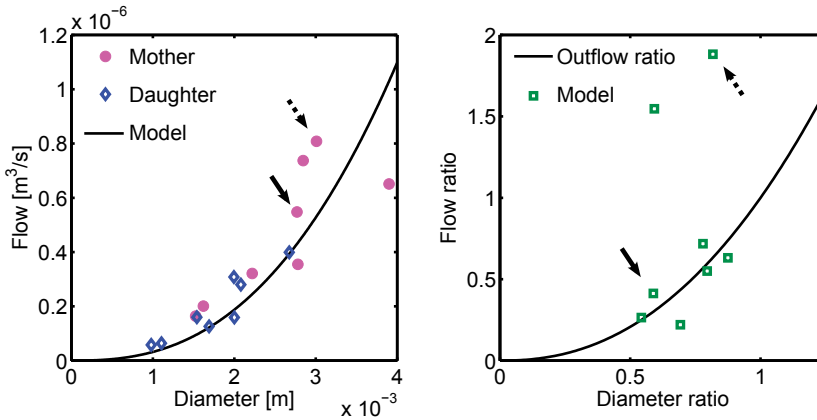
Fig. 3: Hemodynamic data from the patient populations. **A**: Measured diameter-flow relation in the mother branch (pink dots) and daughter branch (blue diamonds) of 8 patients. **B**: Measured diameter ratio of the daughter branches versus the measured flow ratio in those branches. On the x-axis the diameter ratio is defined as the smaller over the larger diameter of the daughter branches. The black lines in both panels plot the relationships derived by Van der Giessen et al. The arrow indicates the measurement associated with the case described in the result section and Fig. 4. (The dashed arrow corresponds to the case described in the supplements).

RESULTS

Fig. 3a shows the measured diameter-flow relation for the mother branch and the daughter branch. The black line is the diameter-flow relationship derived by Van der Giessen et al [20]. A similar behavior was found with a median inflow difference of 0.08 ml/s [-0.01;0.20], although the measured flow in the mother branch tends to be higher than the scaled value. In the daughter branch the difference between the measured and scaled flow was -0.01 ml/s [-0.04; 0.07]. In Fig. 3b the measured flow ratio as a function of the diameter ratio of the daughter branches is plotted, with the black line representing the relationship found by Van der Giessen et al. In 6 out of the 8 cases a good agreement was found: The median of the difference for all cases was 1.5 percentage points [-19.0;

Fig. 4 → : Overview of results for one case. The inflow was underestimated by the scaled approach, while the outflow ratios were similar. **A**: bA 3D reconstruction of the geometry with color map indicating the WSS computed with measured boundary conditions (BC). **B**: 2D maps of the computed absolute WSS with the two approaches. The maps of the mother branch and the daughter where the flow was measured are plotted. **C**: The circumferential average of the absolute WSS in the two segments for the measured-approach (blue circles) and scaled-approach (pink diamonds). **D**: Axial average in the mother branch of both methods. **E**: Axial average of the daughter branch of both methods. **F**: Normalized 2D WSS maps computed with the two methods. **G**: The circumferential averages of the normalized WSS in the mother branch. **H**: Axial average of the normalized WSS in the mother branch. **I**: Axial average of the normalized WSS in the daughter branch.
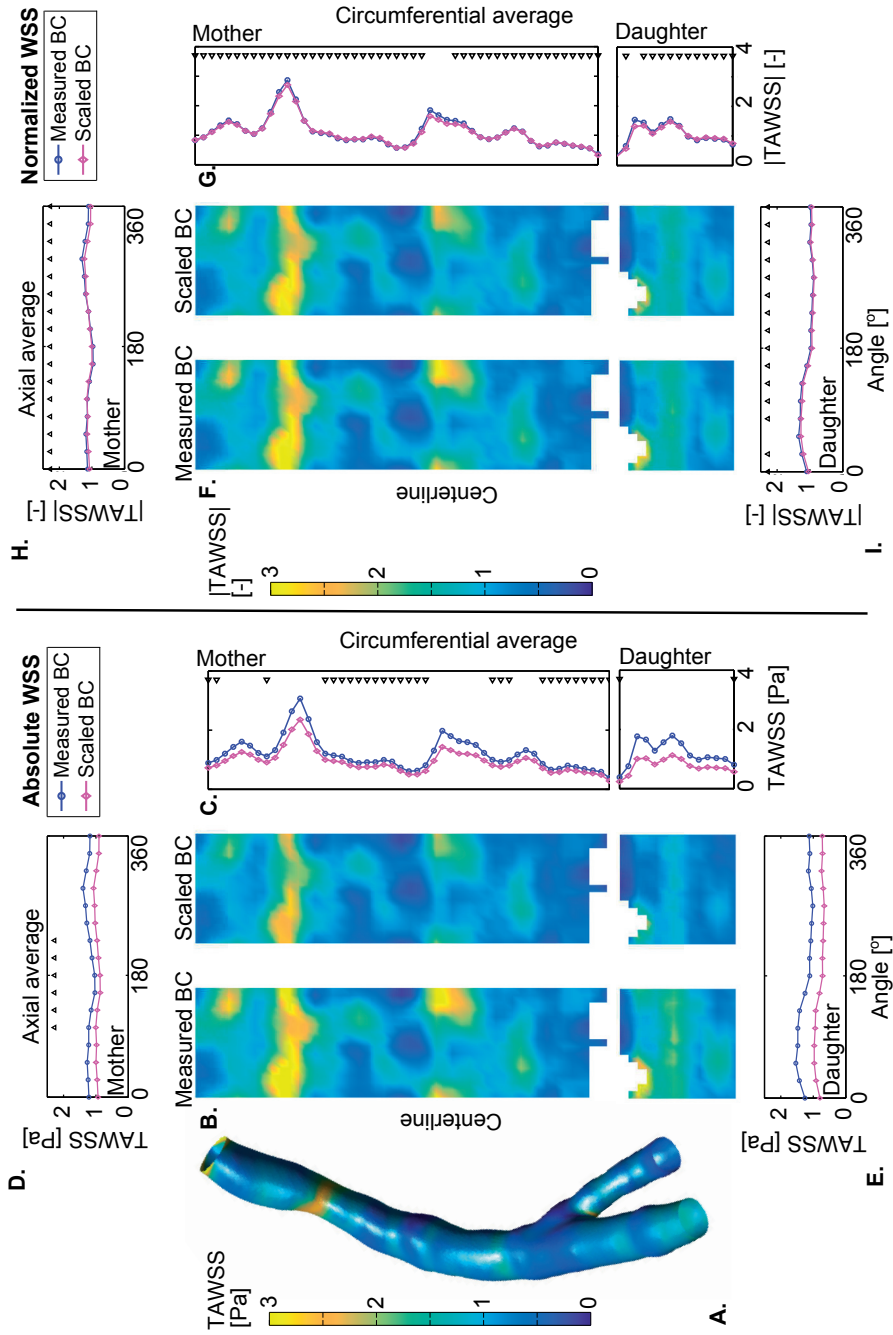
Fig. 4

4.5]. In two cases the measured flow ratio was above 1. Since d1 was defined to be large than d2, this indicates that more flow was going through the smaller daughter branch.

Fig. 4 illustrates the results for one case (arrow in Fig. 3). In this case the measured and scaled inflow differed, with a measured flow of 0.55 ml/s and a scaled flow of 0.43 ml/s. The outflow ratios for both approaches agreed nicely: 29%/71% with the measured-approach and 23%/77% with the scaled approach. In Fig. 4a the WSS computed with the measured-approach is plotted in 3D. Just distal of the inlet, the mother branch shows a lumen-intruding plaque, causing a region of high WSS. Halfway down the mother branch, a local widening of the lumen induces low WSS, immediately followed by a high WSS spot. As expected, higher WSS was found at the flow divider of the main daughter branch. The curvature of the segment is not very strong, leading to only minor asymmetries in WSS distributions. The 2D representations of the WSS computed with both approaches are plotted in Fig. 4b. In these maps the focal high WSS are clearly distinguishable. In both the mother and the daughter branch, the WSS from the scaled approach is lower than the WSS from the measured approach, due to the lower inflow but similar outflow ratio. The averaged WSS in Fig. 4c-e confirmed these observations, with more pronounced differences high WSS regions. The triangles indicate were the WSS from both methodologies can be regarded equivalent according to the noninferiority test. The majority of the mean WSS results were not equivalent.

In Fig. 4f-i the results of the same cases are given after normalization to the 50th percentile of each branch. The 2D maps in Fig. 4f show that the results were in good agreement. Also the circumferential and axial averaged normalized WSS values showed an excellent agreement between the results for the different boundary conditions. This was confirmed by the results of the noninferiority test.

	Absolute WSS				Normalized WSS			
	Circumferential		Axial		Circumferential		Axial	
Case	Mother	Daughter	Mother	Daughter	Mother	Daughter	Mother	Daughter
1	0	0	0	0	92	93	100	100
2	0	30	0	13	78	83	94	94
3	0	2	0	0	80	72	81	50
4	100	88	100	94	100	100	100	100
5	4	0	0	0	91	90	100	100
6	20	18	0	0	100	94	100	100
7	45	0	0	0	91	91	100	100
8	57	14	38	0	94	93	100	94
Mean	28±36	19±30	17±36	13±33	91±8	90±9	97±7	92±17

Table 1: Overview of the percentage of equivalence in mean WSS between the two models in axial and circumferential direction for both the mother and the daughter branch. The percentages are reported for both absolute and normalized WSS.

Table 1 gives the percentage of area per branch where the nononferiority test was positive. The absolute WSS shows little agreement in nearly all the cases. Only in case 4 the boundary conditions of the models matched exceptionally well, resulting in a high agreement. The normalized WSS shows a high agreement between the models for all the cases.

The WSS data from the 2D maps of case 2 from Table 2 are plotted in Fig. 6a. The linear fit through the WSS data in the mother branch resulted in a coefficient k=0.67 for the slope, which is indicative of the underestimation of the WSS by the scaled approach. In the daughter branch this was k=1.12, demonstrating general overestimation of the WSS. The result after normalization to the 50th percentile in the mother branch is plotted in Fig. 6b. A high agreement between the results was seen, as indicated by k=0.95 and an r^2=0.88. Similarly, also a higher agreement (k=0.94, r^2=0.92) was found in the daughter branch (Fig. 6c). In the other 7 cases the r^2 ranged between 0.90 and 1.00. These values did not change after normalization. The means of the coefficients (±standard deviation) are given in Table 2. The much smaller standard deviation of k for the normalized WSS indicates that the agreement improved between the results from the two approaches. The mean value of |1-k| indicates that the difference between the models for the normalized WSS results are much smaller than the differences found for the absolute WSS.

k	Absolute WSS		Normalized WSS	
Case	Mother	Daughter	Mother	Daughter
1	0,57	0,59	0,96	0,93
2	0,67	1,12	0,95	0,94
3	0,64	0,50	0,93	0,86
4	1,20	1,25	1,01	1,01
5	0,61	1,11	0,99	0,98
6	0,77	1,24	0,99	1,00
7	1,49	1,54	1,05	1,04
8	0,78	0,63	0,96	0,95
Mean	0.84±0.33	1.00±0.38	0.98±0.04	0.96±0.06
|1-k|				
Mean	0.33±0.11	0.32±0.16	0.04±0.02	0.05±0.04

Table 2: Overview of k for all 8 cases. This coefficient is indicative for the agreement between the two methods; when k equals one there is high agreement in the results. The bottom gives the mean of the absolute difference of 1-k.
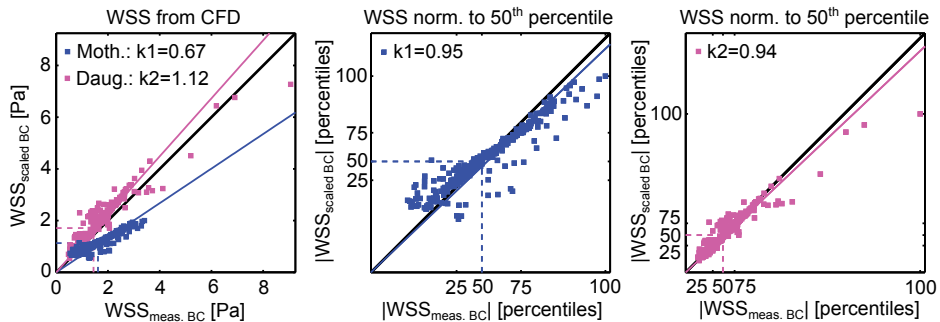
Fig.5: Quantitative comparison of the 2D WSS maps from the case in Fig. 5. **A**: The absolute WSS from the measured-approach versus the absolute WSS from the scaled-approach. The WSS in the mother segment (blue) and daughter (pink) are plotted separately. The lines represent the linear fit through the data points and the origin. The coefficient k indicates the slope of the fit. **B**: The normalized WSS in the mother branch from both methods. **C**: The normalized WSS in the daughter branch from both methods.

DISCUSSION

We studied the WSS in mildly diseased human coronary bifurcations using boundary conditions for both the inlet and outlet derived from catheter-based invasive measurements. Additionally, the inflow and outflow boundary conditions were determined by combining diameter-based scaling laws with diameter measurements from angiographic images. Although in general a reasonable agreement was found for the inflow and a good agreement for outflow ratio, the differences between the two approaches were considerable in some cases. The differences in the boundary conditions in turn led to differences in the computed absolute WSS values. However, after normalization to the 50th percentile an excellent agreement was found between the WSS maps from the two approaches.

The diameter-flow relationship used in this study was derived by Van der Giessen et al. For their derivation the used the measurement reported by Doriot et al.[35]. In the study by Doriot et al. the velocity of the blood was measured in the mother and the two daughter branches of angiographically normal coronary bifurcation of patients suffering from coronary artery disease. These measurements showed a consistent behavior and a simple diameter-based scaling law could nicely describe the diameter-flow relation[20]. We previously derived the outflow ratio of mildly diseased coronary bifurcations from computed tomography perfusion measurements, and found a high agreement between the measured and the scaled outflow ratio[27]. The results in that study showed a homogenous perfusion of the myocardium associated with the daughter branches of the bifurcations. In this study, the scaling laws generally worked well for the majority of

the cases, but in some cases it led to relatively large discrepancies in the flow estimation. For instance in the second example given in the results section (Fig. 5), the larger daughter branch received a smaller fraction of flow than could be expected based on its diameter. The deviations between the measured and scaled flow were most likely caused by differences in the resistance of the distal vascular bed. However, we could not identify these cases based on the angiography data, for instance by using the area stenosis. As long as these cases cannot be identified with angiography, caution should be taken when employing diameter-based scaling laws to estimate boundary conditions, especially for the inflow in more diseased cases.

Many studies tried to correlate absolute WSS to a marker of atherosclerosis[3,32,36]. To compute WSS in geometries with multiple outlets several studies rely on a form of scaling for setting the boundary conditions[23,37–41]. Van der Giessen et al. investigated how different outflow boundary conditions affect computed WSS values, but could not incorporate patient-specific measurements to compare their results[20]. Alternatively, Molony et al. studied the effect of imposing patient-specific or scaled inflow boundary conditions on computed WSS[42]. In a previous study we investigated the effect of only scaled outflow conditions on WSS computations at hyperemic conditions[27]. In our current study patient-specific measurements were available for both the inlet and outlet boundary conditions. The studies by Van der Giessen et al. and Molony et al. showed that the difference between measured and scaled boundary conditions can give rise to large difference in absolute WSS. In our study this was particularly striking at focal spots of high WSS, but areas exposed to decreased WSS can be misinterpreted as well, which could frustrate the search for a correlation between absolute WSS and an atherosclerotic marker[43]. On these grounds geometric scaling does not seem to be appropriate to accurately determine absolute WSS values in mildly diseased coronary bifurcations. In the point to point comparison a considerable difference was shown, and although the axial and circumferential averaging led to smaller differences, they were not negligible as shown by the noninferiority test.

The normalized WSS on the other hand was unaffected by the difference between the measured and scaled boundary conditions. It has been hypothesized that, instead of absolute WSS levels, the endothelium is sensitive to deviations from normal WSS values at baseline flow[44]. These deviations from the baseline WSS values might thus be a potential marker for the onset and progression of atherosclerosis and could be detected with normalized WSS maps. For instance, in a study by Gijsen et al. normalized WSS levels were correlated to strain levels within plaques[8]. The highest strains were found in regions exposed to high normalized WSS, which suggests that high WSS might be associated with plaque destabilization. The study by Eshtehardi et al. found a relation between lowest

25% of WSS and plaque phenotype development[45]. Our study showed that normalized WSS proved to be a robust measure, even in cases where the differences in outflow ratio were relatively large. This was found also by Marzo et al. for cerebral aneurysms, but only qualitative results for normalized WSS were reported[46]. In our study the 2D maps and the averaged values of normalized WSS were not influenced by the boundary conditions. This implies that, despite the non-linear nature of flow phenomena, the flow in these cases was within a range that normalization still yielded similar results. This means that it would be possible to compute normalized WSS distributions from angiography data alone without the need for intravascular velocity measurements.

The hemodynamic significance of coronary stenosis can be determined with FRR, which is derived at hyperemic conditions. Several studies focused on computing FFR to replace invasive measurements[47,48]. In a previous report we investigated the influence of scaled outflow conditions on the pressure drop and FFR at hyperemia. That study showed that the FFR was uninfluenced by the variation in outflow ratio. However, the absolute inflow is expected to have a greater effect on the overall pressure drop than the outflow ratio. Therefore the variations in inflow conditions could consequently influence the computed FFR. In this study baseline conditions were evaluated only, and in a subsequent study it would be interesting to investigate how scaled inflow affects FFR.

Limitations

For this study only a small number of patients was selected. Future studies in larger patient populations should confirm that diameter-based scaling laws in combination with angiography images are sufficient to determine normalized WSS distribution. Subsequently, it would be interesting to include patients in a later stage of the disease that suffer from lumen intruding plaques.

For the geometry reconstruction elliptical cross-sections derived from two angiography images were used. Although this resulted in representative geometries, improvements can be made to acquire a more precise representation, by for instance using intravascular imaging. The goal of this study was to compare the influence of different

Figure supplements → Overview of results for one case similar as Fig. 4. Again the inflow was underestimated by the scaled-approach, but in this case also the outflow ratio differed substantially. **A:** A 3D reconstruction of the geometry with color map indicating the WSS computed with measured boundary conditions (BC). **B:** 2D maps of the computed absolute WSS with the two approaches. The maps of the mother branch and the daughter where the flow was measured are plotted. **C:** The circumferential average of the absolute WSS in the two segments for the measured-approach (blue circles) and scaled-approach (pink diamonds). **D:** Axial average in the mother branch of both methods. **E:** Axial average of the daughter. **F:** Normalized 2D WSS maps computed with the two methods. **G:** The circumferential averages of the normalized WSS in the mother branch. **H:** Axial average of the normalized WSS in the mother branch. **I:** Axial average of the normalized WSS in the daughter branch
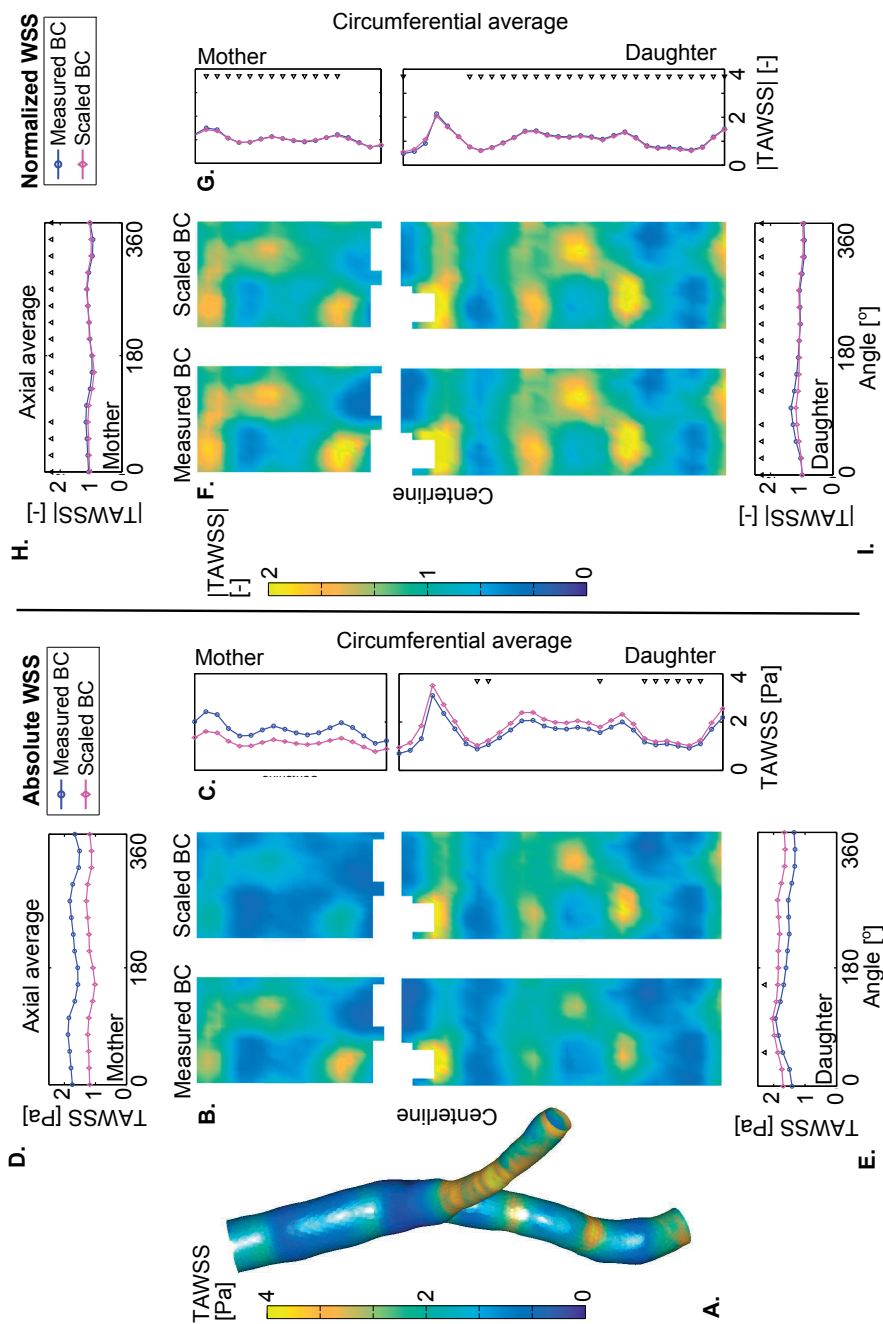
Figure supplements

boundary conditions. Since the same geometry was used to compute WSS with two different sets of boundary conditions, the use of angiography-based reconstructions should not have affected the findings of this study.

The locations where the diameters were measured were selected by a trained reader. Nonetheless, Valen-Sendstad et al. showed that this choice can influence the computed absolute WSS[49]. Based on angiography alone it remains difficult to select a healthy and representative section that can be used for the geometric scaling laws. The normalized WSS will probably be more robust to the small deviations in diameters for the scaling law.

Finally other parameters besides WSS are associated with atherosclerosis, such as the oscillatory shear index or the relative residence time, which depend on transient flow computations[50]. Although the diameter-based outflow models proved effective in this study, more advanced outflow models are likely to be better suited for the transient computation.

Conclusion

In conclusion, normalized WSS was shown to be unaffected by the variation in boundary conditions when obtained from either from measurements or by applying diameter-based scaling laws. Caution should be taken when absolute WSS values are assessed from computations based on scaled boundary conditions.
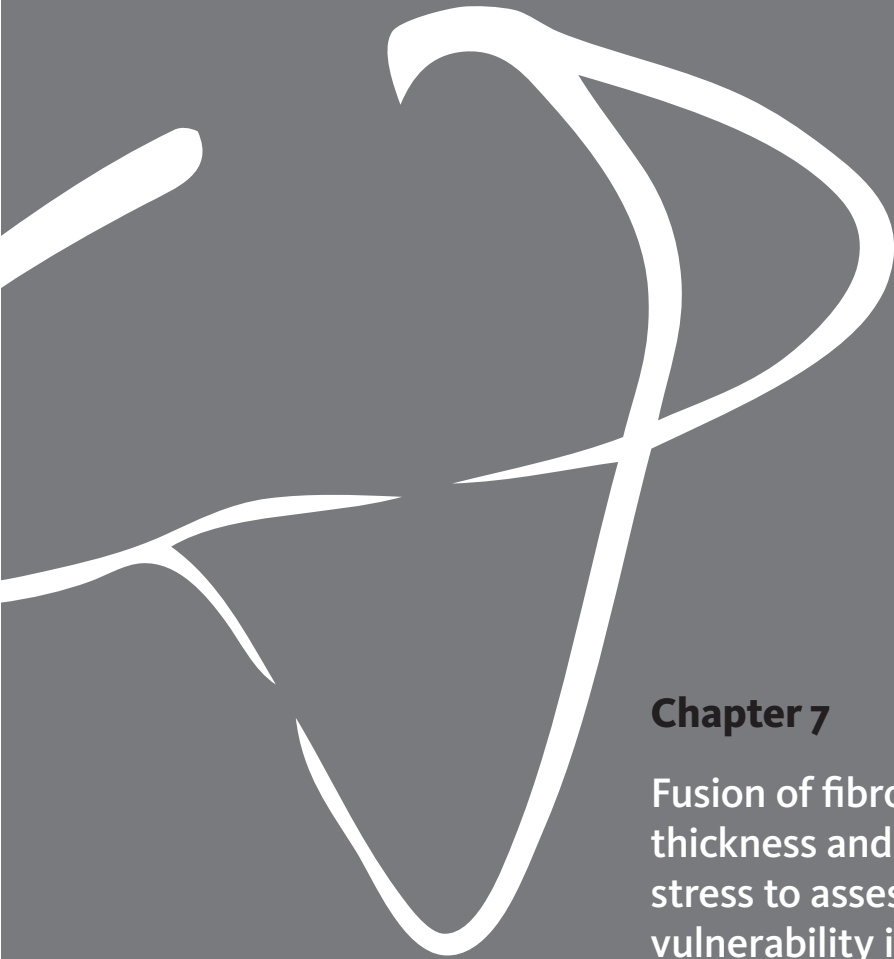
Chapter 7

Fusion of fibrous cap thickness and wall shear stress to assess plaque vulnerability in coronary arteries: A pilot study

ABSTRACT

Identification of rupture-prone plaques in coronary arteries is a major clinical challenge. Fibrous cap thickness and wall shear stress are two relevant image-based risk factors, but these two parameters are generally computed and analyzed separately. Accordingly, combining these two parameters can potentially improve the identification of at-risk regions. Therefore, the purpose of this study is to investigate the feasibility of the fusion of wall shear stress and fibrous cap thickness of coronary arteries in patient data.

Fourteen patients were included in this pilot study. Imaging of the coronary arteries was performed with optical coherence tomography and with angiography. Fibrous cap thickness was automatically quantified from optical coherence tomography pullbacks using a contour segmentation approach based on fast marching. Wall shear stress was computed by applying computational fluid dynamics on the 3D volume reconstructed from two angiograms. The two parameters then were co-registered using anatomical landmarks such as sidebranches.

The two image modalities were successfully co-registered, with a mean (±SD) error corresponding to 8.6±6.7% of the length of the analyzed region. For all the analyzed participants, the average thinnest portion of each fibrous cap was 129±69 µm, and the average WSS value at the location of the fibrous cap was 1.46±1.16 Pa. A unique index was finally generated for each patient via the fusion of fibrous cap thickness and wall shear stress measurements, to translate all the measured parameters into a single risk map.

The introduced risk map integrates two complementary parameters and has potential to provide valuable information about plaque vulnerability.

INTRODUCTION

Cardiovascular disease is the leading cause of mortality and morbidity worldwide[1]. Acute myocardial infarction is generally triggered by rupture of so-called vulnerable atherosclerotic plaques in the coronary artery[2–4]. Such rupture-prone plaques are often referred to as 'silent killers', since symptoms remain unnoticed until the event. Therefore, identification of vulnerable plaques is of eminent importance and represents a major clinical challenge[5].

The morphological characteristics of rupture-prone plaques are a large lipid necrotic core, an overlying thin fibrous cap, and dense macrophage infiltration. These vulnerable plaques are also known as thin-cap fibroatheromas (TCFAs), and are considered the precursor phenotype of plaque rupture[6,7]. Fibrous cap thickness is a critical component of plaque stability, namely thinner caps being more prone to rupture than thicker caps[8]. The threshold of 151μm was recently demonstrated to be the best cut-off to predict rupture for most representative fibrous caps[9]. Therefore, *in vivo* quantification of fibrous cap thickness could enable identification of vulnerable plaques, and potentially guide appropriate surgical treatments such as percutaneous coronary intervention prior to the occurrence of an event.

Moreover, complementary parameters to assess plaque vulnerability can be derived from information about local hemodynamics. Wall shear stress (WSS) is the frictional force of the blood at the vessel wall, and plays an important role in the development and progression of atherosclerotic plaques[10]. Evidence is accumulating that elevated WSS influences plaque composition in such a way that it induces local weakening of the plaque[11,12], and that plaque rupture often occurs upstream to regions exposed to elevated WSS levels[8,13]. Accordingly, combining WSS computations to cap thickness measurements would constitute a risk index that is likely to improve the identification of vulnerable plaques in coronary arteries.

Fibrous cap thickness can be quantified accurately *in vivo* with intravascular optical coherence tomography (OCT)[14]. OCT is an emerging catheter-based imaging modality that enables tissues to be visualized *in vivo* at a high spatial resolution (10-20 μm) and in a minimally invasive fashion. Investigation of the inner circumference of the vessel is performed by the probe spinning along its axis while being pulled back. The emission and reception of near-infrared light at each angular step yields the acquisition of so called A-lines, whose echo time and intensity are then converted into a single gray-scale image. During the pullback acquisition, a stack of consecutive cross-sectional images is generated along the length of the assessed artery segment. The very high spatial resolution of OCT enables an accurate characterization of the structure of the most superficial layers of the arterial wall and can indicate the degree of subclinical atherosclerotic lesion formation[15].

WSS can be obtained by computing the flow field inside of the coronary artery using computations fluid dynamics (CFD). To quantify the WSS, the derivative of the computed flow field near the surface of the wall is calculated. To perform such computation, the three-dimensional (3D) of the arterial lumen geometry is required. Previous work showed that 3D arterial geometry can be accurately reconstructed from two angiography images planes, i.e. at two different angles[16,17]. These reconstructions have then successfully been used to compute WSS in coronary arteries in several recent studies[18–20].

Co-registration of several imaging modalities to improve plaque analysis has been investigated in previous studies. A method for accurate side branch modeling using angiography and OCT was proposed in a recent work[21]. In another study, WSS was computed from volumetric reconstructions generated from 3D OCT, and compared with corresponding geometries derived from 3D intravascular ultrasound (IVUS) and 3D angiography[20]. The effect of inflow boundary conditions on WSS was also investigated using IVUS and angiography[22]. The relationship between WSS and plaque characteristics was assessed using a different approach with OCT and angiography[23]. Nevertheless, the fusion of WSS and cap thickness has not been addressed yet, and the clinical relevance of the resulting index corresponding to the fusion of these two parameters has not been investigated.

The aim of this study is to propose a novel tool devised to evaluate the risk of plaque rupture in clinical settings, by exploiting the fusion of *in vivo* OCT and angiography imaging. A methodology is proposed for a combined assessment of fibrous cap thickness and WSS information. Fibrous cap thickness is quantified from OCT images using a previously validated method that was developed in-house[24]. Wall shear stress is computed based on angiography data by exploiting a recently proposed method[19]. A co-registration framework devised to accurately align and fuse the two measured parameters is presented. The main contribution of this work is a unique index that is derived from co-registered parameters, and displayed as a single risk map aiming to improve the identification of high-risk regions in coronary arteries. To evaluate the feasibility of the proposed framework, a proof-of-concept validation is carried out on 14 patients.

METHODS

Study population
Data was gathered at the Thoraxenter, Erasmus MC (Rotterdam, The Netherlands). Fourteen patients (mean age 61.0±10.3 years old, 7 males), suffering from coronary artery disease and referred for possible percutaneous coronary intervention, were involved in

the study. Ten left anterior descending arteries, one left main artery, and 3 right coronary arteries were simultaneously imaged with angiography and OCT. Informed consent was acquired from the patients for use of their imaging data. All procedures followed were in accordance with the ethical standards of the responsible committee on human experimentation (institutional and national) and with the Helsinki Declaration of 1975, as revised in 2008.

Data acquisition

Angiography recordings were acquired at a frame rate of 15 frames/s with the Axiom ArtisTM system (Siemens, Forchheim, Germany). The two recording angles were selected to avoid overlap of branches other than the selected coronary artery. Table movement in between the two recordings was avoided as well. The ECG signal was registered during the recordings. The angiography images were sampled at 1024x1024 pixels.

OCT imaging was realized with three different scanners, to assess the applicability of the framework. Pullbacks were acquired using one of the following apparatus1) Illumien frequency-domain imaging system with the Dragonfly Duo intracoronary imaging catheter (Lightlab/St Jude, Minneapolis, MN, USA) (9 patients), 2) Lunawave system with the Fastview imaging catheter (Terumo Corporation, Tokyo, Japan) (2 patients), or 3) MGH prototype optical frequency domain imaging system (Massachusetts General Hospital, Boston, MA, USA), and the Terumo Fastview catheter (3 patients). Image acquisition was performed with a previously described non-occlusive technique[15]. For the Lightlab system, pullbacks were acquired over a total length of either 54 mm (6 patients) or 75 mm (3 patients) along the vessel, at either 105 frames/s or 180 frames/s, with an inter-frame distance of either 200 μm or 100 μm. For the Terumo system, pullbacks were acquired over a total length of 47 mm, at 160 frames/s, with an inter-frame distance of 125 μm. For the MGH system, pullbacks were acquired over a total length of 61 mm, 81 mm, and 121 mm along the vessel, at 100 frames/s, with an inter-frame distance of 200 μm. The spatial resolution was 20 μm and 30 μm in the axial and lateral directions, respectively. The depth of the scan range was 4.3 mm. Acquired images were sampled at 968x504 pixels.

Quantification of fibrous cap thickness from OCT images

Fibrous cap thickness is quantified using a previously validated framework[24]. This semi-automated approach consists in a robust contour segmentation scheme based on the fast marching methodology[25]. Briefly, a cost function is derived from the intensity gradient of the polar OCT image along the radial direction. A front propagation scheme is then run, favoring low cost points (i.e. data-attachment term) while penalizing radial displacements (i.e. smoothness constraint term). The optimal path, corresponding to the segmentation contour, is finally extracted by means of a back-tracking scheme in the propagated values.

The three principal phases of the framework are *i)* a manual selection of the region of interest (ROI) containing the fibrous cap to be analyzed; *ii)* the automatic extraction of the luminal interface over the entire vessel circumference; and *iii)* the automatic extraction of the abluminal interface of the fibrous cap within the ROI. Fibrous cap thickness is finally calculated as the distance between both contours of the cap, along a set of lines perpendicular to the luminal interface.

Computation of wall shear stress from angiography images

To compute WSS, the lumen of a coronary artery was first reconstructed based on two angiography images, following the method previously adopted in Goubergrits et al.[19]. These two angiography images were recorded with angular difference of at least 30° and were selected in the same cardiac phase, as indicated with the ECG information. The contrast-filled lumens in the 2D images were segmented by a trained observer (JS). From the 2D segmented contours, a 3D volume was generated, using validated commercially available software (CAAS v5.11, Pie Medical Imaging, Maastricht, the Netherlands)[17]. Next, based on the volume of the lumens, a mesh was generated to compute WSS. The volume meshes were built with tetrahedral cells of approximately 0.1 mm and a five element prism layer at the wall, resulting in a mesh size of typically $2 \cdot 10^6$ cells.

WSS was calculated with CFD using a finite volume solver and by applying standard numerical techniques (Fluent v14.5, Ansys Inc, Canonsburg, US). The inlet and outlet boundary conditions for these computations were assigned by applying scaling laws specific to human atherosclerotic coronary arteries[26]. From the results the 3D WSS magnitude at the wall was extracted and converted to a 2D coordinate system. To do so, the planes perpendicular to the centerline were defined at 0.2 mm intervals. The planes were subsequently subdivided in intervals of 10°. The average WSS values within the resulting bins were mapped to a 2D representation of the absolute WSS.

The WSS was normalized for further analysis. To this end the WSS from the 2D maps was extracted from the segment in between the side branches that served as landmarks, and normalized to the 50th percentile value of that segment.

Co-registration procedure of OCT with angiography

Fusion of OCT and angiography was performed manually using a previously proposed approach[27]. The matching procedure involves two main steps, namely axial and rotational registration (Fig. 1). Axial registration consists in aligning the length and position of a given arterial segment of the OCT pullback with the corresponding segment in the 3D-reconstructed vessel. Rotational registration is the task to determine the angular transformation so that the two segments have the same orientation and overlap with each other. These two steps are described below.
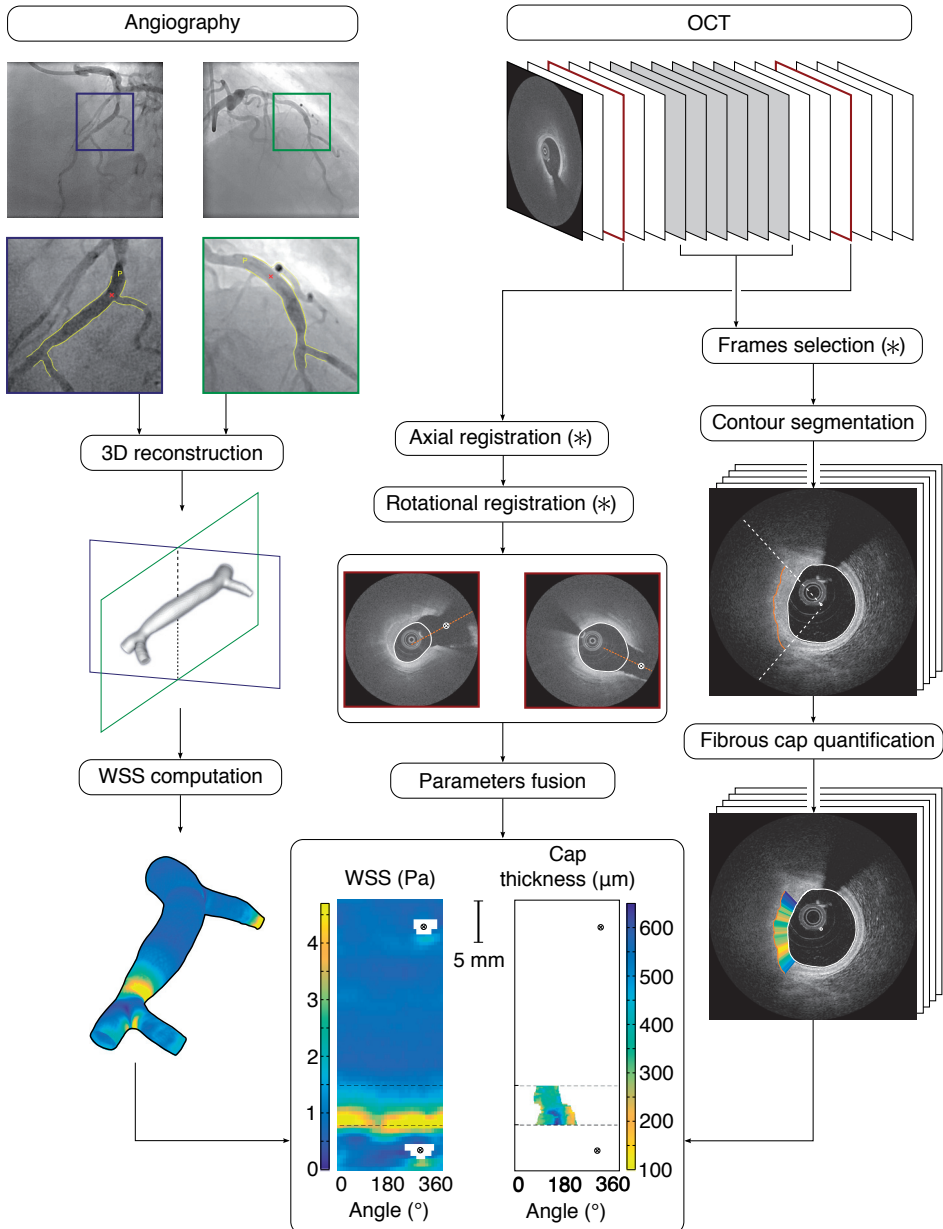
Fig. 1: General framework of the method. All steps of the method are (semi-) automatic, except those indicated with an asterisk (*).

Axial registration

The OCT catheter was visible in at least one of the two angiography images, and indicated the starting and ending points of the OCT pullback. Additional landmarks such as bifurcations and lumen narrowing were identified in both OCT and angiography images. To correctly identify the landmarks, their size as well as the distance between them, were used as additional information. Registration was performed by matching similar pairs of landmarks between the two imaging modalities.

Rotational registration

To determine the angular shift between the OCT images and the 3D volume, the orientation of two side branches was used. Information related to angles was extracted from the cut-open map corresponding to the WSS derived from the 3D reconstruction. In this map, the position of the side branches was indicated. The corresponding positions were also indicated in the OCT pullback. Next, the entire OCT pullback was uniformly rotated around the lumen centerline in order to match the orientation between the two distal side branches. Subsequently, a linear and gradual rotation was applied to the entire pullback in such way that the two proximal side branches had the same orientation, while conserving the alignment between the two distal side branches.

Parameter fusion

To visually display the risk index of the interrogated region on a single map, fusion of cap thickness and WSS was finally performed after the co-registration of OCT and angiograms. Recent findings demonstrated that the best cut-off to predict rupture was 151 μm for most representative fibrous caps[9]. Therefore, this value was used as an upper threshold to identify at-risk regions based on cap thickness information. Similarly, 1.7 Pa is often used to represent the transition between intermediate and high WSS[28], and this value was selected as a lower threshold to characterize at-risk regions based on WSS information. The different risk levels, determined from fusion of cap thickness and wall shear stress, are presented in Table 1.

Risk	Cap thickness [μm]	Wall shear stress [Pa]
Low	>151	< 1.7
Medium	>151	≥ 1.7
Medium	≤ 151	< 1.7
High	≤ 151	≥ 1.7

Table 1: Risk index

RESULTS

Co-registration of OCT and angiography

For each included patient, one site corresponding to an atherosclerotic plaque covered by a fibrous cap could be identified in the OCT pullback, and subsequently localized in the two corresponding angiograms. Volumetric reconstruction from angiography could not be performed for two cases, due to insufficient image quality of the side branches that were used as landmarks (i.e. presence of a trifurcation with vessels overlapping with each other in the image plane for the first case, and contours poorly visible with high level of noise for the second case). These two patients were rejected from the study, and the framework was applied on the 12 remaining cases.

Volumetric 3D geometries were reconstructed with two angiography views corresponding to the same cardiac cycle, based on the recorded ECG. Ten cases were reconstructed in diastole. The two remaining cases were reconstructed in systole, since over-projection of the side branches did not allow the diastolic phase. Nevertheless, only a rigid transformation of the ROI was observed by the trained reader (JS) between the diastolic and systolic phases.

Cap thickness and WSS were computed using the methods detailed in Sections 2.3 and 2.4. Co-registration between OCT and angiography was then successfully performed for all cases. Results displaying the co-registration of WSS and cap thickness are presented in Fig. 4, and identification of at-risk regions was finally realized *via* the fusion of these two parameters in a single map.

To quantify the accuracy of the co-registration procedure, the length between the proximal and distal side branches that were used as landmarks (Fig. 1) was measured along the vessel centerline, in both the angiography-derived 3D volume and the OCT pullback. The average length (±SD) between the two side branches was 19.0±11.1 mm
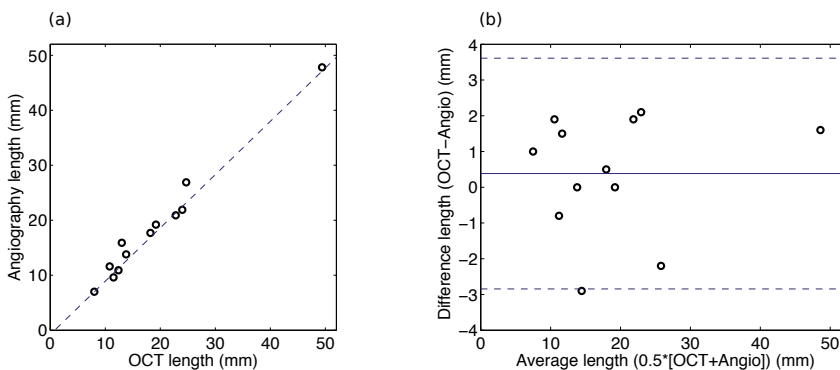
Fig. 2: Length validation between the proximal and distal side branches used for the co-registration between OCT and angiography, for the 12 processed cases. **A**: Linear regression line. **B**: Bland-Altman plot.
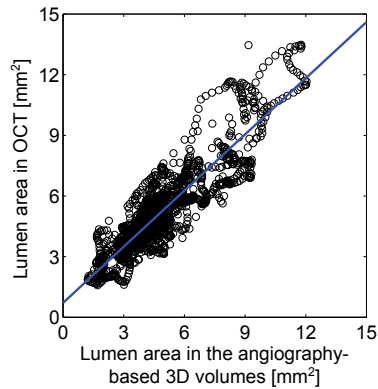
Fig. 3: Linear regression line between the lumen area derived from angiography and from OCT, for all 12 processed cases.

in OCT, and 18.6±10.8 mm in angiography. Regression analysis demonstrated a strong linear relationship between the length derived from the two modalities with r=0.99, as depicted in Fig. 2. The mean absolute difference between the distance measured in OCT and angiography was 1.4±0.9 mm, corresponding to 8.6±6.7% of the measured length, with a bias of 0.4 mm and a 95% confidence interval of [-2.8, 3.6] mm.

Additionally, for the 12 analyzed patients, the lumen area of the arterial segment was measured in each OCT frame between the two landmark side branches, and compared with the lumen area measured at the corresponding location in the 3D volume derived from angiography. A good correlation (R = 0.89) was found between the two set of measurements, as displayed in Fig. 3.

Fibrous cap thickness and WSS analysis

For the 12 analyzed patients, the average cap thickness (±SD) was 278±119 μm, and the thinnest portion of each cap was 129±69 μm. Along the z-axis of the OCT pullback, the average length of the region encompassing the analyzed fibrous cap was 4.5±2.4 mm, corresponding to an average of 33±19 frames. Along the circumference of the vessel, the average angle of the ROI encompassing the cap was 140±58°.

Fig. 4 → : Result examples. **A:** Two angiograms. The region of interest (ROI) is indicated with the rectangle. **B:** OCT image. The fibrous cap is indicated with the asterisk. **C:** 3D reconstruction of the ROI. **D:** WSS map. The region corresponding to the necrotic core is indicated by the dashed lines and the violet contours. **E:** Necrotic core regions. Top row: WSS map (magnified). Middle row: co-registered cap thickness map. Bottom row: corresponding risk index. Patient 1: thin fibrous cap (yellow) with localized high WSS (blue), defining a high-risk region (red). Patient 2: low to medium WSS with relatively thick fibrous cap. Patient 3: thin cap with low WSS. Patient 4: medium WSS with relatively thick fibrous cap.

(a)　　**(b)**　　**(c)**　　**(d)**　　**(e)**

WSS (Pa)
0　0.7　1.4　2.1　2.8　3.5

Cap thickness (µm)
100　200　300　400　500

10 mm

Cap thickness (µm)	>151	>151	≤151	≤151
WSS (Pa)	<1.7	≥1.7	<1.7	≥1.7
Risk	Low	Medium	Medium	High
Color-code	None	WSS	Cap	Both
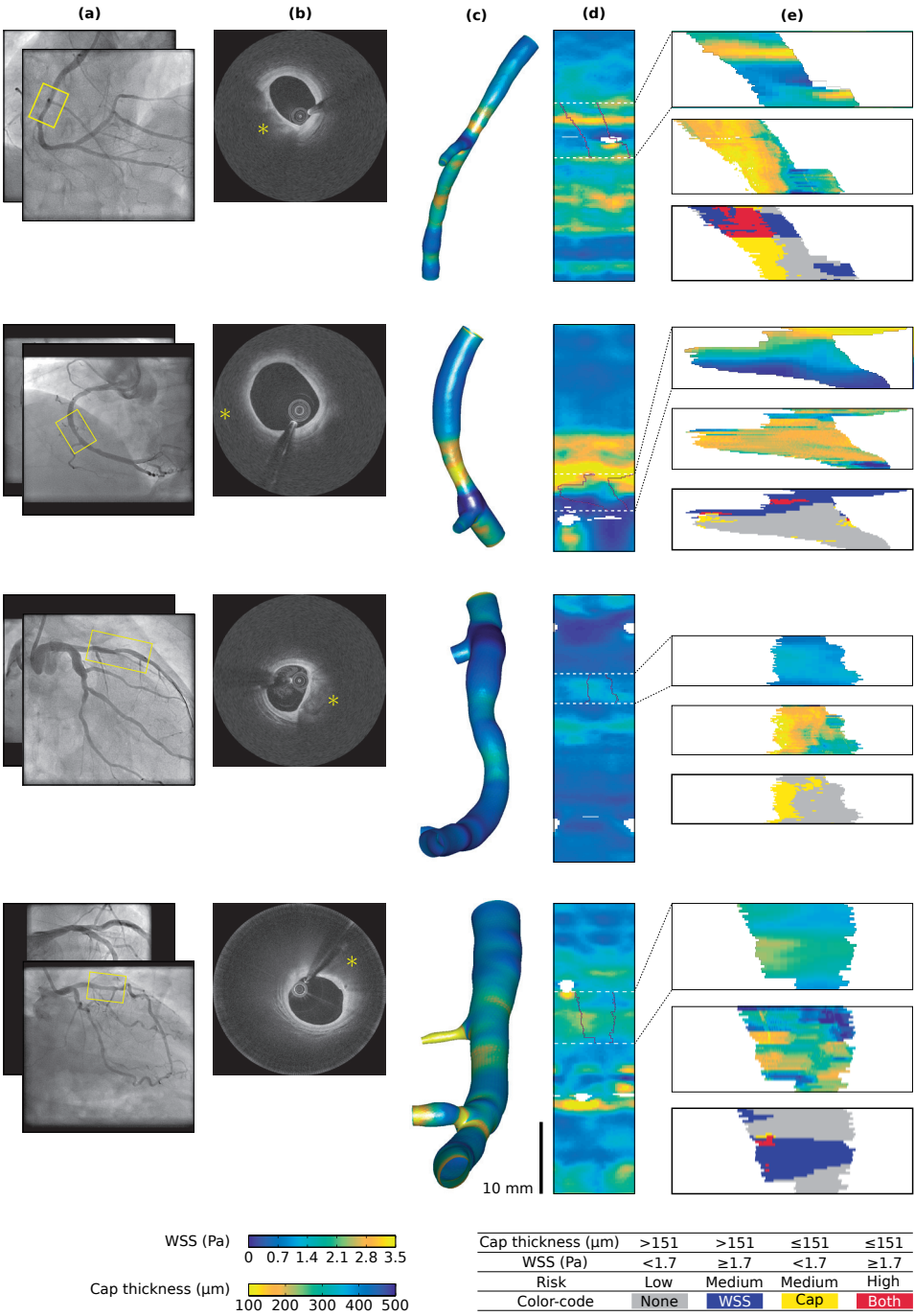
Fig. 4

The average WSS value at the location of the fibrous cap was 1.46±1.16 Pa. Such magnitude is typically considered as a medium WSS value. However, when normalizing the WSS within the region between the two side branches used for the co-registration, the WSS value at the location of the fibrous cap was superior than 1, namely 1.58±1.12. Only one case had a relatively lower WSS within at the ROI, with a normalized value of 0.59±0.13. This demonstrates that, in all cases but one, the highest stress values also corresponded to the location of the cap.

No direct association between WSS and cap thickness was observed. For the 12 analyzed patients, the average composition of the risk map was the following: 35% of the total region corresponded to a high WSS (i.e. ≥1.7 Pa, medium risk), 5% to a thin cap (i.e. ≤151 μm, medium risk), 2% to both of these two factors combined (i.e. high risk), and 58% to none of them (i.e. low risk). For three patients, more than 80% of the plaque region was under high WSS levels. For two other patients, a thin cap covered more 20% of the total plaque area plaque. For another patient, both of these two factors were present in an area equal to 15% of the plaque.

DISCUSSION

In this pilot study, two image-based parameters (i.e. fibrous cap thickness and WSS) derived from two different image modalities (i.e. OCT and angiography) were assessed in the coronary artery and subsequently co-registered. OCT imaging enables arterial tissues to be visualized *in vivo* at a near-histology resolution, and can detect high-risk morphologies such as thin cap fibroatheromas. Angiography can provide 3D information about arterial geometry, local hemodynamics, as well as WSS, thus potentially enabling complementary parameters to assess the rupture risk of a certain plaque. The principal contribution of this work is the introduction of a unique risk map that integrates complementary information derived from cap thickness and WSS parameters.

Co-registration of fibrous cap-thickness and WSS

Proof-of-concept results were obtained by processing 12 coronary segments imaged from 12 *in vivo* patients. An atherosclerotic plaque covered by a fibrous cap was identified in all OCT pullbacks. In all cases, the computed WSS was within the expected physiological range, with elevated WSS at stenosed location. Co-registration between OCT and angiography was performed using two side branches as anatomical landmarks. The accuracy of the co-registration method was validated by the high agreement between the corresponding lengths of the co-registered segments.

The 12 patients analyzed in this study had a fibrous cap of intermediate thickness (i.e. 278±119 μm). Nevertheless, the average value at the thinnest point of the cap was

129±69 μm, which is inferior to the lower threshold of 151 μm used to characterize at-risk regions. It is expected that a broader range of cap thickness, including caps thinner than 65 μm, would be observed by including additional patients in the study. The method to quantify cap thickness was developed in house and previously validated[24]. The clinical applicability of the proposed method is supported by a relatively accurate quantification of cap thickness, with a mean absolute error (±SD) of 30±37 μm.

The association between coronary WSS levels and various atherosclerosis markers was investigated in several studies[20,23,28]. Nevertheless, these studies do not include the side branches in their 3D reconstruction framework when computing the WSS. Although such approaches simplifies the modeling procedure, the presence -or absence- of side branches critically influences the resulting the flow phenomena near bifurcations, as demonstrated in a recent study[21]. The computed flow field in a straight segment directly in between two side branches is not likely to result in adequate WSS patterns, especially at the proximal and distal ends. Moreover, bifurcated areas also correspond to predilection sites for atherosclerosis development, thus making accurate computation in these areas particularly pressing. In the present study, special care has been taken to incorporate both proximal and distal side branches in the CFD computation in order to provide reliable WSS levels.

A unique and patient-specific risk-index map (Fig. 4e) could successfully be generated for all cases. This tool translates all the measured parameters into a single visual information for interpretation of the results. The proposed risk-index map enables fast, simple and reliable identification of at-risk lesions. Such approach has potential to provide a useful aid for interventional planning and decision making.

Clinical implications

Both angiography and OCT imaging provide valuable information to evaluate the patient, namely WSS and cap-thickness. No clear relationship was found between extreme WSS values and cap thickness, therefore the two parameters are likely not to be redundant but instead complementary. The underlying concept of atherosclerosis is complex, and new approaches are required to better assess the risk of the patient.

In this study, threshold values are used to define the risk index from cap thickness measurements and WSS computations. Regarding fibrous cap thickness, the threshold of 65 μm is widely adopted to identify high risk lesions[29]. Nevertheless, this empirical value is likely to be under-evaluated, since *ex vivo* tissues usually undergo variable shrinkage rate during histological preparation[6,15]. A different study established that ruptured plaques in acute coronary syndrome are often associated with a fibrous cap thickness of up to 100 μm[30]. In the present work, the 151 μm threshold value was adopted, as it has been demonstrated to be the best cut-off to predict plaque rupture for most representative

fibrous caps[9]. As for WSS, a consensus in the literature uniformly associates values lower that 1.0 Pa to low WSS levels[10,12]. Nevertheless, there is still an ongoing debate about the absolute WSS levels used to categorize the high WSS profiles. A first study showed that patho-biological processes started destabilizing the cap above 1.5 Pa[31]. A different team used a cut-off value of 2.5 Pa, and reported that this level is associated with a transition into a phenotype of vulnerable plaque[12]. Another study analyzed regions where the WSS levels were above 4.0 Pa, and observed that these regions corresponded to areas with larger necrotic core and higher plaque burden[32]. In the present work, we adopt the threshold value of 1.7 Pa. This choice was motivated by the fact that it was proposed as the optimal threshold between moderate and high WSS in the largest cohort study to date that that investigated atherosclerotic disease progression and localized WSS values[28]. Nevertheless, critical WSS levels need to be further evaluated to reach consensus and determine actual clinically relevant values. The novel risk index introduced in the present study can potentially contribute to re-establish relevant WSS values.

The risk-map could also be composed with normalized WSS instead of absolute WSS. Previous studies indicate that normalized WSS might be a robust method to deal with inaccuracies or inconsistencies that can arise from geometry reconstruction procedures or a chosen methodology to set the boundary conditions[22,26]. The normalized WSS results from this study show that the fibrous cap was exposed to elevated WSS levels. This is in accordance with the theory that thin caps and high WSS co-locate[11,31,33].

The clinical significance of this study is also supported by previous work that combined OCT and angiography imaging, and reported that coronary regions exposed to low WSS were associated with larger lipid burden, thinner fibrous cap, and higher prevalence of thin-cap fibroatheroma[23]. Nevertheless, no association was found between peak WSS and low cap thickness in the present study. However, the number of patients involved in this study is relatively limited. Furthermore, results only represent a snapshot in time from which the current values of cap thickness and WSS can be quantified, therefore the clinical interpretation is limited. Atherosclerosis is a process that develops over time and follows a complex evolution[34]. The different manifestations of the syndrome on the arterial wall, such as plaque composition, morphological alteration, flow patterns, and WSS, also undergo a progressive variation of which the rate may greatly vary from one case to another. A follow-up study would be required to assess the state of the necrotic core plaque over time, better characterize the evolution of the atherosclerotic process, and assess the added value of the two combined parameters for clinical decision making.

Limitations

The 3D volume was generated using a pair of angiography images at two different angles. In such procedure, the cross-sectional lumen geometry was approximated

to an elliptic shape. Nevertheless, this assumption had a limited effect on the lumen area, as indicated by the good correlation between the actual lumen area quantified in OCT and the approximated measurements derived from angiography (R = 0.89, Fig. 3). Another limitation lies in the fact that, although the 3D reconstruction of the vessel was performed using two angiography views in an identical cardiac phase, the OCT-derived information was acquired all along the cardiac cycle and did not systematically match the same cardiac phase. Accordingly, spatial shift could have been introduced between the parameters derived from angiography and OCT. The change in curvature of the artery is likely to induce, up to a certain extent, different WSS values during the cardiac cycle. Additionally, the thickness of the cap may also undergo some variation due to the mechanical forces compressing the tissues. This issue could be addressed with an ECG-triggered acquisition of the OCT pullback, in such a way that the ROI is imaged during the diastolic phase to match the angiography information. Finally, in this pilot study, all the (semi-) automatic steps of the framework (Fig. 1) are currently processed offline. The implementation of the method can be optimized by running the code on a Graphics Processing Unit, thus resulting in faster computations (i.e. below one minute) and enabling online utilization of the tool directly in the catheterization laboratory.

Conclusion

Two risk factors are assessed in the coronary artery using two different imaging modalities, namely fibrous cap thickness is derived from OCT, and WSS is computed from angiography. These two parameters are complementary as they provide information about plaque geometry and hemodynamics, respectively. The generation of a unique risk index is enabled by co-registration of the two risk markers using anatomical landmarks such as side branches. The proposed framework is a promising approach for online identification of plaque vulnerability in the intervention room.

Chapter 8

Discussion

Acute myocardial infarction is generally triggered by rupture of so-called vulnerable plaques in the coronary arteries[1–4]. WSS is a known to play a pivotal role in the onset of atherosclerosis and the progression to a more vulnerable plaque type[5–7]. WSS in the coronary arteries cannot directly be measured, but it can be obtained with CFD. The work in this thesis focused on computing WSS in mildly diseased coronary arteries. In particular the challenges were investigated that arise when WSS will be introduced into clinical practice. In last decades many techniques were developed that could be used to compute WSS[8]. These techniques often relied on elaborate reconstruction methodologies and required input data that has to be obtained through additional invasive measurements, e.g. intravascular imaging or intravascular measurements of hemodynamic parameters. Angiography on the other hand is widely available since it plays a crucial role in definitely confirming an ACS diagnosis. Recent development in image reconstructions techniques have led to tools that allow online 3D reconstructions based on angiography data[9–11]. If also the boundary conditions can be estimated from geometry, WSS can be assessed by relying solely on angiography. This could create possibilities for online clinical applications of WSS. Besides WSS the rupture-risk of a plaque is determined by the thickness of the cap that separates a necrotic core from the lumen[12]. A combination of WSS with a second image-based parameter that characterizes plaque morphology would further aid the identification of plaque vulnerability.

   The first chapter of this thesis focused on the influence the limited resolution angiography offers in the context of accuracy of the WSS computations. Next, two methods are presented that use the geometry from angiographic data to estimate the pressure drop. In combination with CFD the pressure-drop estimate could improve the accuracy and efficiency of the computations. A more direct approach is to impose boundary conditions based on scaling laws that are set using geometry data obtained with angiography. The impact of angiography-based boundary conditions proved to have considerable influence on absolute WSS results, but normalized WSS showed little sensitivity in this regard. In the last chapter a novel risk-map is introduced. Two complementary imaged-based parameters that are associated with plaque vulnerability were extracted from angiography and OCT data. These two parameters, cap-thickness and WSS, were combined into one risk-map, which directly visualizes plaques at risk.

Geometry reconstruction

The quality of the CFD results critically depends on the accuracy of the geometry reconstruction. The geometry is important for the computations since WSS is a derivative of the flow field near the wall. With the back-of-the-envelope calculation given in chapter 2 it is easily shown that even in an idealized straight segment the error increases with a third power with respect to deviations to the reconstructed diameter. Taken into account the resolution obtained using typical settings for angiography and the range of dimen-

sions of human coronary arteries the deviations can quickly become considerable. In a coronary artery with a radius of for example 1.25 mm and an angiography system with a resolution of 0.1 mm, the relative error is in the range of ±25%. In a stenosed region with a radius of 0.75 mm this error can increase to ±50%.

The impact of reconstruction on computed WSS was studied by comparing it to the computed WSS in known geometries. Angiographic recordings of four phantom models were segmented by two expert readers, from which 3D reconstructions were generated. In this study models with a stenoses degrees of 60% were used, which resulted in strong jet formation and recirculation directly distal of the stenosis. Both in the healthy sections as well as in the more difficult diseased zones qualitatively comparable and representative WSS patterns were obtained. This implies that areas exposed to altered WSS patterns can be identified with CFD. The quantitative comparison revealed that mainly directly distal of a stenosis the WSS patterns were sensitive to geometrical deviations. This indicates that the precision of the WSS computations that can be reached with angiography-based reconstructions will not always suffices.

The study was performed under idealized circumstances, i.e. motion artifacts caused by breathing or heartbeats were excluded and optimal viewing angles were selected. By exploiting the currently available techniques to their full potential the deviations might be constrained to a certain degree for in vivo imaging. For example high frame-rate biplane imaging in combination with ECG-based frame selection could reduce motion artifacts to a minimum. With an increased frame rate up to 30 Hz and an assumed movement of 5 mm/s the reconstruction artifacts due to movement can be limited to the resolution of angiography[13]. Secondly, current angiography systems have a large degree of freedom for setting the imaging angle. This could be exploited to optimally visualize the segment of interest for 3D reconstructions. New studies could aim to adjust existing protocols to define two optimal imaging angels per segment of the coronary artery to perform 3D reconstruction techniques. It should be noted that in this study symmetrical concentric stenoses models were used. The symmetrical design resulted in an instable jet that was easily disturbed by small deviations in the 3D reconstruction. Eccentric stenoses –better mimicking the in vivo situation– might be better for these kinds of studies.

To optimally capture the 3D geometry of a diseased coronary artery fusion of angiography with intravascular imaging techniques could provide an outcome. So far hybrid imaging techniques have not made their way into routine clinical use yet. Bourantas et al. pointed out that to date the fusion procedures are time consuming and required special training[8]. In addition, the imaging data from one pullback does not provide any information about the side branches, which is especially relevant for reconstructions of coronary bifurcation. Gijsen et al. devised a method that reconstructs the global

geometry including side branches based on CTA and incorporates the intravascular data only in a region of interest[14]. But this is still a time-consuming method. A specific disadvantage of using OCT the reconstruct the arterial lumen it that it is continuously acquired throughout a heartbeat what makes the data susceptible to motion artifact of the wall. It would be interesting to find out how much deviation this causes. On the other hand, with the recently introduced OCT imaging at 5600 frames/s that study might not be necessary, since it can image a large portion a coronary artery within a heartbeat[15]. Although there are certainly hurdles to be taken before 3D hybrid imaging can performed in a clinical setting, it should be noted that many efforts are made to make the techniques user-friendly and available online[8].These developments could help incorporate hybrid imaging and 3D reconstructions into clinical practice.

Pressure-drop prediction

We investigated pressure-drop predictions in mildly diseased coronary arteries based on imaging data such that in a framework to compute WSS with CFD it could serve as a boundary condition. In chapter 3 a geometrical approach was introduced. Despite a careful selection of the relevant geometrical parameters the results showed a considerable amount of variability. The second method described in chapter 4 was based on the Navier-Stokes equations leading to a much higher accuracy. In this method the curvature was still omitted as a first step in the development.

Other investigators have studied geometry-based pressure-drop predictions as well, since it could offer a quick and easily obtained estimation. One of the first studies looked at pressure losses in a straight tube as a function of the degree of a stenosis[16]. It was found that pressure losses in an ideal stenosis are related through a quadratic function to the ratio of the diameters of the stenosis and the healthy wall. This was subsequently used by Gould et al. and Siebes et al. to predict pressure-drops from 2D angiography images with a fair accuracy[17,18]. The model presented in chapter 2 additionally includes the tapering of the vessel and its 3D curvature. The latter two characteristics are incorporated since the absence of stenoses above 50% could consequently mean that the pressure loses are significantly influenced by the two aforementioned characteristics. Regardless of the additional parameters a considerable variability was found in pressure-drop predictions. That variability could in part be attributed to the geometrical approach with limited substantiating physics.

   Therefore in chapter 4 the cylindrical formulation of the Navier-Stokes equations was taken as the starting point to estimate the pressure drop in a straightened tube with patient-specific cross sections. The resulting model was able to predict the pressure-drop with much higher accuracy than the model from chapter 3. In the model the radial component of the momentum balance was discarded. This influence of this was limited

because there were no cases with a narrowing above 50%. In more heavily stenosed cases the absent of the radial term in the momentum balance could become more influential. This was best seen in the geometry with a stenosis degree of approximately 50% where the pressure-drop was underestimated with 20% for inflow of Re=200. Future projects should aim to extrapolate this approach to a 3D description. In pilot studies a formulation in a curvilinear coordinate system was defined using the same methodology that was used for the cylindrical coordinate system. As a first step this approach could be implemented with an assumed symmetrical velocity profile. In the cylindrical formulation the definition of the velocity profile contains a parameter that relates its shape to the changing lumen profile. Also in the 3D formulation this parameter could be used to capture the effects of luminal narrowing. A next step is to develop a definition that adds asymmetry to the velocity profile by using as little parameters as possible. This parameter can be coupled to characteristics of the 3D geometry such as the local curvature, in the same way the parameter in this study was found.

Computed FFR

When pressure-drop can be predicted based on geometry, it creates possibilities to predict FFR based on geometry as well. In this case the above described models would not be used as a boundary condition, but as an independent method to predict pressure-drop and FFR. In chapter 2 this was done with a geometric approach that other investigators have pursued this as well[19]. This methodology still shows considerable variability. Alternatively, Coenen et al. used a 1D model based on a simplification of the full 3D Navier-Stokes formulation[20]. This model used the diameter along the entire coronary segment of interest. Others investigators employed CFD in 3D geometry reconstructions to calculate FFR[21,22]. The accuracy of the models was generally good with regard to the predicting a positive or negative FFR, but on a per vessel basis more deviation was seen[23]. Besides compromised image quality the results could have been limited by the modeling choices that handle the response of the myocardium.

It remains interesting to push the current limits of geometry-based FFR prediction. However, it should be noted that the principles of coronary flow reserve and subsequently FFR arose from the observations that the narrowing degree alone was not indicative for the hemodynamic impact a stenosis has with regard to myocardial ischemia. With this in mind it seems conflicting to calculate FFR based on geometry alone. The pressure-drop computation in the epicardial part might be accurate using either 3D or reduced-order models, but only if the flow is known. The resulting precision of the FFR estimate therefore greatly depends on imposing the proper flow and thus the behavior of the myocardium. The next step that could increase the accuracy of FFR prediction can be made by improving the models of the myocardial response. The results from chapter 5 show that the volume of the myocardium or the diameter of daughter branches

provide a good basis to estimate the flow distribution. The volume of the myocardium has already been incorporated in the approach by Taylor et al[24]. Future studies will have to give more insight how the myocardial response can be modeled patient specifically. Within the euHeart consortium several studies already focused optimizing coronary perfusion models with minimal invasive clinical imaging[25].

Scaling laws

In order to obtain WSS using only angiographic data, the boundary conditions need to be based on that data as well. The geometry in combination with scaling laws can be used to estimate absolute flow through one branch or the flow ratio over the multiple branches. One direct setup in which these estimates can serve as boundary conditions is by using the absolute inflow estimate and outflow ratio over multiple branches. In chapter 4 it was found that the geometry-based scaling law worked well to define the outflow ratio. In 8 out of 10 cases the difference was less than 15%. In chapter 5 both the inflow and the outflow were scaled and compared well to invasive measurements. The scaled outflow ratio proved again to be a good estimate. The scaled inflow nicely showed the same trend as the measurements, but could differ substantially on a per case basis.

The geometry-based scaling laws are derived using Murray's law, which is based on the assumption that the diameter adjusts to the flow demand of the myocardium. Van der Giessen adapted Murray's law for the blood flow in mildly diseased coronary arteries using the measurements from Doriot et al.[26,27]. In general the relationship proved to hold, but it has not been able to precisely predict the flows observed in vivo (i.e. the fitting procedure resulted in an r^2=0.7). Although the idea seems compelling that transport systems evolved such that the energy requirements are minimized, several simplifications are needed to derive Murray's law. The complex nature and function of coronary trees make it likely that such as an elementary design rule is insufficient to completely characterize the flows. This insufficiency would likely be amplified by the presence of atherosclerosis, which has dynamic and heterogeneous manifestations[28].

Better methods to define inflow will help increase the accuracy of WSS computations. Especially since absolute inflow estimates probably have a larger impact on the precision than the outflow ratios have. This is because the absolute inflow globally determines the order of magnitude of the WSS.

TIMI frame count and similar approaches that measure flow from angiography were explored in many other studies[22,29,30]. Although this technique is a straightforward solution to obtain patient-specific flows without any additional requirements, its accuracy was shown to be modest. Two main causes can be ascribed to that, namely the 3D

trajectory of the moving wave front is difficult to appreciate with 2D angiography. And secondly, the precise location of the wave front is challenging to define, due to its typically hazy appearance. In one recent study TIMI frame count measurements were used as inlet boundary conditions to compute flow, but per case the observed variability was still considerable compared to measurements[22]. A more precise inflow measure could have improved the accuracy of the study. Regardless, a qualitative assessment of WSS computed with TIMI flow can provide valuable information. Absolute WSS values based on TIMI inflow should be interpreted with caution.

When the coronary tree is imaged with angiography the pressure at the proximal end is obtained as well via the guiding catheter. Although this reveals a patient-specific parameter, the proximal pressure cannot be used in combination with an outflow ratio defined at the outlet. To improve the inflow estimation it could potentially be feasible to use the proximal pressure as input in a relative simple model, e.g. a lumped-parameter approach coupled to a single-fiber model of the heart, and extract a flow estimate from that[31]. This could improve the inflow prediction, but shifts the problem to acquiring other patient-specific parameters for such a model.

As for the outflow, the geometry-based outflow ratios worked well in the majority of the cases in chapters 5 and 6. The scaled values were directly compared to invasive and minimal invasive in vivo measurements. First, this implies that the diameter alone sufficed to get a fair assessment of the blood flow distribution in this patient population. Secondly, the agreement between the measured and scaled outflow ratios could be attributed to myocardium that is homogenously affected by atherosclerosis. This was also seen in the CTP data reported in chapter 5 where in the majority of the cases the adjoining regions had comparable myocardial perfusion rates.

In a select number of cases in chapter 5 and 6 the scaled outflow ratios deviated considerably. A first explanation could be that atherosclerosis uniformly affected the wall such that it hindered a fair measure of the diameter of a healthy section. Another explanation could be that the area corresponding to one of the side branches was possibly infarcted or diffusely affected by atherosclerosis. Regardless, in more diseased cases the geometry-based scaling of the outflow ratio could not always suffice. For future applications it is important to develop methods to identify cases where the outflow ratios have a high probability of the being disturbed. ECG for instance can give a first rough indication for the presence of infarcted areas, but a more precise discrimination of the status of the myocardium remains challenging without invasive imaging. The studies on the quantification of the myocardial blood flow with CTP could be used retrospectively to provide additional understanding needed for patient-specific modeling.

Clinical implementation of computed WSS

The work in this thesis shows that absolute WSS computations are sensitive to deviations in the geometry reconstruction and to the imposed boundary conditions. Despite these challenges many studies searched for absolute WSS values or other quantified hemodynamic parameters that could be coupled to specific wall characteristic associated with atherosclerosis[5]. These studies contributed greatly to the current understanding of atherosclerosis. Nonetheless, our results show that absolute WSS results should be interpreted with caution. For instance, a frequently used modeling choice that could influence the outcome is inflow scaled to assumed baseline conditions or based on TIMI flow measures[32–34]. Many studies computed WSS in between major side branches. By omitting the influence of side branches on the flow field, the computed WSS near bifurcation might not have been representative for the in vivo situation[35,36]. In summary, these approaches could have hindered finding absolute WSS levels in relation to atherosclerosis disease progression.

In a recent review article that gives an overview of different analyzing techniques for WSS, the authors indicate that a point-to-point analysis of WSS and wall characteristics would be an ideal[37]. The authors also point out that the required precision of the WSS map might be lacking. One alternative analysis method that is often employed is averaging, either in axial or circumferential directions, or in patches. These averaging approaches could in effect have cancelled out systematic errors caused by the setup of the computations. Continuing along these lines we employed the concept of clinical equivalence. This makes it possible to distinguish between significant differences based on the expected precision associated with the computational setup. A drawback of the averaging WSS data is that local information is always lost to at least a certain degree. This is unfortunate since atherosclerosis is a diffuse and transient disease with focal manifestation[28].

Boundary conditions that are measured invasively remain the gold-standard, but the scaling laws proved to be valuable method when those measurements are not available. Normalization of WSS was investigated to deal with the deviations that arise from using scaling laws to set the boundary conditions. It was shown that even in the cases where the boundary conditions were severely misrepresented, the normalized WSS consistently revealed areas exposed low or high WSS. With normalizing WSS the local aspect the spatial distribution is retained, but the possibility of coupling absolute WSS levels to events in the natural evolution atherosclerosis is lost. The added value of normalized WSS and how it should be interpreted have to be investigated further. One possibility of where normalized WSS could directly be valuable is in clinical follow-up studies. In order to perform such studies a lot of effort goes into registration the altered geometry and defining boundary conditions. By employing the normalization procedures these demands are alleviated. The normalized WSS will quickly reveal areas exposed to

lower or higher WSS in successive time steps. This in turn could be coupled to possible atherosclerotic disease progression. Another topic to explore is how normalized can be interpreted. For instance, should areas be conceived as at-risk when they are exposed to WSS 75% higher than the normalized value?

Reasons that contributed to the successful introduction of FFR in the clinic are: firstly, technology to measure FFR was available; secondly, the relative ease of performing the measurement; thirdly, a single cut-off value is obtained that can help steer treatment. The work in this thesis shows how currently available technology is suited to assess normalized WSS online. The 3D reconstruction techniques based on bi-plane angiography have evolved to the point that it can generate a volume directly. The geometry-based scaling laws to set the inflow and outflow conditions clear the way for the assessment of normalized WSS maps that can be provided during procedures. The proposed setup does not rely on additional invasive measurement. It only needs information acquired with angiography, which essential to any percutaneous procedure and therefore available in every catherization center. The normalized WSS map is therefore reasonably easy to obtain during a procedure or retrospectively. If WSS information is readily available in a clinical setting it could ignite further investigation to the role of WSS in the natural evolution of atherosclerosis. Subsequently, this could change the current status of WSS as additional information for atherosclerosis disease management. FFR is a normalized pressure parameter that provides a clear cut-off value for the management of atherosclerosis. Normalized WSS could in essence become such a marker as well.

The choices for the computational setup in this thesis were designed to deal with the limited computing power conceivably available in a clinical setting. First, steady-state simulations were performed since this speeds-up the computations drastically. Other investigators already concluded that wall shear stress from steady-state computations are in close agreement with the time-averaged WSS computations from transient simulations[38–40]. These findings were confirmed by the results in chapter 2. Second, the wall was considered rigid in all simulations. Computations using a fluid-structure interaction approach could account for the effects of a compliant wall. While this approach can be of great value when studying for instance wave reflections or the stress distribution inside the wall, previous reports show no major contribution of a compliant wall with regard to WSS[41–43]. Moreover, parameters that define the mechanical behavior of the wall need to be defined in these computations. It is not straightforward finding representative parameters for the material model due to the diffuse and heterogeneous nature of atherosclerosis. It is thus questionable if such an approach would lead to more accurate results. Third, the reduced-order models discussed in chapters 3 and 4 were developed in order to reduce the size of the 3D computational domain. With the ever-increasing

computational power the argument to use reduced-order models becomes less pressing, especially in research settings. However, in a clinical setting limited computational cost remains beneficial because it lowers the threshold for applications.

Risk-map

Two parameters can be associated with the rupture-risk of plaque: The thickness of the cap that separates a necrotic core from the lumen and elevated WSS over that cap. In chapter 6 a method is presented in which a unique and patient-specific risk-index map is constructed from the two imaged-based parameters that could be complementary to assess the rupture-risk of a plaque. The co-registration of the two parameters from the different imaging modalities proved to be accurate, shown by the high correspondence of the lengths of the reconstructions. The tool translates the information into one visual representation that enables a direct interpretation. The new risk index has potential to provide valuable information about plaque vulnerability. This risk-map could conceivably be included in a process of progressive decision making: e.g. CFD can first be used to identify regions exposed to high WSS and therefore potentially at-risk. This in could provide an additional incentive to interrogate a region of interest with OCT. Future studies should focus on the further integration of image-based techniques to stratify rupture-risk. Some important hurdles that still need to be taken are; devising methods that cope with heartbeat artifacts in imaging data, implementing and optimizing a framework for WSS computations based on 3D image reconstruction and optimization of the cap-detections algorithms from OCT data.

Conclusion

The work in this thesis focused on computing WSS in bifurcations of mildly diseased coronary arteries. In particular it looked at computing WSS by relying solely on angiographic imaging data for future clinical applications. One strategy to make 3D WSS computations more efficient is to use reduced-order models as outlet boundary conditions. Alternatively, geometry-based scaling laws are a more direct approach to set boundary conditions, but can still provide accurate qualitative WSS information. It was shown that absolute WSS obtained without invasive measurement and hybrid imaging techniques should be analyzed with caution. Regardless, the combination of geometry-based scaling laws and 3D reconstruction techniques allow for WSS computations based on angiography alone. It was shown that normalized WSS can be computed in a robust manner. The possibility to assess WSS by relying solely on angiography could facilitate the acceptance of WSS in the clinical setting. Especially in combination with other image-based parameters associated with plaque vulnerability - such as OCT-derived cap-thickness - WSS might help to establish patient-specific risk maps.
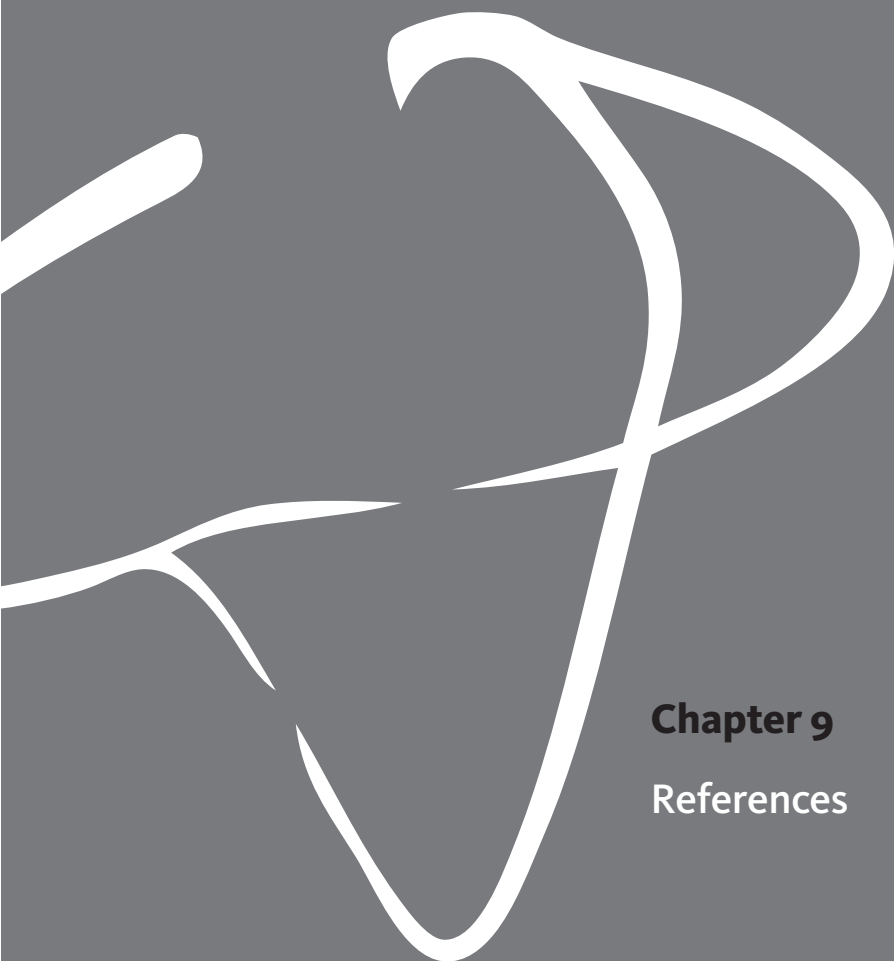
Chapter 9

References

CHAPTER 1

1. Nichols, M. *et al.* **Eur. Heart J.** 34, 3028–3034 (2013).
2. Nederlandse Hartstichting. (2013).
3. Kubo, T. *et al.* **J. Am. Coll. Cardiol.** 55, 1590–1597 (2010).
4. Libby, P. & Theroux, P. **Circulation** 111, 3481–3488 (2005).
5. Stary, H. C. *et al.* **Circulation** 89, 2462–2478 (1994).
6. Stary, H. C. *et al.* **Arterioscler. Thromb. Vasc. Biol.** 15, 1512–1531 (1995).
7. Virmani, R. *et al.* **Arterioscler. Thromb. Vasc. Biol.** 20, 1262–1275 (2000).
8. Schaar, J. a *et al.* **Eur. Heart J.** 25, 1077–82 (2004).
9. Cheruvu, P. K. *et al.* **J. Am. Coll. Cardiol.** 50, 940–949 (2007).
10. Falk, E., Shah, P. K. & Fuster, V. **Circulation** 92, 657–671 (1995).
11. Burke, A. P. *et al.* **N. Engl. J. Med.** (1997).
12. Wijns, W. *et al.* **Eur. Heart J.** 31, 2501–55 (2010).
13. Gould, K. L., Lipscomb, K. & Hamilton, G. W. **Am. J. Cardiol.** 33, 87–94 (1974).
14. Gould, K. L. & Lipscomb, K. **Am. J. Cardiol.** 34, 48–55 (1974).
15. Pijls, N. H. *et al.* **N. Engl. J. Med.** 334, 1703–8 (1996).
16. Pijls, N. H. J. & Sels, J.-W. E. M. **J. Am. Coll. Cardiol.** 59, 1045–57 (2012).
17. Tonino, P. a L. *et al.* **J. Am. Coll. Cardiol.** 55, 2816–21 (2010).
18. van Nunen, L. X. *et al.* **Lancet** in press, (2015).
19. Mintz, G. S. *et al.* **Eur. J. Echocardiogr.** 2, 299–313 (2001).
20. Kume, T. *et al.* **Am. J. Cardiol.** 97, 1172–1175 (2006).
21. Tearney, G. J. *et al.* **J. Am. Coll. Cardiol.** 59, 1058–72 (2012).
22. Wang, T. *et al.* **Opt. Lett.** 38, 1715–1717 (2013).
23. Newby, D. E. **Heart** 96, 1247–1251 (2010).
24. Davies, M. J. **Heart** 83, 361–366 (2000).
25. Virmani, R. *et al.* **J. Am. Coll. Cardiol.** 47, C13–C18 (2006).
26. Malek, A. M. & Alper, S. L. 282, 2035–2042 (1999).
27. Wentzel, J. J. *et al.* **Cardiovasc. Res.** 96, 234–43 (2012).
28. Cheng, C. *et al.* **Circulation** 113, 2744–53 (2006).
29. Chatzizisis, Y. S. *et al.* **J. Am. Coll. Cardiol.** 49, 2379–93 (2007).
30. Fox, B. *et al.* **Atherosclerosis** 41, 337–347 (1982).
31. Friedman, M. H. *et al.* **Atherosclerosis** 68, 27–33 (1987).
32. Kimura, B. J. *et al.* **J. Am. Coll. Cardiol.** 27, 825–831 (1996).
33. Nakazawa, G. *et al.* **J. Am. Coll. Cardiol.** 55, 1679–1687 (2010).
34. Slager, C. *et al.* **Nat. Clin. Pract. Cardiovasc. Med.** 2, 401–407 (2005).
35. Slager, C. J. *et al.* **Nat. Clin. Pract. Cardiovasc. Med.** 2, 456–64 (2005).
36. Chatzizisis, Y. S. *et al.* **Circulation** 123, 621–30 (2011).
37. Fukumoto, Y. *et al.* **J. Am. Coll. Cardiol.** 51, 645–50 (2008).
38. Fujii, K. *et al.* **Am. J. Cardiol.** 98, 429–35 (2006).
39. Gijsen, F. J. H. *et al.* **J. Biomech.** 46, 240–7 (2013).
40. Nieuwstadt, H. A. *et al.* **J. Biomech. Eng.** 136, (2013).
41. Akyildiz, A. C. *et al.* **Comput. Methods Biomech. Biomed. Engin.** 1–9 (2015).
42. Sadat, U., Teng, Z. & Gillard, J. H. **Expert Rev. Cardiovasc. Ther.** 8, 1469–1481 (2010).
43. Holzapfel, G. a. *et al.* **J. Biomech.** 47, 859–869 (2014).
44. Ohayon, J. *et al.* **Ann. Biomed. Eng.** 42, 269–279 (2014).

45. Cardoso, L. & Weinbaum, S. *Ann. Biomed. Eng.* 42, 415–431 (2014).
46. Eshtehardi, P. *et al. J. Am. Heart Assoc.* 1, e002543 (2012).
47. Kume, T. *et al. Am. Heart J.* 152, 755.e1–4 (2006).
48. Zahnd, G. *et al. Int. J. Comput. Assist. Radiol. Surg.* (2015).
49. Nieman, K. *et al. Lancet* 357, 599–603 (2001).
50. Dewey, M. *et al. Circulation* 120, 867–875 (2009).
51. Weustink, A. C. *et al. J. Am. Coll. Cardiol.* 50, 786–794 (2007).
52. van der Giessen, A. (PhD thesis - Erasmus Medical Center, 2010).
53. Boutsianis, E. *et al. Eur. J. Cardio-thoracic Surg.* 26, 248–256 (2004).
54. Myers, J. G. *et al. Ann. Biomed. Eng.* 29, 109–120 (2001).
55. Chaichana, T., Sun, Z. & Jewkes, J. *Phys. Medica* 29, 447–452 (2013).
56. Frauenfelder, T. *et al. Eur. Radiol.* 17, 1291–1300 (2007).
57. Goubergrits, L. *et al. Int. J. Cardiovasc. Imaging* 24, 411–21 (2008).
58. Bruschke, A. V. G. *et al. J. Am. Coll. Cardiol.* 54, 2139–2144 (2009).
59. Cheng, T. O. *Circulation* 107, E42–E42; author reply E42–E42 (2003).
60. Pijls, N. H. & de Bruyne, B. (Kluwer academic publishers, 2000).
61. Tu, S. *et al. Catheter. Cardiovasc. Interv.* 76, 291–8 (2010).
62. Tu, S. *et al. Int. J. Cardiovasc. Imaging* 26, 5–17 (2010).
63. Onuma, Y. *et al. EuroIntervention J. Eur. Collab. with Work. Gr. Interv. Cardiol. Eur. Soc. Cardiol.* 7, 629–635 (2011).
64. Corney, S., Johnston, P. R. & Kilpatrick, D. *Med. Biol. Eng. Comput.* 42, 660–668 (2004).
65. Girasis, C. *et al. EuroIntervention* 8, 1451–1460 (2013).
66. Goubergrits, L. *et al. Ann. Biomed. Eng.* 37, 682–91 (2009).
67. Johnston, B. M. *et al. J. Biomech.* 37, 709–720 (2004).
68. Johnston, B. M. *et al. J. Biomech.* 39, 1116–1128 (2006).
69. Zeng, D. *et al. Ann. Biomed. Eng.* 31, 420–429 (2003).
70. Zeng, D. *et al. J. Biomech. Eng.* 130, 041014 (2008).
71. Theodorakakos, a *et al. Phys. Med. Biol.* 53, 4875–4892 (2008).
72. De Santis, G. *et al. Med. Biol. Eng. Comput.* 48, 371–380 (2010).
73. Chen, M. C. Y. *et al. ASAIO J.* 51, 313–320 (2005).
74. Laban, M. *et al. Comput. Cariol.* 325–328 (1995).
75. Samady, H. *et al. Circulation* 124, 779–788 (2011).
76. Wentzel, J. J. *et al. Circulation* 103, 1740–1745 (2001).
77. Gijsen, F. J. H. *et al. J. Biomech.* 40, 2349–57 (2007).
78. Papafaklis, M. I. *et al. JACC Cardiovasc. Interv.* 3, 1181–1189 (2010).
79. Papafaklis, M. I. *et al. Atherosclerosis* 240, 205–211 (2015).
80. Bourantas, C. V *et al. EuroIntervention* 9, 582–93 (2013).
81. Stone, P. H. *et al. Circulation* 126, 172–81 (2012).
82. Bourantas, C. V *et al. Int. J. Cardiovasc. Imaging* 30, 485–94 (2014).
83. Ellwein, L. M. *et al. Cardiovasc. Eng. Technol.* 2, 212–227 (2011).
84. Toutouzas, K. *et al. Atherosclerosis* 240, 510–519 (2015).
85. Papafaklis, M. I. *et al. EuroIntervention* 11, 407 – 415 (2015).
86. van der Giessen, A. G. *et al. Int. J. Cardiovasc. Imaging* 26, 781–96 (2010).
87. Karanasos, A. *et al. Int. J. Cardiol.* 191, 279–283 (2015).
88. Bourantas, C. V. *et al. J. Am. Coll. Cardiol.* 61, 1369–1378 (2013).
89. Bourantas, C. V. *Press* (2015).

90. Gibson, C. M. *et al.* **Circulation** 99, 1945–1950 (1999).

91. Gibson, C. M. *et al.* **Circulation** 93, 879–888 (1996).

92. Tanedo, J. S. *et al.* **Catheter. Cardiovasc. Interv.** 53, 459–463 (2001).

93. Doucette, J. W. *et al.* **Circulation** 85, 1899–1911 (1992).

94. Segal, J. *et al.* **J. Am. Coll. Cardiol.** 20, 276–286 (1992).

95. Pijls, N. H. J. **Circulation** 105, 2482–2486 (2002).

96. MacCarthy, P. *et al.* **J. Am. Coll. Cardiol.** 45, 216–20 (2005).

97. van der Horst, A. *et al.* **Med. Eng. Phys.** 33, 684–691 (2011).

98. Siebes, M. *et al.* **Circulation** 109, 756–62 (2004).

99. Rossi, A. *et al.* **Radiology** 270, (2014).

100. Bamberg, F. *et al.* **Radiology** 260, 689–698 (2011).

101. Kurata, A. *et al.* **Eur. Radiol.** 25, 49–57 (2015).

102. Meinel, F. G. *et al.* **AJR Am J Roentgenol** 174–180 (2014).

103. Kono, A. K. *et al.* **Invest. Radiol.** 49, 801–7 (2014).

104. van de Vosse, F. N. & Stergiopulos, N. **Annu. Rev. Fluid Mech.** 43, 467–499 (2011).

105. Taylor, C. a & Figueroa, C. a. **Annu. Rev. Biomed. Eng.** 11, 109–34 (2009).

106. Shi, Y., Lawford, P. & Hose, R. **Biomed. Eng. Online** 10, 33 (2011).

107. Bessems, D., Rutten, M. & Van De Vosse, F. **J. Fluid Mech.** 580, 145–168 (2007).

108. Huberts, W. *et al.* **Med. Eng. Phys.** 34, 233–48 (2012).

109. van der Horst, A. *et al.* **Comput. Math. Methods Med.** 15 (2013).

110. Kim, H. J. *et al.* **Ann. Biomed. Eng.** 38, 3195–209 (2010).

111. Vignon-Clementel, I. E. *et al.* **Comput. Methods Appl. Mech. Eng.** 195, 3776–3796 (2006).

112. Hughes, J. R. & Lubliner, J. **Math. Biosci.** 18, 161–170 (1973).

113. Stergiopulos, N., Young, D. F. & Rogge, T. R. **J. Biomech.** 25, 1477–88 (1992).

114. Reymond, P. *et al.* **Am. J. Physiol. Heart Circ. Physiol.** 297, H208–22 (2009).

115. Wan, J. *et al.* **Comput. Methods Biomech. Biomed. Engin.** 5, 195–206 (2002).

116. Womersley, J. R. **J. Physiol.** 127, 553–563 (1955).

117. Westerhof, N. *et al.* **J. Biomech.** 2, 121–143 (1969).

118. Formaggia, L. *et al.* **Comput. Methods Appl. Mech. Eng.** 191, 561–582 (2001).

119. Figueroa, C. A. *et al.* **Comput. Methods Appl. Mech. Eng.** 195, 5685–5706 (2006).

120. Murray, C. D. **Proc. Natl. Acad. Sci. U. S. A.** 12, 207–214 (1926).

121. Sherman, T. F. **J. Gen. Physiol.** 78, 431–453 (1981).

122. LaBarbera, M. **Science (80-.).** 249, 992–1000 (1990).

123. Zamir, M., Sinclair, P. & Wonnacott, T. H. **J. Biomech.** 25, 1303–10 (1992).

124. van Bavel, E. & Spaan, J. a. **Circ. Res.** 71, 1200–1212 (1992).

125. Kassab, G. S. *et al.* **Am. J. Physiol.** 265, H350–H365 (1993).

126. Mittal, N. *et al.* **Am. J. Physiol. Heart Circ. Physiol.** 289, H439–46 (2005).

127. Zhou, Y., Kassab, G. S. & Molloi, S. **Phys. Med. Biol.** 47, 977–93 (2002).

128. Kassab, G. S. **Am. J. Physiol. Heart Circ. Physiol.** 290, H894–903 (2006).

129. Doriot, P. a *et al.* **Coron. Artery Dis.** 11, 495–502 (2000).

130. van der Giessen, A. G. *et al.* **J. Biomech.** 44, 1089–95 (2011).

131. Zhang, J.-M. *et al.* **Biomed Res. Int.** 2014, (2014).

132. Soulis, J. V. *et al.* **J. Biomech.** 39, 742–749 (2006).

133. Rikhtegar, F. *et al.* **J. Biomech.** 47, 505–511 (2014).

134. Joshi, A. K. *et al.* **Arterioscler. Thromb. Vasc. Biol.** 24, 2408–2413 (2004).

135. Stone, P. H. *et al.* **Eur. Heart J.** 28, 705–10 (2007).

136. Chatzizisis, Y. S. *et al.* **Circulation** 117, 993–1002 (2008).
137. Stone, P. H. *et al.* **Circulation** 108, 438–44 (2003).
138. Wentzel, J. J. *et al.* **J. Biomech.** 36, 681–688 (2003).
139. Gijsen, F. J. H. *et al.* **Am. J. Cardiol.** 92, 1325–1328 (2003).
140. Gijsen, F. J. H. *et al.* **Am. J. Physiol. Heart Circ. Physiol.** 295, 1608–1614 (2008).
141. Taylor, C. a, Fonte, T. a & Min, J. K. **J. Am. Coll. Cardiol.** 61, 2233–41 (2013).
142. Koo, B.-K. *et al.* **J. Am. Coll. Cardiol.** 58, 1989–97 (2011).
143. Min, J. K. *et al.* **JAMA** 308, 1237–45 (2012).
144. Nørgaard, B. L. *et al.* **J. Am. Coll. Cardiol.** 63, 1145–55 (2014).
145. Morris, P. D. *et al.* **JACC. Cardiovasc. Interv.** 6, 149–57 (2013).
146. Tu, S. *et al.* **JACC. Cardiovasc. Interv.** 7, 768–77 (2014).
147. Morris, P. D. *et al.* **JACC Cardiovasc. Interv.** 8, 1009–1017 (2015).

CHAPTER 2

1. Virmani, R. *et al.* **Arterioscler. Thromb. Vasc. Biol.** 20, 1262–1275 (2000).
2. Newby, D. E. **Heart** 96, 1247–1251 (2010).
3. Slager, C. *et al.* **Nat. Clin. Pract. Cardiovasc. Med.** 2, 401–407 (2005).
4. Stone, P. H. *et al.* **Circulation** 126, 172–81 (2012).
5. Gijsen, F. J. H. *et al.* **Am. J. Physiol. Heart Circ. Physiol.** 295, 1608–1614 (2008).
6. Nakazawa, G. *et al.* **J. Am. Coll. Cardiol.** 55, 1679–1687 (2010).
7. Samady, H. *et al.* **Circulation** 124, 779–88 (2011).
8. Fukumoto, Y. *et al.* **J. Am. Coll. Cardiol.** 51, 645–50 (2008).
9. Gijsen, F. J. H. *et al.* **J. Biomech.** 46, 240–7 (2013).
10. Fujii, K. *et al.* **Am. J. Cardiol.** 98, 429–35 (2006).
11. Cicha, I. *et al.* **Stroke.** 42, 3502–10 (2011).
12. Slager, C. J. *et al.* **Circulation** 102, 511–516 (2000).
13. Corban, M. T. *et al.* **Atherosclerosis** 232, 271–6 (2014).
14. Bourantas, C. V *et al.* **EuroIntervention** 9, 582–93 (2013).
15. Tu, S. *et al.* **Int. J. Cardiovasc. Imaging** 27, 197–207 (2011).
16. Onuma, Y. *et al.* **EuroIntervention J. Eur. Collab. with Work. Gr. Interv. Cardiol. Eur. Soc. Cardiol.** 7, 629–635 (2011).
17. Girasis, C. *et al.* **EuroIntervention** 8, 1451–1460 (2013).
18. Zeng, D. *et al.* **J. Biomech. Eng.** 130, 041014 (2008).
19. Goubergrits, L. *et al.* **Ann. Biomed. Eng.** 37, 682–91 (2009).
20. Johnston, B. M. *et al.* **J. Biomech.** 39, 1116–1128 (2006).
21. Chen, M. C. Y. *et al.* **ASAIO J.** 51, 313–320 (2005).
22. De Santis, G. *et al.* **Med. Biol. Eng. Comput.** 48, 371–380 (2010).
23. Wellnhofer, E. *et al.* **Biomed. Eng. Online** 5, 39 (2006).
24. Wellnhofer, E. *et al.* **Atherosclerosis** 202, 483–90 (2009).
25. Wellnhofer, E. *et al.* **Atherosclerosis** 213, 475–81 (2010).
26. Wellnhofer, E. *et al.* **Int. J. Card. Imaging** 15, 339–53; discussion 355–6 (1999).
27. Goubergrits, L. *et al.* **Int. J. Cardiovasc. Imaging** 24, 411–21 (2008).
28. Girasis, C. *et al.* **Catheter. Cardiovasc. Interv.** 77, 790–7 (2011).
29. Pijls, N. H. & de Bruyne, B. (Kluwer academic publishers, 2000).

30. Bovendeerd, P. H. M. *et al.* **Ann. Biomed. Eng.** 34, 1833–45 (2006).
31. van der Giessen, A. G. *et al.* **J. Biomech.** 44, 1089–95 (2011).
32. Cho, Y. I. & Kensey, K. R. **Biorheology** 28, 241–262 (1991).
33. He, X. & Ku, D. N. **J. Biomech. Eng.** 118, 74–82 (1996).
34. Lee, S.-W., Antiga, L. & Steinman, D. a. **J. Biomech. Eng.** 131, 061013 (2009).
35. Wentzel, J. J. *et al.* **Cardiovasc. Res.** 96, 234–43 (2012).
36. Wentzel, J. J. *et al.* **J. Biomech.** 38, 1551–5 (2005).
37. Walker, E. & Nowacki, A. S. **J. Gen. Intern. Med.** 26, 192–196 (2011).
38. Schrauwen, J. T. C. *et al.* **Ann. Biomed. Eng.** (2014).
39. Myers, J. G. *et al.* **Ann. Biomed. Eng.** 29, 109–120 (2001).
40. Van Langenhove, G. *et al.* **Circulation** 102, e22–e24 (2000).
41. Grigioni, M. *et al.* **J. Biomech.** 38, 1375–1386 (2005).
42. Morbiducci, U. *et al.* **Ann. Biomed. Eng.** 37, 516–531 (2009).
43. Caro, C. G. *et al.* **Proc. R. Soc. A Math. Phys. Eng. Sci.** 452, 185–197 (1996).
44. Bourantas, C. V *et al.* **Int. J. Cardiovasc. Imaging** 30, 485–94 (2014).
45. Feldman, C. L. *et al.* **Am. Heart J.** 143, 931–939 (2002).
46. Schrauwen, J. T. C. *et al.* **J. Biomech.** in press, (2015).
47. Peiffer, V., Sherwin, S. J. & Weinberg, P. D. **Cardiovasc. Res.** 99, 242–50 (2013).
48. Leter, E. M. *et al.* **Int. J. Radiat. Oncol. Biol. Phys.** 58, 278–283 (2004).

CHAPTER 3

1. Stary, H. C. *et al.* **Arterioscler. Thromb. Vasc. Biol.** 15, 1512–1531 (1995).
2. Falk, E., Shah, P. K. & Fuster, V. **Circulation** 92, 657–671 (1995).
3. Gijsen, F. J. H. *et al.* **EuroIntervention** 7, 121–7 (2011).
4. Gijsen, F. J. H. *et al.* **Am. J. Physiol. Heart Circ. Physiol.** 295, 1608–1614 (2008).
5. Fukumoto, Y. *et al.* **J. Am. Coll. Cardiol.** 51, 645–50 (2008).
6. de Weert, T. T. *et al.* **Stroke.** 40, 1334–40 (2009).
7. Gijsen, F. J. H. *et al.* **J. Biomech.** 46, 240–7 (2013).
8. Kim, H. J., Jansen, K. E. & Taylor, C. a. **Ann. Biomed. Eng.** 38, 2314–30 (2010).
9. Slager, C. J. *et al.* **Circulation** 102, 511–516 (2000).
10. Stone, P. H. *et al.* **Circulation** 126, 172–81 (2012).
11. van der Giessen, A. G. *et al.* **Int. J. Cardiovasc. Imaging** 26, 781–96 (2010).
12. van der Giessen, A. G. *et al.* **J. Biomech.** 44, 1089–95 (2011).
13. Mollet, N. R. *et al.* **Am. J. Cardiol.** 95, 1165–9 (2005).
14. Girasis, C. *et al.* **EuroIntervention** 8, 1451–60 (2013).
15. Tu, S. *et al.* **Int. J. Cardiovasc. Imaging** 28, 1617–25 (2012).
16. Pijls, N. H. *et al.* **N. Engl. J. Med.** 334, 1703–8 (1996).
17. Tonino, P. a L. *et al.* **J. Am. Coll. Cardiol.** 55, 2816–21 (2010).
18. Young, D. & Tsai, F. **J. Biomech.** 6, 395–410 (1973).
19. Young, D. & Tsai, F. **J. Biomech.** 6, 547–559 (1973).
20. Gould, K. L., Kelley, K. O. & Bolson, E. L. **Circulation** 66, 930–937 (1982).
21. Stone, G. W. *et al.* **N. Engl. J. Med.** 364, 226–35 (2011).
22. Bijari, P. B. *et al.* **J. Biomech.** 45, 1632–7 (2012).
23. Pijls, N. H. & de Bruyne, B. (Kluwer academic publishers, 2000).

24. Banerjee, R. K. *et al.* **Biomed. Eng. Online** 7, 24 (2008).
25. Stergiopulos, N., Young, D. F. & Rogge, T. R. **J. Biomech.** 25, 1477–88 (1992).
26. van der Horst, A. *et al.* **Comput. Math. Methods Med.** 15 (2013).
27. Kim, H. J. *et al.* **Ann. Biomed. Eng.** 38, 3195–209 (2010).
28. Koo, B.-K. *et al.* **JACC. Cardiovasc. Interv.** 5, 1126–32 (2012).
29. Min, J. K. *et al.* **JAMA** 308, 1237–45 (2012).
30. Huo, Y. & Kassab, G. S. **Am. J. Physiol. Heart Circ. Physiol.** 291, H1074–87 (2006).
31. Olufsen, M. S. **Am. J. Physiol. Heart Circ. Physiol.** 276, 257–268 (1999).
32. Pahlevan, N. M. *et al.* **Ann. Biomed. Eng.** 39, 1470–81 (2011).
33. Corban, M. T. *et al.* **Atherosclerosis** 232, 271–6 (2014).
34. Johnston, B. M. *et al.* **J. Biomech.** 39, 1116–28 (2006).
35. Feldman, C. L. *et al.* **Am. Heart J.** 143, 931–939 (2002).
36. Myers, J. G. *et al.* **Ann. Biomed. Eng.** 29, 109–120 (2001)

CHAPTER 4

1. Falk, E., Shah, P. K. & Fuster, V. **Circulation** 92, 657–671 (1995).
2. Virmani, R. *et al.* **Arterioscler. Thromb. Vasc. Biol.** 20, 1262–1275 (2000).
3. Schaar, J. a *et al.* **Eur. Heart J.** 25, 1077–82 (2004).
4. Stone, G. W. *et al.* **N. Engl. J. Med.** 364, 226–35 (2011).
5. Gijsen, F. J. H. *et al.* **J. Biomech.** 46, 240–7 (2013).
6. Samady, H. *et al.* **Circulation** 124, 779–88 (2011).
7. Kim, H. J., Jansen, K. E. & Taylor, C. a. **Ann. Biomed. Eng.** 38, 2314–30 (2010).
8. Girasis, C. *et al.* **Catheter. Cardiovasc. Interv.** 77, 790–7 (2011).
9. Tu, S. *et al.* **Int. J. Cardiovasc. Imaging** 28, 1617–25 (2012).
10. Formaggia, L. *et al.* **Comput. Methods Appl. Mech. Eng.** 191, 561–582 (2001).
11. Taylor, C. a & Figueroa, C. a. **Annu. Rev. Biomed. Eng.** 11, 109–34 (2009).
12. van de Vosse, F. N. & Stergiopulos, N. **Annu. Rev. Fluid Mech.** 43, 467–499 (2011).
13. Young, D. & Tsai, F. **J. Biomech.** 6, 395–410 (1973).
14. Young, D. & Tsai, F. **J. Biomech.** 6, 547–559 (1973).
15. Gould, K. L., Kelley, K. O. & Bolson, E. L. **Circulation** 66, 930–937 (1982).
16. Schrauwen, J. *et al.* **J. Biomech.** 47, 1810–5 (2014).
17. Stone, P. H. *et al.* **Circulation** 126, 172–81 (2012).
18. Mollet, N. R. *et al.* **Am. J. Cardiol.** 95, 1165–9 (2005).
19. van der Giessen, A. G. *et al.* **J. Biomech.** 44, 1089–95 (2011).
20. Kim, H. J. *et al.* **Ann. Biomed. Eng.** 37, 2153–69 (2009).
21. Wan, J. *et al.* **Comput. Methods Biomech. Biomed. Engin.** 5, 195–206 (2002).
22. Fukumoto, Y. *et al.* **J. Am. Coll. Cardiol.** 51, 645–50 (2008).
23. Wentzel, J. J. *et al.* **Cardiovasc. Res.** 96, 234–43 (2012).
24. Pijls, N. H. *et al.* **N. Engl. J. Med.** 334, 1703–8 (1996).
25. Vignon-Clementel, I. E. *et al.* **Comput. Methods Appl. Mech. Eng.** 195, 3776–3796 (2006).
26. Hughes, J. R. & Lubliner, J. **Math. Biosci.** 18, 161–170 (1973).
27. Olufsen, M. S. **Am. J. Physiol. Heart Circ. Physiol.** 276, 257–268 (1999).
28. Huberts, W. *et al.* **Med. Eng. Phys.** 34, 233–48 (2012).
29. Huo, Y. & Kassab, G. S. **Am. J. Physiol. Heart Circ. Physiol.** 292, H2623–33 (2007).

30. Reymond, P. *et al.* ***Am. J. Physiol. Heart Circ. Physiol.*** 297, H208–22 (2009).
31. van der Horst, A. *et al.* ***Comput. Math. Methods Med.*** 15 (2013).
32. Kroon, W. *et al.* ***Comput. Math. Methods Med.*** 2012, 156094 (2012).
33. Bessems, D., Rutten, M. & Van De Vosse, F. ***J. Fluid Mech.*** 580, 145–168 (2007).
34. Huo, Y. & Kassab, G. S. ***Am. J. Physiol. Heart Circ. Physiol.*** 291, H1074–87 (2006).
35. Pahlevan, N. M. *et al.* ***Ann. Biomed. Eng.*** 39, 1470–81 (2011)

CHAPTER 5

1. Tonino, P. a L. *et al.* ***J. Am. Coll. Cardiol.*** 55, 2816–21 (2010).
2. Pijls, N. H. *et al.* ***N. Engl. J. Med.*** 334, 1703–8 (1996).
3. Gijsen, F. J. H. *et al.* ***J. Biomech.*** 46, 240–7 (2013).
4. Stone, P. H. *et al.* ***Circulation*** 126, 172–81 (2012).
5. Wentzel, J. J. *et al.* ***Cardiovasc. Res.*** 96, 234–43 (2012).
6. Taylor, C. a & Steinman, D. a. ***Ann. Biomed. Eng.*** 38, 1188–203 (2010).
7. Rossi, A. *et al.* ***Radiology*** 270, (2014).
8. Kurata, A. *et al.* ***Eur. Radiol.*** 25, 49–57 (2015).
9. Gould, K. L. *et al.* ***J. Am. Coll. Cardiol.*** 62, 1639–53 (2013).
10. LaBarbera, M. ***Science.*** 249, 992–1000 (1990).
11. Rossi, A. *et al.* ***Eur. Heart J. Cardiovasc. Imaging*** 15, 85–94 (2014).
12. Kono, A. K. *et al.* ***Invest. Radiol.*** 49, 801–7 (2014).
13. Schaap, M. *et al.* ***Med. Image Anal.*** 13, 701–14 (2009).
14. Kirişli, H. a *et al.* ***Med. Image Anal.*** 17, 859–76 (2013).
15. Piccinelli, M. *et al.* ***IEEE Trans. Med. Imaging*** 28, 1141–55 (2009).
16. Cho, Y. I. & Kensey, K. R. ***Biorheology*** 28, 241–262 (1991).
17. Wilson, R. F. *et al.* ***Circulation*** 82, 1595–1606 (1990).
18. van der Giessen, A. G. *et al.* ***J. Biomech.*** 44, 1089–95 (2011).
19. Avanzini, F. *et al.* ***J. Hypertens.*** 24, 2377–85 (2006).
20. Bamberg, F. *et al.* ***Radiology*** 260, 689–698 (2011).
21. Taylor, C. a, Fonte, T. a & Min, J. K. ***J. Am. Coll. Cardiol.*** 61, 2233–41 (2013).
22. Morris, P. D. *et al.* ***JACC. Cardiovasc. Interv.*** 6, 149–57 (2013).
23. Schrauwen, J. T. C. *et al.* ***Ann. Biomed. Eng.*** 43, 59–67 (2014).
24. Takarada, S., Zhang, Z. & Molloi, S. ***Int. J. Cardiovasc. Imaging*** 29, 535–44 (2013).
25. Tu, S. *et al.* ***JACC. Cardiovasc. Interv.*** 7, 768–77 (2014).
26. Wong, J. T. *et al.* ***Int. J. Cardiovasc. Imaging*** 28, 13–22 (2012).
27. Trachet, B. *et al.* ***J. Biomech. Eng.*** 133, (2011).
28. van de Vosse, F. N. & Stergiopulos, N. ***Annu. Rev. Fluid Mech.*** 43, 467–499 (2011).
29. Sommer, K. *et al.* ***Ann. Biomed. Eng.*** 42, 1–10 (2013).
30. Murray, C. D. ***Proc. Natl. Acad. Sci. U. S. A.*** 12, 207–214 (1926).
31. Peiffer, V., Sherwin, S. J. & Weinberg, P. D. ***Cardiovasc. Res.*** 99, 242–50 (2013).
32. Chatzizisis, Y. S. *et al.* ***J. Am. Coll. Cardiol.*** 49, 2379–93 (2007).
33. Wellnhofer, E. *et al.* ***Atherosclerosis*** 202, 483–90 (2009).
34. Fukumoto, Y. *et al.* ***J. Am. Coll. Cardiol.*** 51, 645–50 (2008).
35. Wentzel, J. J. *et al.* ***Circulation*** 103, 1740–1745 (2001).
36. Wentzel, J. J. *et al.* ***J. Biomech.*** 33, 1287–1295 (2000).

37. Termeer, M. *et al.* ***Dagstuhl Follow.*** 1, 196–209 (2010).
38. Karch, R. *et al.* ***Ann. Biomed. Eng.*** 31, 548–563 (2003).
39. van Horssen, P. *et al.* ***Am. J. Physiol. Heart Circ. Physiol.*** 306, H496–504 (2014).

CHAPTER 6

1. Falk, E., Shah, P. K. & Fuster, V. ***Circulation*** 92, 657–671 (1995).
2. Nakazawa, G. *et al.* ***J. Am. Coll. Cardiol.*** 55, 1679–1687 (2010).
3. Wentzel, J. J. *et al.* ***Cardiovasc. Res.*** 96, 234–43 (2012).
4. Slager, C. *et al.* ***Nat. Clin. Pract. Cardiovasc. Med.*** 2, 401–407 (2005).
5. Fujii, K. *et al.* ***Am. J. Cardiol.*** 98, 429–35 (2006).
6. Gijsen, F. J. H. *et al.* ***J. Biomech.*** 46, 240–7 (2013).
7. Samady, H. *et al.* ***Circulation*** 124, 779–88 (2011).
8. Gijsen, F. J. H. *et al.* ***Am. J. Physiol. Heart Circ. Physiol.*** 295, 1608–1614 (2008).
9. Girasis, C. *et al.* ***EuroIntervention*** 8, 1451–1460 (2013).
10. Tu, S. *et al.* ***Int. J. Cardiovasc. Imaging*** 28, 1617–25 (2012).
11. Goubergrits, L. *et al.* ***Ann. Biomed. Eng.*** 37, 682–91 (2009).
12. Timmins, L. H. *et al.* ***Ann. Biomed. Eng.*** 43, 94–106 (2014).
13. Murray, C. D. ***Proc. Natl. Acad. Sci. U. S. A.*** 12, 207–214 (1926).
14. Huo, Y. & Kassab, G. S. ***J. R. Soc. Interface*** 9, 190–200 (2012).
15. Mittal, N. *et al.* ***Am. J. Physiol. Heart Circ. Physiol.*** 289, H439–46 (2005).
16. Molloi, S. & Wong, J. T. ***Phys. Med. Biol.*** 52, 1495–503 (2007).
17. LaBarbera, M. ***Science.*** 249, 992–1000 (1990).
18. Kassab, G. S. ***Am. J. Physiol. Heart Circ. Physiol.*** 290, H894–903 (2006).
19. van Bavel, E. & Spaan, J. a. ***Circ. Res.*** 71, 1200–1212 (1992).
20. van der Giessen, A. G. *et al.* ***J. Biomech.*** 44, 1089–95 (2011).
21. Soulis, J. V. *et al.* ***J. Biomech.*** 39, 742–749 (2006).
22. Rikhtegar, F. *et al.* ***J. Biomech.*** 47, 505–511 (2014).
23. Joshi, A. K. *et al.* ***Arterioscler. Thromb. Vasc. Biol.*** 24, 2408–2413 (2004).
24. Zhang, J.-M. *et al.* ***Biomed Res. Int.*** 2014, (2014).
25. Chaichana, T., Sun, Z. & Jewkes, J. ***Phys. Medica*** 29, 447–452 (2013).
26. Nolte, F. *et al.* ***EuroIntervention*** 10, 320–328 (2013).
27. Schrauwen, J. T. C. *et al.* ***J. Biomech.*** in press, (2015).
28. Cho, Y. I. & Kensey, K. R. ***Biorheology*** 28, 241–262 (1991).
29. Myers, J. G. *et al.* ***Ann. Biomed. Eng.*** 29, 109–120 (2001).
30. Feldman, C. L. *et al.* ***Am. Heart J.*** 143, 931–939 (2002).
31. Johnston, B. M. *et al.* ***J. Biomech.*** 39, 1116–28 (2006).
32. Stone, P. H. *et al.* ***Circulation*** 126, 172–81 (2012).
33. Walker, E. & Nowacki, A. S. ***J. Gen. Intern. Med.*** 26, 192–196 (2011).
34. Schrauwen, J. T. C. *et al.* ***PlosOne*** (2016).
35. Doriot, P. a *et al.* ***Coron. Artery Dis.*** 11, 495–502 (2000).
36. Samady, H. *et al.* ***Circulation*** 124, 779–788 (2011).
37. Sommer, K. *et al.* ***Ann. Biomed. Eng.*** 42, 1–10 (2013).
38. Malvè, M. *et al.* ***Ann. Biomed. Eng.*** 43, 82–93 (2014).
39. Gijsen, F. J. H. *et al.* ***J. Biomech.*** 47, 39–43 (2014).

40.   Wellnhofer, E. *et al.* **Atherosclerosis** 213, 475–81 (2010).
41.   Li, Y. *et al.* **J. Am. Coll. Cardiol.** 66, 125–135 (2015).
42.   Molony, D. S. *et al.* **Biomed. Eng. Online** 14, 1–14 (2015).
43.   Peiffer, V., Sherwin, S. J. & Weinberg, P. D. **Cardiovasc. Res.** 99, 242–50 (2013).
44.   Cheng, C. *et al.* **Atherosclerosis** 195, 225–35 (2007).
45.   Eshtehardi, P. *et al.* **J. Am. Heart Assoc.** 1, e002543 (2012).
46.   Marzo, A. *et al.* **Ann. Biomed. Eng.** 39, 884–896 (2011).
47.   Taylor, C. a, Fonte, T. a & Min, J. K. **J. Am. Coll. Cardiol.** 61, 2233–41 (2013).
48.   Morris, P. D. *et al.* **JACC Cardiovasc. Interv.** 8, 1009–1017 (2015).
49.   Valen-Sendstad, K. *et al.* **Ann. Biomed. Eng.** 43, 1422–1431 (2015).
50.   Lee, S.-W., Antiga, L. & Steinman, D. a. **J. Biomech. Eng.** 131, 061013 (2009).

CHAPTER 7

1.   ***World Heal. Organ. (Fact sheet number 317)***
2.   Cheruvu, P. K. *et al.* **J. Am. Coll. Cardiol.** 50, 940–949 (2007).
3.   Falk, E., Shah, P. K. & Fuster, V. **Circulation** 92, 657–671 (1995).
4.   Burke, A. P. *et al.* **N. Engl. J. Med.** (1997).
5.   Libby, P. & Theroux, P. **Circulation** 111, 3481–3488 (2005).
6.   Virmani, R. *et al.* **Arterioscler. Thromb. Vasc. Biol.** 20, 1262–1275 (2000).
7.   Schaar, J. a *et al.* **Eur. Heart J.** 25, 1077–82 (2004).
8.   Gijsen, F. J. H. *et al.* **J. Biomech.** 46, 240–7 (2013).
9.   Yonetsu, T. *et al.* **Eur. Heart J.** 32, 1251–1259 (2011).
10.   Wentzel, J. J. *et al.* **Cardiovasc. Res.** 96, 234–43 (2012).
11.   Gijsen, F. J. H. *et al.* **Am. J. Physiol. Heart Circ. Physiol.** 295, 1608–1614 (2008).
12.   Samady, H. *et al.* **Circulation** 124, 779–88 (2011).
13.   Fukumoto, Y. *et al.* **J. Am. Coll. Cardiol.** 51, 645–50 (2008).
14.   Kume, T. *et al.* **Am. Heart J.** 152, 755.e1–4 (2006).
15.   Tearney, G. J. *et al.* **J. Am. Coll. Cardiol.** 59, 1058–72 (2012).
16.   Tu, S. *et al.* **Int. J. Cardiovasc. Imaging** 28, 1617–25 (2012).
17.   Girasis, C. *et al.* **EuroIntervention** 8, 1451–1460 (2013).
18.   Johnston, B. M. *et al.* **J. Biomech.** 39, 1116–1128 (2006).
19.   Goubergrits, L. *et al.* **Ann. Biomed. Eng.** 37, 682–91 (2009).
20.   Toutouzas, K. *et al.* **Atherosclerosis** 240, 510–519 (2015).
21.   Li, Y. *et al.* **J. Am. Coll. Cardiol.** 66, 125–135 (2015).
22.   Molony, D. S. *et al.* **Biomed. Eng. Online** 14, 1–14 (2015).
23.   Vergallo, R. *et al.* **Circ. Cardiovasc. Imaging** 7, 905–911 (2014).
24.   Zahnd, G. *et al.* **Int. J. Comput. Assist. Radiol. Surg.** (2015).
25.   Cohen, L. (Springer US, 2005).
26.   Schrauwen, J. T. C. *et al.* **J. Biomech.** in press, (2015).
27.   van der Giessen, A. G. *et al.* **Int. J. Cardiovasc. Imaging** 26, 781–96 (2010).
28.   Stone, P. H. *et al.* **Circulation** 126, 172–81 (2012).
29.   Narula, J. *et al.* **J. Am. Coll. Cardiol.** 61, 1041–1051 (2014).
30.   Toutouzas, K. *et al.* **Am. Heart J.** 161, 1192–1199 (2011).
31.   Chatzizisis, Y. S. *et al.* **Circulation** 117, 993–1002 (2008).

32. Wentzel, J. J. *et al.* **EuroIntervention** 989–995 (2013).
33. Slager, C. J. *et al.* **Nat. Clin. Pract. Cardiovasc. Med.** 2, 456–64 (2005).
34. Napoli, C. *et al.* **Circulation** 114, 2517–2527 (2006)

CHAPTER 8

1. Cheruvu, P. K. *et al.* **J. Am. Coll. Cardiol.** 50, 940–949 (2007).
2. Falk, E., Shah, P. K. & Fuster, V. **Circulation** 92, 657–671 (1995).
3. Burke, A. P. *et al.* **N. Engl. J. Med.** (1997).
4. Schaar, J. a *et al.* **Eur. Heart J.** 25, 1077–82 (2004).
5. Wentzel, J. J. *et al.* **Cardiovasc. Res.** 96, 234–43 (2012).
6. Slager, C. *et al.* **Nat. Clin. Pract. Cardiovasc. Med.** 2, 401–407 (2005).
7. Cheng, C. *et al.* **Circulation** 113, 2744–53 (2006).
8. Bourantas, C. V. *et al.* **J. Am. Coll. Cardiol.** 61, 1369–1378 (2013).
9. Tu, S. *et al.* **Catheter. Cardiovasc. Interv.** 76, 291–8 (2010).
10. Girasis, C. *et al.* **EuroIntervention** 8, 1451–1460 (2013).
11. Goubergrits, L. *et al.* **Ann. Biomed. Eng.** 37, 682–91 (2009).
12. Virmani, R. *et al.* **J. Am. Coll. Cardiol.** 47, C13–C18 (2006).
13. Leter, E. M. *et al.* **Int. J. Radiat. Oncol. Biol. Phys.** 58, 278–283 (2004).
14. Gijsen, F. J. H. *et al.* **J. Biomech.** 47, 39–43 (2014).
15. Wang, T. *et al.* **J. Am. Coll. Cardiol. Cardiovasc. Imaging** 'in press', (2015).
16. Young, D. & Tsai, F. **J. Biomech.** 6, 395–410 (1973).
17. Siebes, M., D'Argenio, D. Z. & Selzer, R. H. **Comput. Methods Programs Biomed.** 21, 143–52 (1985).
18. Gould, K. L., Kelley, K. O. & Bolson, E. L. **Circulation** 66, 930–937 (1982).
19. Tu, S. *et al.* **JACC Cardiovasc. Interv.** 8, 564–574 (2015).
20. Coenen, A. *et al.* **Radiology** 274, 674–683 (2015).
21. Morris, P. D. *et al.* **JACC. Cardiovasc. Interv.** 6, 149–57 (2013).
22. Tu, S. *et al.* **JACC. Cardiovasc. Interv.** 7, 768–77 (2014).
23. Morris, P. D. *et al.* **JACC Cardiovasc. Interv.** 8, 1009–1017 (2015).
24. Taylor, C. a, Fonte, T. a & Min, J. K. **J. Am. Coll. Cardiol.** 61, 2233–41 (2013).
25. Smith, N. *et al.* **Interface Focus** 1, 349–364 (2011).
26. Doriot, P. a *et al.* **Coron. Artery Dis.** 11, 495–502 (2000).
27. van der Giessen, A. G. *et al.* **J. Biomech.** 44, 1089–95 (2011).
28. Kubo, T. *et al.* **J. Am. Coll. Cardiol.** 55, 1590–1597 (2010).
29. Vergallo, R. *et al.* **Circ. Cardiovasc. Imaging** 7, 905–911 (2014).
30. Toutouzas, K. *et al.* **Atherosclerosis** 240, 510–519 (2015).
31. Bovendeerd, P. H. M. *et al.* **Ann. Biomed. Eng.** 34, 1833–45 (2006).
32. Stone, P. H. *et al.* **Circulation** 108, 438–44 (2003).
33. Chatzizisis, Y. S. *et al.* **Circulation** 117, 993–1002 (2008).
34. Stone, P. H. *et al.* **Circulation** 126, 172–81 (2012).
35. Li, Y. *et al.* **J. Am. Coll. Cardiol.** 66, 125–135 (2015).
36. Wellnhofer, E. *et al.* **Atherosclerosis** 213, 475–81 (2010).
37. Peiffer, V., Sherwin, S. J. & Weinberg, P. D. **Cardiovasc. Res.** 99, 242–50 (2013).
38. Myers, J. G. *et al.* **Ann. Biomed. Eng.** 29, 109–120 (2001).
39. Feldman, C. L. *et al.* **Am. Heart J.** 143, 931–939 (2002).

40.   Johnston, B. M. *et al.* ***J. Biomech.*** 39, 1116–28 (2006).

41.   Torii, R. *et al.* ***Commun. Numer. Methods Eng.*** 25, 565–580 (2009).

42.   Zeng, D. *et al.* ***J. Biomech. Eng.*** 130, 041014 (2008).

43.   Brown, A. G. *et al.* ***J. Biomech.*** 45, 516–523 (2012)
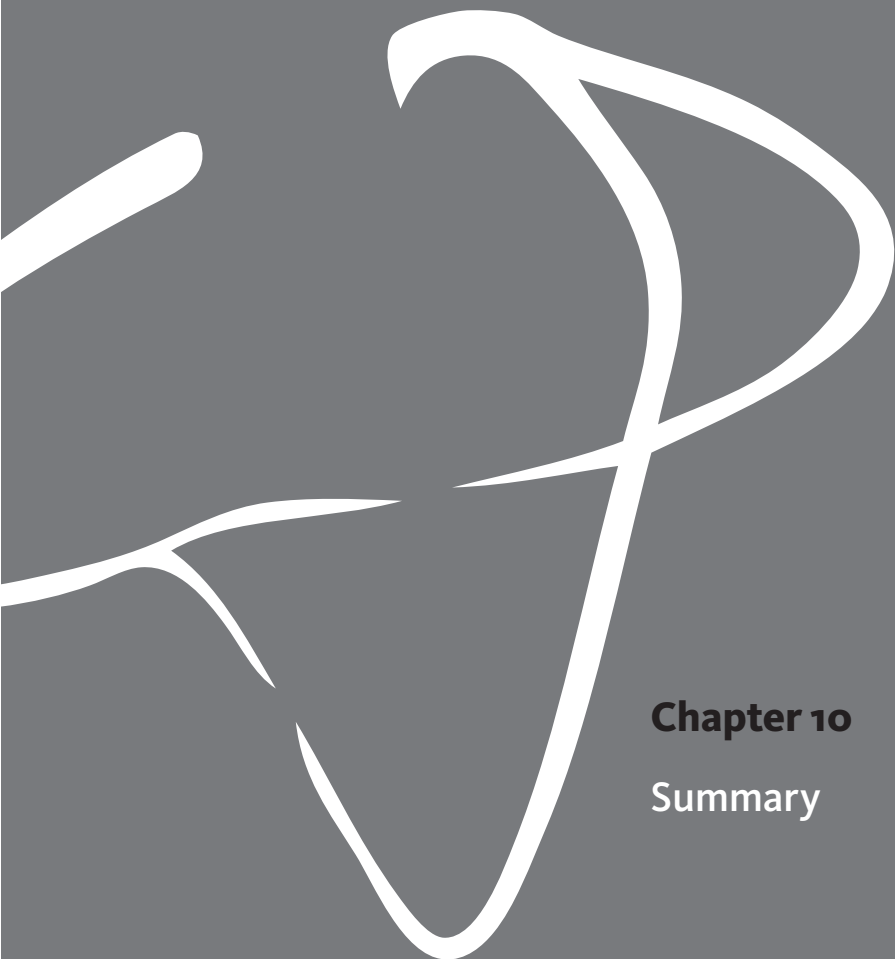
Chapter 10

Summary

Chapter 1 offers a brief introduction on atherosclerosis in coronary arteries and how altered wall shear stress (WSS) levels can result in vulnerable atherosclerotic plaques. Rupture of these vulnerable plaques can potential result in (acute) myocardial infarction followed by sudden death. WSS cannot directly be measured in coronary arteries, but it can be computed with numerical techniques. One requirement to compute WSS is an accurate 3D representation of the geometry of a coronary artery, for which several imaging modalities can be applied. In this thesis x-ray angiography plays a central role for the computations of WSS. A second requirement is to define the inflow and outflow conditions of the reconstructed vessel. These conditions can be based on invasive measurements, so-called reduced-order models or geometry-based scaling laws.

In **chapter 2** the impact of deviations in angiography-based 3D reconstructions on computed WSS was investigated. Two expert readers segmented angiography recordings from four phantoms that mimicked mildly diseased coronary arteries, from which 3D reconstructions were generated. WSS computations were performed in the original phantom geometry and in the reconstructions based on the segmentations from the two readers. A direct comparison of the WSS revealed that qualitatively a good agreement was found. A quantitative comparison brought considerable differences to light in the diseased zones. The quantitative analysis was confirmed by a clinical equivalence analysis, which showed significant differences based on the expected precision of the computational setup.

In **chapter 3** a model is introduced that predicts the pressure-drop based on geometry in mildly diseased coronary arteries, which can serve as a reduced-order model for the outflow conditions in WSS computations. It uses geometrical features that can be extracted from angiographic data and relates them to the pressure-drop they cause. Besides the often used stenosis degree, also the tapering and curvature of the vessel were incorporated. In spite of the fact that all relevant geometrical features were included, considerable variability was observed.

A second method to predict pressure-drop using imaging data is presented in **chapter 4**. With the Navier-Stokes equations the complete flow field can be acquired by simultaneously solving the velocity and the pressure in a defined domain. This leads to precise results but it comes at a relatively high computational cost. With an assumed velocity distribution the Navier-Stokes equation becomes simpler to solve and the pressure-drop can be determined quickly. The assumed velocity distribution was estimated using the luminal contours. As a first step in the development the curvature was still omitted. This method, based on the Navier-Stokes equation, led to a higher accuracy than the morphological approach in chapter 3.

Chapter 5 investigates if outflow conditions in WSS computations can be set with geometry-based scaling laws. Ten coronary bifurcations from patients suffering of coronary artery disease were imaged with computed tomography angiography. Additionally, the myocardial blood flow was imaged with an emerging non-invasive imaging technique called dynamic computed tomography perfusion imaging. The outflow conditions were set with these measurements or with scaling laws that were either based on the myocardial volume or on the diameter of the daughter branches. A good agreement was found between the measured and scaled outflow ratios. The influence of the different approaches on the computed pressure drop was minor. The normalized WSS was relatively unaffected by the variations in outflow ratios, the absolute WSS values showed more sensitivity to the different approaches.

In **chapter 6** the influence of using scaling laws was investigated to set not only the outflow but also the inflow conditions. Eight patients that were scheduled for percutaneous coronary intervention were imaged with angiography. Additionally, the velocity proximal and distal of a bifurcation was acquired with an intravascular Doppler measurement. These measurements were used to set the inflow and outflow conditions for the first set of WSS computations in the bifurcations. In the second set of computations the absolute inflow and the outflow ratio were set with geometry-based scaling laws using angiography data. A reasonable agreement was found between the measured and scaled inflows. The measured and the scaled outflow ratios showed a good agreement. The WSS from the measured-approach and the scaled-approach were directly compared. Consistent with the findings in chapter 5, this study showed that normalized WSS can be obtained from angiography data alone by applying diameter-based scaling laws to define the boundary conditions. Caution should be taken when absolute WSS is assessed from computations that used scaled boundary conditions.

Besides WSS another image-based parameter is associated with the risk for acute myocardial infarction, namely the thickness the fibrous cap that separates fatty deposits from the lumen. In **chapter 7** the coronary arteries from 14 patients were prospectively imaged with angiography and optical coherence tomography. The angiography data was used the make 3D reconstructions of the coronary bifurcations and set the inflow and outflow conditions for the WSS computations. The fibrous cap-thickness was derived from the optical coherence tomography data. Subsequently, the two parameters were successfully co-registered in 12 cases. Finally, a novel risk-map was introduced that allows a direct visual inspection of the potential rupture-risk.

In **Chapter 8** the main findings of the thesis are discussed. The thesis focused on the potential of computing WSS using angiographic data alone. The angiography-based 3D

reconstructions of the geometry – that can be performed online – proved to result in qualitatively comparable WSS. There was a reasonable agreement between the measured and geometry-based inflows. For the outflow ratios a good agreement was found. Normalized WSS was highly insensitive to the deviations in inflow and outflow conditions. Normalized WSS can be computed using angiography alone, which therefore has potential for online applications in a clinical setting.

Chapter 11

Samenvatting

In **hoofdstuk 1** wordt een korte introductie gegeven over atherosclerosis in krans-slagaders, en over hoe wandschuifspanning (WSS) niveaus gerelateerd zijn aan athe-rosclerotische plaques. Ruptuur van kwetsbare plaques kan mogelijk leiden tot een myocardinfarct en zelfs tot een hartstilstand. Het is niet mogelijk WSS in kransslagaders direct te meten, maar het is wel mogelijk om die te berekenen. Een van de vereiste voor deze berekenigen is een accurate reconstructie van de 3D geometrie van een krans-slagader. Hiervoor kunnen verschillende beeldvormende technieken gebruikt worden. In deze thesis staat angiografie centraal om WSS te berekenen. Een tweede vereiste voor de berekeningen is het voorschrijven van de in- en uitstroomcondities. Dit kan gedaan worden aan de hand van invasieve metingen, zogenoemde *reduced-order models* of met geometrische schalingswetten.

Hoofdstuk 2 onderzoekt het effect dat afwijkingen in 3D reconstructies gebaseerd op angiografie hebben op de WSS-berekeningen. Hiervoor hebben twee experts angiografieopnames van kranslagadersmodellen met een geringe vernauwingsgraad gesegmenteerd. Deze segmentaties vormden de basis voor de 3D reconstructies. De WSS-berekeningen werden gedaan op basis van de originele geometrie van de modellen en op basis van de reconstructies. Uit een directe vergelijking tussen de uitkomsten kon het effect van de reconstructie afwijkingen op de WSS berekeningen worden bepaald. Kwalitatief kwamen de uitkomsten goed overeen. Kwantitief kwamen er verschillen in de vernauwde regio's aan het licht. De kwantitatieve analyse werd vervolgens bevestigd met een test voor klinische equivalentie, die significante verschillen aantoonde op basis van de verwachte nauwkeurigheid van de recontructiemethode.

In **hoofdstuk 3** wordt een model geïntroduceerd dat de drukval voorspelt op basis van de geometrie van kransslagaders met een beperkte vernauwingsgraad. Hievoor gebruikt het model geometrische parameters die uit medische beelden gehaald kunnen worden, en relateerde deze aan de drukval die ze veroorzaken. Dit model kan mogelijk dienen als een *reduced-order* model voor de uitstroomcondities in de 3D WSS-berekeningen. Naast de vaak gebruikte vernauwingsgraad maakt dit model ook gebruik van de curvatuur en het taps toelopen van de kransslagaders. Gemiddeld genomen werkt dit model goed, maar ondanks de zorgvuldige selectie van de parameters resulteerde dit model in een aanzienlijke variatie in de individuduele drukvalvoorspellingen.

In **hoofdstuk 4** wordt een tweede model geïntroduceerd dat de drukval bepaalt aan de hand van geometrie. Met de Navier-Stokes-vergelijkingen kan de druk en de snel-heid van een stromingen precies bepaald worden in een vooraf gedefinieerd domein. Deze methode vergt echter relatief veel rekenkracht. De benodigde rekenkracht voor de drukvalbepaling kan aanzienlijk verminderd worden door vooraf een snelheidsverde-ling in het betreffende domein aan te nemen. In dit model wordt de snelheidsverdeling

bepaald op basis van het verloop van het lumen. Als eerste stap in de ontwikkeling van deze methode is de curvatuur van de kransslagaders niet meegenomen. Met dit model, dat gebaseerd is op Navier-Stokes-vergelijkingen, werd een hogere precisie gehaald dan met het model gebaseerd op enkel de geometrie.

Hoofdstuk 5 onderzoekt hoe uitstroomvoorwaarden bepaald kunnen worden aan de hand van geometrische schalingswetten. Tien coronaire bifurcaties van patiënten met een midle vorm van atherosclerosis in de kransslagaders werden in beeld gebracht met *computed tomography angiography*. Daarnaast werd de myocardiale bloedstroom gemeten met een recent geïntroduceerde techniek genaamd *dynamic computed tomographie perfusion imaging*. De uitstroomvoorwaarden werden vervolgens op drie manieren bepaald: aan de hand van de metingen, het myocard volume in combinatie met de schalingswetten of de diameters van de dochtertakken van de bifurcatie in combinatie met de schalingswetten. De berekende uitstroom ratio's met elk van de drie methodes kwamen in goede mate overeen. Het verschil tussen de berekende drukval van de drie methodes was minimaal. De genormaliseerde WSS werd weinig beïnvloed door de verschillen in uitstroomvoorwaarden, maar de absolute WSS was wel gevoelig voor die verschillen.

De invloed van zowel geschaalde in- als uitstroomvoorwaarden wordt in **hoofdstuk 6** onderzocht. Coronaire bifurcaties van acht patiënten die een percutane coronaire interventie ondergingen werden in beeld gebracht met angiografie. Vervolgens werd ook de stromingssnelheid van het bloed proximaal en distaal van de bifurcatie invasief gemeten. De in- en uitstroomvoorwaarden in een eerste groep WSS-berekeningen werden bepaald aan de hand van deze metingen. Een tweede groep berekeningen werd gedaan met in- en uitstroomvoorwaarden op basis van schalingswetten. De geschaalde instroomwaardes kwamen in redelijke mate overeen met de metingen, voor de uitstroomwaardes werd een goede overeenstemming gevonden. De berekende WSS van beide methodes konden direct vergeleken worden. De genormaliseerd WSS bleek ongevoelig te zijn voor afwijkingen in de in- en uitstroomvoorwaarden, wat in overeenstemming is met de bevindingen van hoofdstuk 5. De absolute WSS was wel gevoelig voor variaties in de randvoorwaarden.

Naast WSS is er een tweede parameter dat geassocieerd wordt met de kans op een myocard infarct, namelijk de dikte van de fibreuze kap die een vetophoping in de wand van het lumen scheidt. Ook deze parameter kan bepaalde worden aan de hand van een beeldvormende techniek. In **hoofdstuk 7** werden de kransslagaders van 14 prospectief geselecteerde patiënten in beeld gebracht met zowel angiografie als met *optical coherence tomographie*. De dikte van de fibreuze kap werd uit de *optical*

coherence tomographie data gehaald. De WSS werd berekend in 3D reconstructies op basis van angiografie in combinatie met in- en uitstroomvoorwaarden gebaseerd op schallingswetten eveneens aan de hand van angiografie data. Co-registratie van beide beeldvormende technieken was mogelijk in 12 van de 14 patienten. Vanuit deze co-registratie werd een nieuwe risico-index ontwikkeld gebaseerd op de dikte van de kap en de WSS verdeling. Deze risico-index geeft een directe weergave van de verhoogde instabiliteit van een atherosclerotische plaque. Deze risico-index kan in de toekomst mogelijk klinische toegepast worden.

In **hoofdstuk 8** worden de hoofdbevindingen van dit proefschrift besproken. Dit werk richtte zich op de mogelijkheid van het berekenen van WSS aan de hand van enkel angiografische beelden. De 3D reconstructies op basis van angiografie bleek een goede basis voor het berekenen van WSS-patronen. De geschaalde instroomwaardes kwamen in redelijke mate overeen met de metingen, voor de uitstroomwaardes werd een goede overeenstemming gevonden. Vervolgens bleek de genormaliseerde WSS ongevoelig voor afwijkingen in in- en uitstroomwaardes. Deze bevingen tonen aan dat de bere-kening van WSS-patronen gedaan kunnen worden op basis van angiografie alleen, wat mogelijkheden schept voor klinische toepassingen.
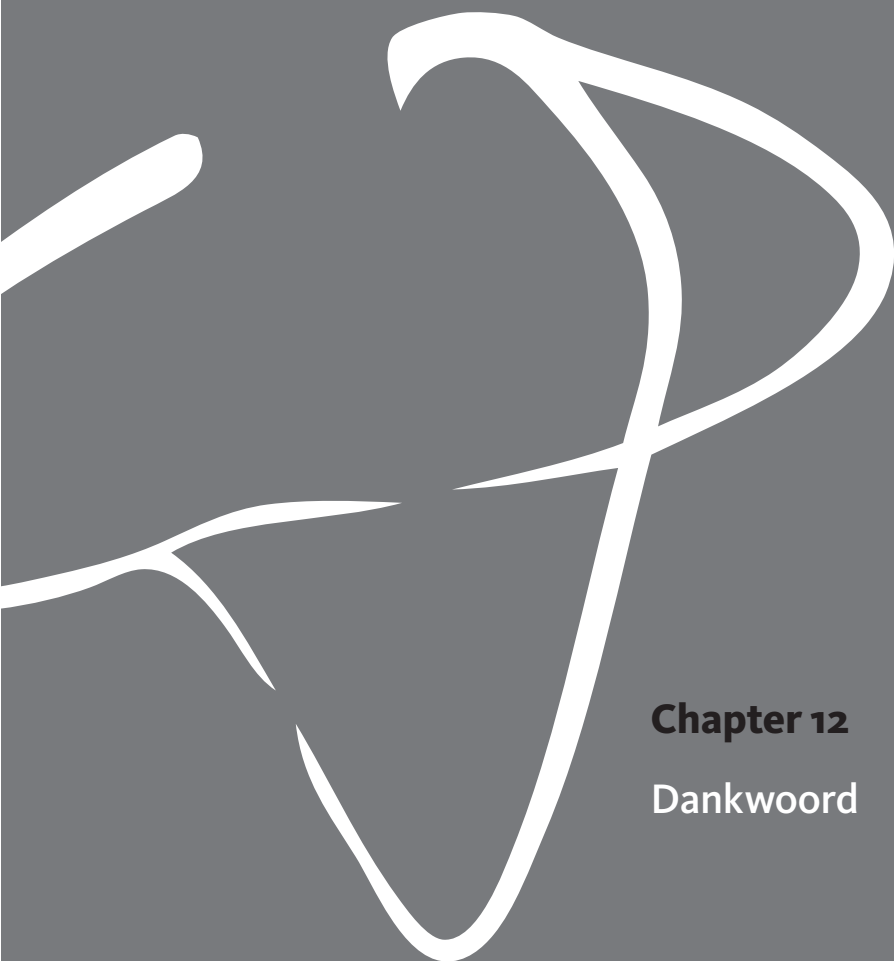
Chapter 12

Dankwoord

Frank, ik wil jou als eerste bedanken voor al je inzet en hulp tijdens dit project. Jouw bijzonder ontspannen manier van werken zorgde er mede voor dat ik met plezier terug kijk op mijn promotietraject. Ik ben blij dat ik jou als begeleider heb gehad en ik heb ontzettend veel van je geleerd. Het is moeilijk te zeggen hoe dit werk eruit zou hebben gezien zonder jouw hulp en inspanning.

Ton, allereerst bedankt voor de kans om een promotieonderzoek te doen. Ik heb de laatste jaren uitgekeken naar onze besprekingen. Je bijzonder snelle en heldere analyses, maar ook je algemene manier van leidinggeven zullen voor mij als een voorbeeld blijven gelden.

Ik wil al mijn collega's bedanken die ervoor zorgden dat ik elke dag weer in een leuke omgeving kon werken. Ik heb mooie herinneringen aan de momenten buiten werktijd. Van de simpele borrels, tot de labuitjes, conferenties en zelfs roadtrips. Ik hoop jullie nog vaak te zien.

Voor mij zijn vrienden heel belangrijk. De (levenslange) achterban uit Roosendaal, de BMTers en de Haagsche huisgenoten, bedankt voor al jullie oprechte belangstelling en gedeelde drankrekeningen. Jullie zijn nog niet van mij af…

Als laatste en belangrijkste bedank ik mijn ouders en zus. Bedankt voor de onvoorstelbare hoeveelheden geduld, vertrouwen en jullie inlevingsvermogen. Zonder jullie zou dit werk er niet zijn.

Chapter 13

Scientific contributions

JOURNAL PAPERS

- R. Rezakhaniha, A. Agianniotis, <u>J.T.C. Schrauwen</u>, A. Griffa, D. Sage, C. V. C. Bouten, F. N. van de Vosse, M. Unser, N. Stergiopulos; Experimental investigation of collagen waviness and orientation in the arterial adventitia using confocal laser scanning microscopy, *Biomechanics and Modeling in Mechanobiology,* 2012, 11(3-4):461-73

- <u>J.T.C. Schrauwen</u>, A. Vilanova, R. Rezakhaniha, N. Stergiopulos, F.N. van de Vosse, P.H.M.Bovendeerd; A method for the quantification of the pressure dependent 3D collagen configuration in the arterial adventitia, *Journal of Structural Biology*, 2012, 180(2):335-42

- <u>J.T.C. Schrauwen</u>, J.J. Wentzel, A.F.W. van der Steen, F.J.H. Gijsen; Geometry-based pressure drop prediction in mildly diseased human coronary arteries, *Journal of Biomechanics,* 2014, 3;47(8):1810-5

- <u>J.T.C. Schrauwen</u>, D.J. Koeze, J.J. Wentzel, F.N. van de Vosse, A.F.W. van der Steen, F.J.H. Gijsen; Fast and Accurate Pressure-Drop Prediction in Straightened Atherosclerotic Coronary Arteries, *Annals of Biomedical Engineering,* 2015, 43(1):59-67

- <u>J.T.C. Schrauwen</u>, A. Coenen, A. Kurata, J.J. Wentzel, A.F.W. van der Steen, K. Nieman, F.J.H. Gijsen; Functional and anatomical measures for outflow boundary conditions in atherosclerotic coronary bifurcations, *Journal of Biomechanics***, 2015, "***in press***"

- <u>J.T.C. Schrauwen</u>, A. Karanasos, N.S. van Ditzhuijzen, J.P. Aben, A.F.W. van der Steen, J.J. Wentzel, F.J.H. Gijsen; Angiography-Based Reconstructions for Wall Shear Stress Computations in Phantoms of Coronary Bifurcations, *PlosOne*, 2015, 10(12)

- <u>J.T.C. Schrauwen</u>, J.C.V. Schwarz, J.J. Wentzel, A.F.W. van der Steen, M. Siebes, F.J.H. Gijsen; Measured versus scaled inflow and outflow boundary conditions for wall shear stress computations in atherosclerotic human coronary bifurcations, "*under review*"

- G. Zahnd*, <u>J.T.C. Schrauwen</u>*, A. Karanasos., E.S. Regar, A.F.W. van der Steen, W.J. Niessen, T. van Walsum, F.J.H. Gijsen; Fusion of fibrous cap thickness and wall shear stress to assess plaque vulnerability in coronary arteries - A pilot study, "*under review*"

- R. Xing, D. De Wilde, G. McCann, Y. Ridwan, <u>J.T.C. Schrauwen</u>, A.F.W. van der Steen, F.J.H. Gijsen, K. van der Heiden; Contrast-enhanced micro-CT imaging for wall shear stress computation in murine carotid arteries, "*submitted*"

*Both authors contributed equally

CONFERENCE CONTRIBUTIONS

- <u>J.T.C. Schrauwen</u>, J.J. Wentzel, A.F.W. van der Steen, F.J.H. Gijsen; 2013, Fractional flow reserve estimation by forward geometrical modelling, at the 4th Dutch Biomedical Engineering 2013 meeting, Egmond aan Zee, the Netherlands – poster presentation

- <u>J.T.C. Schrauwen</u>, J.J. Wentzel, A.F.W. van der Steen, F.J.H. Gijsen, 2013; Fractional flow reserve estimation by forward geometrical modelling, at the ASME summer bioengineering conference 2013, Sun River, U.S. – oral presentation

- <u>J.T.C. Schrauwen</u>, J.J. Wentzel, A.F.W. van der Steen, F.J.H. Gijsen; 2013, Fractional flow reserve estimation by forward geometrical modelling, at the 8th International symposium on Biomechanics in Vascular Biology and Cardiovascular Disease, Rotterdam, NL – poster presentation

- <u>J.T.C. Schrauwen</u>, J.J. Wentzel, A.F.W. van der Steen, F.J.H. Gijsen; 2013, Fractional flow reserve estimation by forward geometrical modelling, at the 3[de] Cardiovasculaire conferentie meeting, Noorwijkerhout, NL – poster presentation

- <u>J.T.C. Schrauwen</u>, D.J. Koeze, J.J. Wentzel, F.N. van de Vosse, A.F.W. van der Steen, F.J.H. Gijsen; 2014, Fast pressure drop calculation with lumen specific assumptions for the Navier-Stokes equations in atherosclerotic human coronary arteries, at the 7th World Conference of Biomechanics, Boston, USA - poster presentation

- <u>J.T.C. Schrauwen</u>, D.J. Koeze, J.J. Wentzel, F.N. van de Vosse, A.F.W. van der Steen, F.J.H. Gijsen; 2014, Fast pressure drop calculation with lumen specific assumptions for the Navier-Stokes equations in atherosclerotic human coronary arteries, 9th International symposium on Biomechanics in Vascular Biology and Cardiovascular Disease, Montreal, Canada – poster presentation

- J.T.C. Schrauwen, D.J. Koeze, J.J. Wentzel, F.N. van de Vosse, A.F.W. van der Steen , F.J.H. Gijsen; 2014, Fast pressure drop calculation with lumen specific assumptions for the Navier-Stokes equations in atherosclerotic human coronary arteries, at the 12th International Symposium on Computer Methods in Biomechanics and Biomedical Engineering, Amsterdam, Netherlands - oral presentation

- J.T.C. Schrauwen, D.J. Koeze, J.J. Wentzel, F.N. van de Vosse, A.F.W. van der Steen , F.J.H. Gijsen; 2015, Fast pressure drop calculation with lumen specific assumptions for the Navier-Stokes equations in atherosclerotic human coronary arteries, at the 5th Dutch Biomedical Engineering Conference, Egmond aan Zee, Netherlands - oral presentation

- J.T.C. Schrauwen, G. Zahnd, J.J. Wentzel, E. Regar, T. van Walsum and F. Gijsen; 2015, Fusion of shear stress mapping and OCT for prediction of plaque rupture in human coronary arteries, at 3rd Optics in Cardiology, Rotterdam, 2015 - poster presentation

- J.T.C. Schrauwen, A. Coenen, A. Kurata, .J. Wentzel, A.F.W. van der Steen, K. Nieman, F.J.H. Gijsen; 2015, Functional and Anatomical Measures for Outflow Boundary Conditions in Atherosclerotic Coronary Bifurcations, at the 10th international symposium on Biomechanics in Vascular Biology and Cardiovascular Disease, Rotterdam, the Netherlands - poster presentation

- J.T.C. Schrauwen, A. Karanasos, N.S. van Ditzhuijzen, J.P. Aben, A.F.W. van der Steen, J.J. Wentzel, F.J.H. Gijsen; 2015, Angiography-Based Reconstructions for Wall Shear Stress Computations in Phantoms of Coronary Bifurcations, at the 10th international symposium on Biomechanics in Vascular Biology and Cardiovascular Disease, Rotterdam, the Netherlands - poster presentation

- J.T.C. Schrauwen, A. Coenen, A. Kurata, .J. Wentzel, A.F.W. van der Steen, K. Nieman, F.J.H. Gijsen; 2015, Functional and Anatomical Measures for Outflow Boundary Conditions in Atherosclerotic Coronary Bifurcations, at the 2015 Summer Biomechanics, Bioengineering and Biotransport Conference, Snowbird, U.S. - oral presentation

- J.T.C. Schrauwen, A. Karanasos, N.S. van Ditzhuijzen, J.P. Aben, A.F.W. van der Steen, J.J. Wentzel, F.J.H. Gijsen; 2015, Angiography-Based Reconstructions for Wall Shear Stress Computations in Phantoms of Coronary Bifurcations, at the 2015 Summer Biomechanics, Bioengineering and Biotransport Conference, Snowbird, U.S. - poster presentation

- J.T.C. Schrauwen, A. Coenen, A. Kurata, .J. Wentzel, A.F.W. van der Steen, K. Nieman, F.J.H. Gijsen; 2015, Functional and Anatomical Measures for Outflow Boundary Conditions in Atherosclerotic Coronary Bifurcations, at the Computational Fluid Dynamics in Medicine and Biology II, Albufeira, Portigual - oral presentation

- G.Zahnd, J.T.C Schrauwen, A. Karanasos, E.S. Regar, W.J. Niessen, T. van Walsum, F.J.H. Gijsen; 2015, Fusion of fibrous cap thickness and wall shear stress to assess plaque vulnerability in coronary arteries - A pilot study, at MICCAI 2015 CVII-STENT workshop, Munchen, Germany
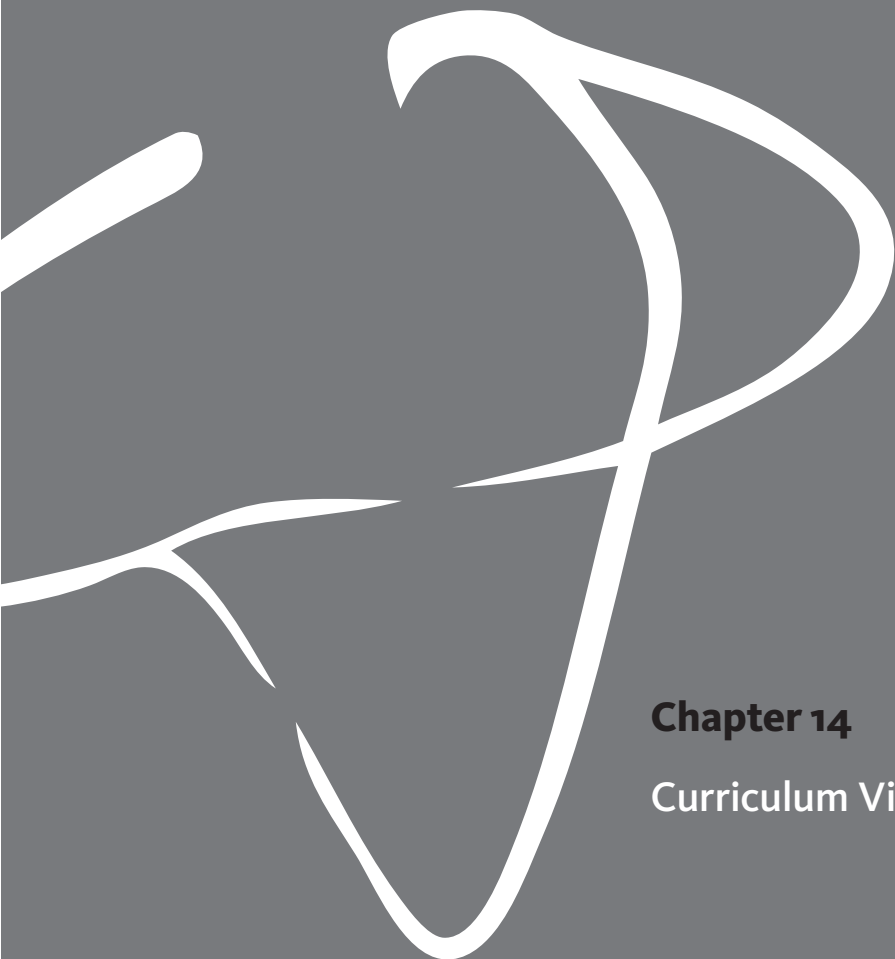
Chapter 14

Curriculum Vitae

Jelle Tymen Christiaan Schrauwen

June 5th 1986, Roosendaal, the Netherlands

2005 – 2008:   B.Sc Biomedial Engineering
                  Eindhoven University of Technology, Eindhoven, the Netherlands

2008 – 2011:   M.Sc. Biomedial Engineering
                  Eindhoven University of Technology, Eindhoven, the Netherlands

2009 – 2010:   Research Assistant
                  Laboratory of Hemodynamics and Cardiovascular Technology
                  Ecolé Polytechnique Federale Lausanne, Lausanne, Zwitserland

2011 – 2015:   Ph.D. research
                  Department of Biomedical Engineering
                  Erasmus Medical Center, Rotterdam, the Netherlands

Chapter 15

PhD portfolio

Conference and symposium attendance	Year	ECTS
• 1st Optics in Cardiology symposium, Rotterdam, NL	2011	0.6
• Holst memorial lecture and symposium, Eindhoven, NL	2011	0.3
• Symposium 'Een warm hart' (ICIN), Amsterdam	2012	0.3
• 7th International symposium on Biomechanics in Vascular Biology and Cardiovascular Disease, Altanta, Georgia, U.S.	2013	0.6
• 4th Dutch Bio-Medical Engineering Conference, Egmond aan Zee, Netherlands	2013	0.6
• ASME summer bioengineering conference, Sunriver, Oregon, U.S.	2013	1.5
• 8th International symposium on Biomechanics in Vascular Biology and Cardiovascular Disease, Rotterdam, NL	2013	0.6
• 2nd Optics in Cardiology symposium	2013	0.6
• 7th World Conference of Biomechanics, Boston, U.S.	2014	1.5
• 12th International Symposium on Computer Methods in Biomechanics and Biomedical Engineering, Amsterdam	2014	0.9
• 5th Dutch Bio-Medical Engineering Conference, Egmond aan Zee, Netherlands	2015	0.6
• 3rd conference on Optics in Cardiology, Rotterdam, NL	2015	0.6
• 10th International symposium on Biomechanics in Vascular Biology and Cardiovascular Disease, Rotterdam, NL	2015	0.6
• Summer Biomechanics, Bioengineering and Biotransport Conference, Snowbird, Utah, U.S.	2015	1.5

Courses & Seminars	Year	ECTS
• Computational Fluid Dynamics I – J.M. Burgerscentrum, Delft, NL	2012	2.0
• Atherosclerotic & Aneurysmal Disease (COEUR), Rotterdam, NL	2012	0.6
• Annual COEUR PhD day, Rotterdam, NL	2012	0.3
• Annual BME research day (TU/e), Eindhoven, NL	2012	0.3
• Research seminar: opening CERES research center (TU/e), Eindhoven, NL	2012	0.3
• Research seminar: Imaging of Carotid arteries – structure and function, Rotterdam, NL	2012	0.3
• Research seminar: Carotid atherosclerotic plaques – Biomechanics and imaging, Rotterdam, NL	2013	0.3
• Annual BME research day (TU/e), Eindhoven, NL	2013	0.3
• Annual COEUR PhD day, Rotterdam, NL	2013	0.3
• Cardiovascular Imaging and Diagnostics (COEUR), Rotterdam, NL	2013	0.6
• Annual conference Dutch Technology Foundation, Nieuwegein, NL	2013	0.3
• Biomedical English Writing and Communication, Rotterdam, NL	2014	4.0
• Biostatistics for clinicians (NIHES), Rotterdam, NL	2014	2.0
• Pathophysiology of Ischemic Heart Disease (COEUR), Rotterdam, NL	2014	0.6
• Presenting yourself and your work, Rotterdam, NL	2014	0.5
• Research seminar: Non-invasive imaging of myocardial ischemia, Rotterdam, NL	2014	0.3
• Annual COEUR PhD day, Rotterdam, NL	2015	0.3

Presentations	Year	ECTS
• 4th Dutch Bio-Medical Engineering Conference, Egmond aan Zee, Netherlands – poster presentation	2013	0.2
• ASME summer bioengineering conference, Sunriver, U.S. – oral presentation	2013	0.2
• 8th International symposium on Biomechanics in Vascular Biology and Cardiovascular Disease, Rotterdam, NL – poster presentation	2013	0.2
• CVC meeting, Noordwijkerhout, NL – poster presentation	2013	0.2
• 7th World Conference of Biomechanics, Boston, U.S. – poster presentation	2014	0.2
• 9th International symposium on Biomechanics in Vascular Biology and Cardiovascular Disease, Montreal, Canada – poster presentation	2014	0.2
• 12th International Symposium on Computer Methods in Biomechanics and Biomedical Engineering, Amsterdam – oral presentation	2014	0.2
• 5th Dutch Bio-Medical Engineering Conference, Egmond aan Zee, Netherlands – oral presentation	2015	0.2
• 3th conference on Optics in Cardiology, Rotterdam, NL – poster presentation	2015	0.2
• 10th International symposium on Biomechanics in Vascular Biology and Cardiovascular Disease, Rotterdam, NL – two poster presentations	2015	0.4
• Summer Biomechanics, Bioengineering and Biotransport Conference, Snowbird, U.S. – oral & poster presentation	2015	0.4
• Computational Fluid Dynamics in Medicine and Biology II, Albuifeira, Portugal – oral presentation	2015	0.2

Activities	Year	ECTS
• Organization of 'lab-day-out', Department of Biomedical Engineering, Rotterdam, NL	2013 / 2014	2.0 / 2.0
• member PhD committee of the Cardiovascular Research School Erasmus University Rotterdam (COEUR)	2013/2014 / 2014/2015	1.0 / 1.0
• Supervision of 3 master students	2012-2014	7.5
• Audio support at 10th International symposium on Biomechanics in Vascular Biology and Cardiovascular Disease, Rotterdam, NL	2015	0.6